

# FINAL REPORT

Advanced EMI Models and Classification Algorithms: The Next  
Level of Sophistication to Improve Discrimination of  
Challenging Targets

SERDP Project MR-2225

JANUARY 2017

Dr. Fridon Shubitidze  
Dartmouth College

*Distribution Statement A*

*This document has been cleared for public release*



*Page Intentionally Left Blank*

This report was prepared under contract to the Department of Defense Strategic Environmental Research and Development Program (SERDP). The publication of this report does not indicate endorsement by the Department of Defense, nor should the contents be construed as reflecting the official policy or position of the Department of Defense. Reference herein to any specific commercial product, process, or service by trade name, trademark, manufacturer, or otherwise, does not necessarily constitute or imply its endorsement, recommendation, or favoring by the Department of Defense.

*Page Intentionally Left Blank*

REPORT DOCUMENTATION PAGE			Form Approved OMB No. 0704-0188	
Public reporting burden for this collection of information is estimated to average 1 hour per response, including the time for reviewing instructions, searching existing data sources, gathering and maintaining the data needed, and completing and reviewing this collection of information. Send comments regarding this burden estimate or any other aspect of this collection of information, including suggestions for reducing this burden to Department of Defense, Washington Headquarters Services, Directorate for Information Operations and Reports (0704-0188), 1215 Jefferson Davis Highway, Suite 1204, Arlington, VA 22202-4302. Respondents should be aware that notwithstanding any other provision of law, no person shall be subject to any penalty for failing to comply with a collection of information if it does not display a currently valid OMB control number. <b>PLEASE DO NOT RETURN YOUR FORM TO THE ABOVE ADDRESS.</b>				
1. REPORT DATE (DD-MM-YYYY) April 25, 2017		2. REPORT TYPE Draft final report		3. DATES COVERED (From - To) 6 April, 2012- 30 April, 2017
4. TITLE AND SUBTITLE			5a. CONTRACT NUMBER W912HQ-12-C-0014	
			5b. GRANT NUMBER	
			5c. PROGRAM ELEMENT NUMBER	
6. AUTHOR(S)  Dr. Fridon Shubitidze, Dr. Juan Pablo Fernández, Dr. Benjamin Barrowes Mr. Dave George, Dr. Daniel Stienhurst, Dr. Thomas Bell			5d. PROJECT NUMBER MR-2225	
			5e. TASK NUMBER	
			5f. WORK UNIT NUMBER	
7. PERFORMING ORGANIZATION NAME(S) AND ADDRESS(ES)  Dartmouth College, Thayer School of Engineering, 14 Engineering Dr. Hanover, NH, 03755			8. PERFORMING ORGANIZATION REPORT NUMBER	
9. SPONSORING / MONITORING AGENCY NAME(S) AND ADDRESS(ES)  SERDP Office 4800 Mark Center Drive, Suite Alexandria, VA 22350-3605			10. SPONSOR/MONITOR'S ACRONYM(S)	
			11. SPONSOR/MONITOR'S REPORT NUMBER(S)	
12. DISTRIBUTION / AVAILABILITY STATEMENT  Approved for public release; distribution is unlimited.				
13. SUPPLEMENTARY NOTES N/A				
14. ABSTRACT  This project yields combined software/hardware approaches for enhancing the detection and classification of small and/or deep targets at live UXO sites. Advanced EMI models were adapted to existing hardware, hardware electronics were modified to increase EMI responses from buried targets, and modified hardware/software performance was evaluated using test-stand and blind data sets. The combined approach detected and classified all shallow targets and also managed to detect and classify small targets buried as deep as 20 times the target diameter. The high-power transmitter system developed here has been implemented in the Geometrics mini MetalMapper, a commercially available version of the 2 × 2 TEMTADS.				
15. SUBJECT TERMS UXO; High power transmitter; electromagnetic induction; forward and inverse EMI models; detection; classification; Cued; deep targets; sensors;				
16. SECURITY CLASSIFICATION OF:			17. LIMITATION OF ABSTRACT  UU	18. NUMBER OF PAGES  116
a. REPORT U	b. ABSTRACT U	c. THIS PAGE U		19a. NAME OF RESPONSIBLE PERSON
				19b. TELEPHONE NUMBER (include area code) 603 646 3671

*Page Intentionally Left Blank*

## Contents

Abstract .....	1
Objective .....	1
Technical Approach .....	1
Results .....	2
Benefits .....	2
Acknowledgments .....	3
1    Introduction .....	4
2    Objectives .....	5
3    Technical approach .....	9
The orthonormalized volume magnetic source model .....	10
3.1.1    Orthonormal Green functions .....	11
3.1.2    ONVMS procedure .....	13
Joint diagonalization for multi-target data pre-processing .....	15
3.1.3    The multi-static response matrix .....	16
3.1.4    Interpretation and diagonalization of the MSR matrix .....	17
3.1.5    Algorithm for joint diagonalization .....	20
MUSIC algorithm .....	20
3.1.6    Combined JD-MUSIC algorithm .....	22
Automated separation of signal and noise eigenvalues in JD .....	23
EMI data inversion: A global optimization technique .....	24
Discrimination parameters .....	25
4    Results .....	26
5 × 5 TEMTADS test-stand cases .....	26
5 × 5 TEMTADS field test cases .....	32
Combined joint diagonalization-MUSIC algorithm applied to 2 × 2 TEMTADS Test-stand and field results .....	35
The JD algorithm for guiding data collection in real time .....	39
Improving the capability of current advanced EMI sensors to detect and discriminate small and deep targets .....	42
Understanding noise in an EMI system .....	44

Tx-combination/high-current effect.....	48
Large Tx currents: experimental validation.....	49
ONVMS for deep target classification.....	53
5 Modeling advanced EMI sensors: searching for optimal Tx/Rx combinations and configurations .....	55
Introduction.....	55
The high-power $2 \times 2$ TEMTADS.....	55
Assessing transmitter coil detection and classification performance .....	60
5.1.1 Primary field at target .....	60
5.1.2 Secondary field at receiver.....	65
5.1.3 Minimum detectable signal.....	69
5.1.4 Comparisons between secondary field at receiver for different transmitter loops ..	73
5.1.5 Combining and adjusting Tx current magnitudes and directions to improve detection and classification of small and deep targets .....	76
6 APG blind and small-munitions classification studies .....	80
APG blind grids .....	80
APG small-munition grids .....	86
7 Results and discussion .....	90
8 Project-related publications .....	93
9 References.....	94
10 Appendix: Minimizing noise .....	97

## List of Figures

Figure 1: A metallic object under the transmitter. The target's EMI response at the receiver coil can be calculated from the equivalent surface or volume magnetic dipole moment $dm$ .	10
Figure 2. An example case of JD applied to the data of SR-607, a 37-mm projectile from Spencer Range. Plotted on the left are the eigenvalues, of which 4 can be identified above the noise level. On the right shows the proposed way of filtering.	22
Figure 3. Example of typical signal and typical noise eigenvalues chosen from the same case as in Figure 2 (left) and where they landed on the $(\log k)-b$ space (right). The $(\log k)-b$ distribution on the right is classified for signal (red dots) and noise (cyan and blue dots).	24
Figure 4. Test-stand setup showing three targets: a 105-mm shell, a 60-mm mortar (center, half-shrouded), and an aluminum spheroid (top left).	26
Figure 5. Eigenvalues of the 105-mm shell test-stand data from JD, unfiltered on the left and automatic-filtered on the right.	27
Figure 6. Eigenvalue distribution of the 105-mm test-stand case in $(\log k)-b$ space with automated classification into signal (red) and noise (blue) results.	28
Figure 7. Contour surfaces of the $F$ function for the 105-mm test-stand case. Red, blue, and gray show 70%, 50%, and 30% of the maximum value, respectively. The true location is marked by the cross.	28
Figure 8. Eigenvalues of the three-object test-stand case, unfiltered on the left and filtered on the right.	29
Figure 9. Signal (red) and noise (blue) classification results for the three-object test-stand case.	29
Figure 10. Peaks found by MUSIC algorithm displayed using the contour surface of $F$ from (0). The ground truth locations are marked out by the three crosses. Red, blue, and gray show 70%, 50%, and 30% of the maximum value, respectively. The true location is marked by the cross.	30
Figure 11. Eigenvalues of the 37-mm test stand case, unfiltered on the left and filtered on the right. The SNR in this case is noticeably lower, evidencing that signal eigenvalues on the left are not as high above the noise level as in other examples.	31
Figure 12. Location found using the MUSIC algorithm, unfiltered on the left and filtered on the right. Red, blue, and gray show 70%, 50%, and 30% of the maximum value, respectively.	31
Figure 13. Eigenvalues of the SR-614 anomaly, unfiltered on the left and filtered on the right.	32
Figure 14. Ground truth photo of anomaly SR-614.	33
Figure 15. Signal (red) to noise (blue) classification result for anomaly SR-614.	33
Figure 16. Target location found by the MUSIC algorithm for SR-614. Red, blue and, gray show 70%, 50%, and 30% of the maximum value, respectively.	34
Figure 17. Eigenvalues for the 37 mm projectile at a depth of 46.5 cm before (left) and after (right) the filtering process in JD. The characteristic curve of the 37 mm projectile can be identified.	36
Figure 18. The $F$ function of the MUSIC algorithm plotted in the search region. Gray, blue, and red show the contour surfaces of 60%, 75%, and 90% of the maximum value, respectively.	36
Figure 19. Eigenvalues for a 37-mm projectile at a depth of 86 cm, before (left) and after (right) the filtering process in JD. The lower SNR means that only two eigenvalues are above the noise level.	37

Figure 20. Target location found in MUSIC algorithm for the 86 cm depth case before (left) and after (right) the filtering, gray, blue and red shows the contour surface of 60%, 75% and 90% of the maximum value, respectively. ....	37
Figure 21. Eigenvalues for the SR-2059, a 37-mm projectile at a depth of 17.5 cm, before (left) and after (right) the filtering process in JD. ....	38
Figure 22. Ground truth photo and MUSIC result for SR-2059 at Spencer Range. Gray, blue, and red show the contour surface of 60%, 75%, and 90% of the maximum value, respectively. ....	38
Figure 23. Left: Measured $5 \times 5$ TEMTADS monostatic signal versus time for a 37-mm projectile placed 60 cm below the sensor center. Right: MSR matrix eigenvalues versus time extracted via JD from the same 37-mm projectile dataset. ....	39
Figure 24. Inverted total ONVMS for a 37-mm projectile placed 60 cm below the $5 \times 5$ TEMTADS center. ....	40
Figure 25. A vertical 37-mm projectile placed 90 cm below the center of the $5 \times 5$ TEMTADS sensor. Left: MSR data matrix eigenvalues. Right: inverted total ONVMS. ....	41
Figure 26. A vertical 37-mm projectile placed 90 cm below the center of the MetalMapper sensor. Left: MSR data matrix eigenvalues. Right: inverted total ONVMS. ....	41
Figure 27. (Left) Combining TEMTADS Tx loops column-wise and row-wise. (Right) Extracted total ONVMS for the 105 HEAT-round buried horizontally at 115 cm depth: original $5 \times 5$ TEMTADS (solid lines) and combined Tx (crosses). ....	43
Figure 28. Left: $5 \times 5$ TEMTADS MSR eigenvalues for a 105-mm HEAT round buried at a depth of 35 cm. Right: Extracted total ONVMS using all Tx/Rx pairs (solid lines) and using only 4 Tx and all 25 Rx combinations (crosses). The data were collected at the APG blind grid. ....	43
Figure 29. EMI response versus time for a heterogeneous target placed 1.2 m below a $35 \text{ cm} \times 35 \text{ cm}$ Tx loop. Magenta lines correspond the target's responses at $5 \times 5$ Rx positions, while blue lines are for target responses plus noise. ....	45
Figure 30. Number on data points in each logarithmic interval. ....	45
Figure 31. EMI response vs. time at 121 equally spaced logarithmic intervals for a heterogeneous target placed 1.2 m below a $35 \text{ cm} \times 35 \text{ cm}$ transmitter coil. Magenta lines correspond to the target's responses at $5 \times 5$ receiver positions; green lines are for target responses plus noise. The data are integrated at each logarithmic interval. ....	47
Figure 32. Comparisons between magnetic fields for a heterogeneous target with noise (blue and red lines) and without noise (green line). First, data were calculated at every $4 \mu\text{s}$ in a linear scale and then reduced to time gates with equal logarithmic intervals. Comparing between 24 (blue lines) and 121 (red lines) timegates shows that reducing the timegate number improves the data quality at times later than 1 ms. ....	48
Figure 33. EMI signal versus time for a heterogeneous target. ....	49
Figure 34. An experimental setup for the $2 \times 2$ 3D system with large Tx currents. ....	50
Figure 35. Transmitter coil with a 6 A current. Left: time-dependent eigenvalues for a 37-mm projectile placed below the system at a depth of 86 cm. Right: extracted total ONVMS for the 37-mm projectile buried at depths of 42 cm (dashed circle lines) and 86 cm (solid lines). ....	51
Figure 36. Transmitter coil with an 11 A current. Left: time-dependent eigenvalues for a 37-mm projectile placed below the system at a depth of 86 cm. Right: extracted total ONVMS for the 37-mm projectile buried at depths of 42 cm (dashed circle lines) and 86 cm (solid lines). ....	51
Figure 37. Transmitter coil with a 14 A current. Left: time-dependent eigenvalues for a 37-mm projectile placed below the system at a depth of 86 cm. Right: extracted total ONVMS for the 37-mm projectile buried at depths of 42 cm (dashed circle lines) and 86 cm (solid lines). ....	52

Figure 38. Inverted effective ONVMS for an M30 Bomb in a test-stand scenario. The target is oriented 45 degrees at a depth of 150 cm depth (top) and oriented vertically at a depth of 210 cm (bottom). The red lines are the total ONVMS for a library AN M30 Bomb, and the other lines correspond to the effective primary (green), secondary (black), and tertiary (blue) effective polarizabilities for the test AN M30 target. ....	53
Figure 39. Schematic diagram of the NRL TEMTADS 2 × 2 EMI sensor array. Each unit consists of a 35 × 35 cm Tx loop with an 8 cm triaxial Rx cube at its center. The complete system is 0.8 × 0.8 m in size. ....	56
Figure 40. The NRL TEMTADS 2 × 2 system (a) on its cart and (b) with its weather shield removed.....	57
Figure 41. The 2 × 2 TEMTADS geometry. XYZO is a global Cartesian coordinate system, r is an observation point measured with respect to XYZO, and $r'_{2,i}$ is the $i$ th current element on the $T = 2$ transmitter with respect to the global coordinate system. ....	58
Figure 42. A schematic diagram for calculating the secondary magnetic field at location $r_{i,3}$ produced by a responding magnetic dipole m placed at r.....	59
Figure 43. Primary magnetic B field due to standard (left) and high-power (right) TEMTADS transmitter loops around a small (37-mm-like) target placed at six positions. The depths at positions # = 1, 2, ..., 6 are 30 cm, 50 cm, 75 cm, 100 cm, 125 cm and 150 cm, respectively....	62
Figure 44. Primary magnetic B field due to standard MM (left) and large 1.2 m × 1.2 m (right) transmitter loops around a small (37-mm-like) target is placed at six positions. The depths at positions # = 1, 2, ..., 6 are 30 cm, 50 cm, 75 cm, 100 cm, 125 cm and 150 cm, respectively....	63
Figure 45. Primary field versus depth for standard TEMTADS, MM, large Tx, and high-power TEMTADS coils. The electrical properties of each transmitter loop are given in Table 1. ....	64
Figure 46. Comparison between modeled and measured data for APG calibration anomaly #B2. The anomaly is a 57-mm projectile buried at a depth of 32 cm. ....	66
Figure 47. Comparison between modeled and measured data for APG calibration anomaly #K4. The anomaly is a 105-mm projectile buried at a depth of 105 cm. ....	67
Figure 48. Comparison between modeled and measured data for APG calibration anomaly #E1. The anomaly is a 105-mm projectile buried at a depth of 5 cm. ....	68
Figure 49. Noise Spectrum from Meloy 2003, taken from Chrissan and Fraser-Smith (1996). ..	69
Figure 50. Baseline noise level from cube 8 compared to thermal noise of a 1 k $\Omega$ resistor. The graph shows the output of a loop with an effective area of 115 m <sup>2</sup> in units of $\mu\text{V} / \sqrt{2.2 \text{ Hz}}$ . One must multiply the output by 5.8 to obtain B field values in nT/sec/ $\sqrt{\text{Hz}}$ . ....	72
Figure 51. Expanded spectra over the lower part of the frequency range. The y-axes are displayed on a linear scale to illustrate of relative magnitudes in terms of a wideband signal.....	73
Figure 52. B-field values for (left) standard and (right) high-power TEMTADS transmitter loops.....	74
Figure 53. $H_x$ , $H_y$ , and $H_z$ field distributions (in dB) under the 2 × 2 TEMTADS system footprint for Tx coil #1. ....	77
Figure 54. $H_x$ , $H_y$ , and $H_z$ field distributions (in dB) under the 2 × 2 TEMTADS footprint for Tx coils #1 and #2. The coils carry currents of the same magnitude but in opposite directions. ....	77
Figure 55. $H_x$ , $H_y$ , and $H_z$ field distributions (in dB) under the 2 × 2 TEMTADS footprint for Tx coils #1 and #2. The coils carry equal-magnitude currents in the same direction. ....	78
Figure 56. $H_x$ , $H_y$ , and $H_z$ field distributions (in dB) under the 2 × 2 TEMTADS footprint for a large (1 m × 1 m) coil. ....	78

Figure 57. $H_x$ , $H_y$ , and $H_z$ field distributions (in dB) under the $2 \times 2$ TEMTADS footprint for a large $1 \text{ m} \times 1 \text{ m}$ coil combined with Tx #1. Currents have opposite directions in the coils, and the small coil carries a current five times stronger. ....	79
Figure 58. $H_x$ , $H_y$ and $H_z$ field distributions (in dB) under the $2 \times 2$ TEMTADS footprint for a large $1 \text{ m} \times 1 \text{ m}$ coil combined with Tx #2. Currents have opposite directions in the coils, and the small coil carries a current five times stronger. ....	79
Figure 59: The APG TOI. ....	80
Figure 60: Extracted total ONVMS vs time for APG blind grid UXO targets. ....	82
Figure 61. TEMTADS/Pushcart blind grid probability of detection for response and discrimination stages versus their respective false-positive probability. ....	83
Figure 62. TEMTADS/Pushcart blind grid probability of detection for response and discrimination stages versus their respective probability of background alarm. ....	84
Figure 63. TEMTADS/Pushcart capped test-area probability of detection for response and discrimination stages against their respective probability of background alarm. ....	87
Figure 64. TEMTADS/Pushcart uncapped test-area probability of detection for response and discrimination stages against their respective probability of background alarm. ....	87
Figure 65. TEMTADS/Pushcart capped test area probability of detection for response and discrimination stages against the respective probability of background alarm for all ordnance larger than 20 mm. ....	88
Figure 66. TEMTADS/Pushcart uncapped test area probability of detection for response and discrimination stages against the respective probability of background alarm for all ordnance larger than 20 mm. ....	88
Figure 67. B field signals. ....	98
Figure 68. dB/dt signals. ....	99
Figure 69. B signals computed from dB/dt signals. ....	100
Figure 70. dB/dt and CumSum signals for target at position P8 at Aberdeen. ....	101
Figure 71. dB/dt and CumSum signals for target at position P11 at Aberdeen. ....	101
Figure 72. dB/dt and CumSum signals for target at position P3 at Aberdeen. ....	101
Figure 73. B Fields and dB/dt signals for a deep target. ....	102

## List of Tables

Table 1. Electrical properties of transmitting loops modeled. ....	61
Table 2. Comparison of four transmitting loops to detect deep targets .....	74
Table 3. A list of original and combined transmitters for creating a square MRS. ....	81
Table 4. Blind-grid test area results .....	85
Table 5. Blind-grid efficiency and rejection rates .....	85
Table 6. Blind correct-type classification of targets correctly discriminated as munitions.....	86

## List of Acronyms

AIC	Akaike Information Criterion
APG	Aberdeen Proving Ground
BIC	Bayesian Information Criterion
cm	Centimeter
DE	Differential Evolution
DLL	Dynamic Link Libraries
DoD	Department of Defense
EM	Electromagnetic
EMA	Expectation Maximization Algorithm
EMI	Electromagnetic Induction
ESTCP	Environmental Security Technology Certification Program
FCS	Former Camp Sibert
GSEA	Generalized standardized excitation approach
IDA	Institute for Defense Analyses
JD	Joint Diagonalization
MEG	Magneto encephalographic
ML	Maximum Likelihood
$\mu$ s	Microsecond
mm	Millimeter
MM	MetalMapper
MPV	Man-Portable Vector
ms	Millisecond
MR	Munitions response
MSR	Multi-static response
MUSIC	Multiple Signal Classification
NC	North Carolina
NSMS	Normalized surface magnetic source
NV/SMS	Normalized volume or surface magnetic source models
ONVMS	Orthogonal normalized volume magnetic source
ONV/SMS	Orthonormalized volume or surface magnetic source models
PNN	Probabilistic Neural Network
SERDP	Strategic Environmental Research and Development Program
SLO	San Luis Obispo
SVM	Support vector machine
TD	Time Domain
TEMTADS	Time Domain Electromagnetic Towed Array Detection System
TOI	Target of Interest
UXO	Unexploded Ordnance

## **Abstract**

The research described in this report was conducted in fulfillment of Project MM-2225, “Advanced EMI Models and Classification Algorithms: The Next Level of Sophistication to Improve Discrimination of Challenging Targets,” submitted to the Strategic Environmental Research and Development Program (SERDP) in response to the Munitions Management Statement of Need MMSON-12-01 “Advanced Technologies for Detection, Discrimination, and Remediation of Military Munitions on Land”.

## **Objective**

The objective of this project was to enhance the detection, localization, and classification of small and/or deeply buried unexploded ordnance (UXO) by developing fast, noise-tolerant EMI data preprocessing and inversion approaches and by extending the detection range and spatial resolution of next-generation EMI systems using different combinations of transmitter coils and adjusting the coils in both direction and current amplitude. In a real field, electromagnetic responses from actual targets are mixed with noise due to both the instrument and the environment. This project studied two ways to increase the depth at which buried UXO can be detected and characterized: 1) increasing the signal amplitude by using high-power and/or large transmitter loops, and 2) decreasing the noise level through the use of advanced models for EMI data preprocessing and classification.

## **Technical Approach**

This project provides efficient methodologies and practical approaches for improving the detection and classification of small and deeply buried targets at live UXO sites. The project team first considered enhancing EMI data preprocessing and minimizing noise by extending and adapting advanced EMI models—including the Orthonormalized Volume Magnetic Source (ONVMS) model, joint diagonalization (JD), multiple signal classification (MUSIC), and a combined JD-MUSIC approach—to existing system hardware to extend detection range and spatial resolution. Second, the team modified and updated current EMI sensor hardware to enhance the capability to detect and single out EMI signals from buried targets. The combined software/hardware suite was used to extract classification features from small and/or deep targets, and its performance was evaluated using test-stand and blind data sets.

## Results

Data analyses using advanced EMI models were conducted for test-stand data sets collected with the MetalMapper and the  $5 \times 5$  and  $3D-2 \times 2$  versions of the TEMTADS sensor. An updated system (a high-power  $2 \times 2$  TEMTADS system with 14 A transmitter currents) was deployed and tested at the blind and small-munitions sites at Aberdeen Proving Ground in Maryland. The data were processed using a combined ONVMS-DE approach that extracted intrinsic and extrinsic parameters from targets and ultimately classified each one as either UXO or non-UXO. Excellent classification results were obtained at both grids for all anomalies larger than 20 mm.

## Benefits

The results clearly demonstrated that the combined hardware/software approaches developed by this project are able to detect, locate, and classify buried small and/or deep UXO. The advanced EMI models described here shall remain the preferred approach for analyzing small and/or deep buried targets using EMI data. Not only was the combined approach able to detect and discriminate all shallow targets, it also managed to detect and classify small targets buried as deep as 20 times the target diameter. The high-power transmitter approach developed here has been implemented in a state-of-the-art instrument, a commercially available version of the  $2 \times 2$  TEMTADS called the Geometrics mini MetalMapper.

## Acknowledgments

Funding for this project was provided by the Strategic Environmental Research and Development Program (SERDP). We wish to express our sincere appreciation to Dr. Herb Nelson, Dr. Anne Andrews, and the staff of the SERDP and ESTCP offices for their support.

The Principal Investigator, Dr. Fridon Shubitidze of the Thayer School of Engineering at Dartmouth College, conceived implementations of advanced EMI data pre-processing, inversion, and classification approaches for detection and classification of small and/or deeply buried targets. He successfully applied these approaches to all UXO data collected at the Aberdeen Proving Ground blind and small munitions test sites.

Mr. Yinlin Wang, of the Thayer School of Engineering at Dartmouth College, implemented the MUSIC and joint diagonalization algorithms for TEMTADS and applied them to test-stand and blind data sets.

Mr. Johnny Sigman, of the Thayer School of Engineering at Dartmouth College, created an expert-free classification utility and applied it to data collected at Spencer Range.

Mr. Dave George, of G&G Sciences, designed and built a high-power transmitter system, collected test-stand data, and implemented the joint diagonalization algorithm in the GEM-3D.

Dr. Juan Pablo Fernández, previously of the Thayer School of Engineering at Dartmouth College, applied advanced models to next generation systems' data sets and created technical documentations and papers.

Dr. Benjamin Barrowes, of the US Army ERDC-CRREL, participated in the design, development, and testing of next-generation systems for detecting and classifying deep and/or small targets.

Dr. Daniel Stienhurst, of NOVA Research, implemented the joint diagonalization algorithm in the TEMTADS data pre-processing software, deployed the high-power TEMTADS at Aberdeen Proving Ground, and collected data.

Dr. Thomas Bell, of Leidos, conducted noise analysis for the TEMTADS system.

# 1 Introduction

Recent live-site discrimination studies at various live UXO sites [1], such as San Luis Obispo [2], CA (SLO), Camp Butner, NC [3], [4], Camp Beale, CA[5], [6], etc., have revealed that advanced electromagnetic induction (EMI) sensors, which currently feature multi-axis illumination of targets and tri-axial vector sensing [2] (*e.g.*, MetalMapper) or exploit multi-static array data acquisition (*e.g.*, TEMTADS) [5]-[7], together with advanced EMI models [3], provide superb classification performance relative to the previous generation of single-axis monostatic sensors [4]. However, these advances have yet to improve significantly the ability to classify small targets with calibers ranging from 20 to 60 mm, classify deep targets, or provide the high fidelity necessary to distinguish overlapping target signatures in highly cluttered and complex geological environments, for example those with magnetic soil. For example, earlier ESTCP-sponsored pilot live-site UXO classification studies, like the one carried out at SLO, showed that EMI sensors and classification algorithms encountered difficulties when attempting to correctly classify 37-mm rounds and 60-mm mortars buried deeper than 11 times the target diameter. In addition, a live-site test at the Massachusetts Military Reservation highlighted the difficulties for current sensors in classifying large and small, deep, and overlapping targets with high confidence.

This report provides results for small- and/or deep-target detection and classification with high confidence using advanced models and updated electromagnetic induction (EMI) systems. Two approaches are taken to improve target detection and classification: 1) advanced EMI models are adapted to the existing systems and 2) detection limits of current sensors are enhanced by modifying their hardware. Based on these approaches, this report illustrates a combined software/hardware suite that extends the detection range and spatial resolution to next-generation EMI systems, analyzes extracted classification features for small and/or deep targets, and demonstrates the ability of the combined method ability to detect and discriminate small targets buried as deep as 20 times the target diameter. The studies are conducted for both the MetalMapper and the TEMTADS systems, the latter in both its  $5 \times 5$  and  $3D-2 \times 2$  versions. The data analyses are carried out using advanced EMI models that include the Orthonormalized Volume Magnetic Source (ONVMS) [8] model, joint diagonalization (JD) [9], multiple signal classification (MUSIC) [10], and a combined JD-MUSIC approach [11].

In the combined JD-MUSIC approach, the data first goes through a process to form a time-dependent set of multistatic response (MSR) square matrices that are fed into the JD technique. JD then finds the common eigenvectors that diagonalize the entire set MSR matrices, which contain both target signal and noise data, and further sorts and filters them: the eigenvectors originating from targets of interest (TOI) and from noise are identified and passed into a MUSIC algorithm that separates the signal subspace from the noise subspace, thus enhancing the signal-to-noise ratio (SNR). (JD also overcomes a major disadvantage of MUSIC by providing an accurate estimate of the number of signals that are present.) The MUSIC algorithm defines an orthogonal function and maps the noise subspace onto a calculated array of Green functions. The orthogonality between the noise and signal subspaces allows one to estimate the target locations from the resulting maxima. Because the Green function is pre-calculated, the method is fast enough to perform target mapping in real or near-real time.

## 2 Objectives

The principal objective of this project is to improve our advanced EMI models and classification algorithms by developing fast, noise-tolerant EMI data pre-processing approaches that enable the discrimination of small and deep targets; to research adaptive techniques for isolating large and small overlapping targets in high-clutter environments; and to extend the detection range and spatial resolution of next-generation EMI systems by deploying multiple transmitter coils with currents adjustable in both direction and amplitude. The following are the specific technical objectives:

- Improve data quality by using the JD methodology to provide real-time guidance so next-generation EMI systems can find the best location from which to interrogate anomalies in both cued and dynamic acquisition modes. For each detected anomaly we build an MSR data matrix and extract its time-dependent eigenvalues using the JD technique *without performing data inversion*. The MSR eigenvalues can be used to make a quick estimate of the number of potential targets and roughly map their locations relative to the sensor. Tackling this problem first allows us to locate the sensors precisely over the anomalies and thus address one of the major problems recognized during recent ESTCP live-UXO studies. This step involves a modification

of the JD approach developed under SERDP 1632 and ESTCP 201101 for the data-collection stage.

- Develop a fast target-discrimination algorithm based on the MSR eigenvalues' time-decay patterns. All current-generation multi-receiver EMI systems can provide an MSR data matrix at each time gate for a given transmitter/receiver configuration. The eigenvalues and eigenvectors of the MSR data matrix are characteristic of the assortment of underground targets. In other words, 1) the number of nonzero eigenvalues (*i.e.*, those above the noise threshold) depends upon the number of targets, and 2) the eigenvalues' time-decay patterns are intrinsic properties of the targets in question. Developing a fast eigenvalue pattern-recognition technique that identifies time-decay rates, shapes, and (log-scale) slopes allows us to discriminate complex mixtures of munitions of different types without performing any library matching or table lookup. The problem of identifying “unexpected” TOI (*i.e.*, targets native to a given site but not expected from site history or site preparation data), first recognized during the SLO study, is a challenge for current statistical classification algorithms because usually there are insufficient samples of “unexpected” TOI (and, in some cases, none) that can be used to train the classifiers. The proposed pattern-recognition algorithm reduces false negatives and improves our ability to identify “unexpected” TOI correctly.
- Determine the feasibility of using different combinations ( $2 \times 2$ ,  $3 \times 3$ ,  $4 \times 4$ , etc.) of transmitters (Tx) and receivers (Rx) to improve target discrimination. We test the JD algorithm on different Tx/Rx combinations to determine which of them contain the most valuable information about the targets. We also analyze how a given combination isolates one target from another in a highly cluttered environment. In this project, we use an optimal design approach with multiple types of prior information as inputs—such as the sensor's detection depth, target classification feature parameters, etc.—to find the best transmitter/receiver configurations for target classification. In addition, we implement the MUSIC algorithm to infer target locations. The great advantage of MUSIC over traditional nonlinear inversion is that MUSIC avoids nonlinear searches in spaces of high dimension. In addition,

regardless of the number of targets, MUSIC can give a suboptimal estimate of the source locations by using only one 3D search in the solution space. The source locations are estimated by checking the orthogonality between the modeled field (*i.e.*, the Green function) and the noise subspace projection.

- Develop an adaptive approach for multi-target inversion and classification. Most of the currently available multi-target inversion algorithms invert EMI data simultaneously. Recent studies show that these approaches produce good results when signals from small TOI are comparable to those of nearby targets. However, in real field situations there will always be cases in which a small TOI lies under a large non-TOI, resulting in a classic electromagnetic shielding problem. Since a target's response depends on its volume and its distance to the sensor as  $V/R^6$ , the signal from the small TOI is indistinguishable from that of the piece of clutter. To the best of our knowledge none of the existing multi-target inversion techniques can overcome this limitation; the JD technique, in which one can remove from the data the contribution from a large target by suppressing large eigenvalues and their corresponding eigenvectors, stands as a possible exception to this rule and warrants more investigation.
- Improve the capability of current advanced EMI sensors to detect and discern small and deeply buried targets by searching for optimal Tx/Rx combinations and configurations. Current EMI sensors can detect targets down to a depth limited by the geometric size of the Tx coils, the amplitudes of the transmitting currents, and the noise floor of the receivers. The last two factors are not independent: one could in principle detect a deeply buried target by increasing the amplitude of the Tx current, but this also increases the noise and does not improve the SNR. The problem could also be overcome by increasing the size of the Tx coils and thus their moment. Current multi-transmitter sensors such as TEMTADS can be electronically tweaked to provide a big Tx moment: they can be modified to transmit signals from two, three or more Tx coils simultaneously. We propose to enhance the deep-target detection capability of TEMTADS by exploring different combinations of Tx coils. First we model different multi-Tx combinations within TEMTADS using a full 3D EMI solver

based on the method of auxiliary sources (MAS). We then determine the feasibility of honing these combinations for enhanced detection and discrimination of deep targets. Finally, we investigate how to improve the spatial resolution and focusing properties of the primary magnetic field by electronically adjusting the currents of the transmitters.

- Use the results of the above-mentioned studies to redesign and modify the electronics of the TEMTADS system and use the improved apparatus to conduct actual experimental studies.
- Combine the physically complete EMI models developed by our group (*e.g.*, the Ortho-Normalized Volume Magnetic Source model and the Normalized Surface Magnetic Source model) with the adaptive JD-based technique described above in order to discern small and deep targets and to classify different types of UXO. Investigate, test, and document the advantages and disadvantages of the combined model for different Tx/Rx configurations and in multi-target scenarios. Adapt existing discrimination techniques (pattern recognition, Gaussian mixture model for target clustering, and genetic programming, to mention a few) to perform automatic classification.

### 3 Technical approach

This chapter outlines advanced EMI models for detection and classification of small and/or deep targets. Namely, here we present 1) an ONVMS technique [8] and 2) a combined joint diagonalization (JD) [9] and multiple signal classification (MUSIC) [10] algorithm for estimating subsurface object locations from electromagnetic induction (EMI) sensor data without solving ill-posed inverse-scattering problems. Recently, we developed a set of advanced, physically complete, fast, accurate, and clutter-tolerant forward models for UXO discrimination that includes the normalized surface magnetic source (NSMS) [12] model and the ortho-normalized volume magnetic source (ONVMS) model [8]. The NSMS model can be considered as a generalized surface dipole model, and in fact contains the point dipole model as a limiting case. The ONVMS model, a further extension of NSMS, is based on the assumption that a collection of scatterers can be replaced with a set of magnetic dipole sources, distributed over a volume, that mimic the eddy currents and magnetic response that are induced on the targets by the sensor and that in turn establish the observable secondary field. These induced dipoles and currents are distributed inside the objects in question, and thus the spatial distribution of the responding dipoles (their amplitudes scaled by the primary field) traces a map of “response activity” with a clustering pattern that reveals the locations and orientations of the targets present within.

JD is a numerical technique [9], [13]-[17] that finds the common eigenvectors that diagonalize a set of multistatic response (MSR) matrices measured by a time-domain EMI sensor. Eigenvalues from targets of interest (TOI) can be then distinguished automatically from noise-related eigenvalues. Filtering is also carried out in JD to improve the signal-to-noise ratio (SNR) of the data. The MUSIC algorithm utilizes the orthogonality between the signal and noise subspaces in the MSR matrix, which can be separated with information provided by JD. An array of previously calculated Green functions are then projected onto the noise subspace, and the location of the target is estimated by the extremum of the projection owing to the orthogonality. This combined method is applied to data from the Time-Domain Electromagnetic Multisensor Towed Array Detection System (TEMTADS). Examples of TEMTADS test-stand and field data collected at Spencer Range, TN, are analyzed and presented. Results indicate that, due to its

non-iterative mechanism, the method can be executed fast enough to provide real-time estimation of object locations in the field.

### The orthonormalized volume magnetic source model

Most EMI sensors are composed of separate transmitting and receiving coils. When the operator activates the sensor, a current runs through the transmitter coils, which results in the establishment of a (“primary” or “principal”) magnetic field in the surrounding space (Figure 1). According to the elementary atomic model of matter, all materials are composed of atoms, each with a positively charged nucleus and a number of orbiting negatively charged electrons. The orbiting electrons cause circulating currents and form microscopic magnetic dipoles. In the absence of an external magnetic field, the magnetic dipoles of atoms of most materials have random orientations, resulting in no magnetic moment. The application of an external time-varying magnetic field, by Faraday’s law, induces eddy currents in highly conducting bodies by aligning the magnetic moments of the spinning electrons and the magnetic moments due to changes in the orbital motion of electrons. These currents and magnetization in turn generate a (“secondary” or “scattered”) magnetic field that also varies with time and induces measurable currents in the receiving coils. The induced magnetic dipoles/eddy currents are distributed inside the object and produce a magnetic field intensity  $\mathbf{H}$  outside. The magnetic field due to the  $i$ -th source can then be expressed at any observation point  $\mathbf{r}$  as the matrix-vector product

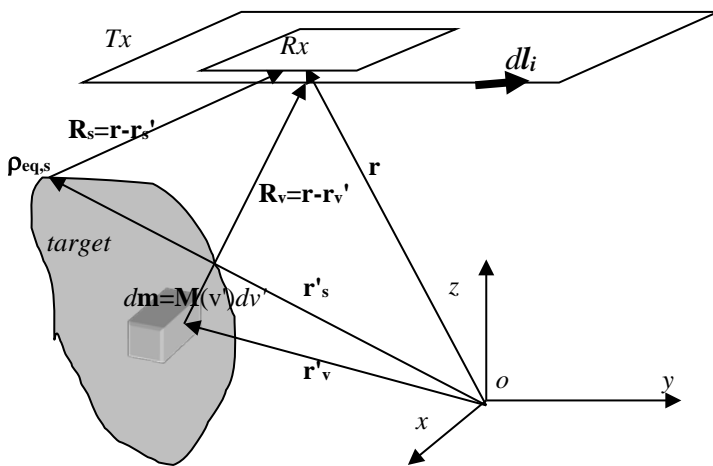


Figure 1: A metallic object under the transmitter. The target’s EMI response at the receiver coil can be calculated from the equivalent surface or volume magnetic dipole moment  $dm$ .

$$\mathbf{H}_i(\mathbf{r}) = G_i(\mathbf{r})\mathbf{m}_i, \quad (0)$$

where the Green function  $G_i$  is given in detail in [8]. When there are several such sources, the total field can be expressed as a superposition:

$$\mathbf{H}(\mathbf{r}) = \sum_{i=1}^M G_i(\mathbf{r})\mathbf{m}_i = \begin{bmatrix} G_1 & G_2 & \cdots \end{bmatrix} \begin{bmatrix} \mathbf{m}_1 \\ \mathbf{m}_2 \\ \vdots \end{bmatrix}. \quad (0)$$

Before going further we note that our method takes as input the (in principle unknown) number  $M$  of radiating sources. For advanced EMI sensors such as the MetalMapper and  $2 \times 2$  and  $5 \times 5$  TEMTADS arrays we have developed a procedure based on joint diagonalization, sketched in Section 3.2, that estimates  $M$  starting from raw data and with no need for inversion. For other sensors one may proceed by letting  $M$  vary as part of an optimization routine.

The superposition (0) can be used (and often has) to carry out one- and multi-object inversions starting from data taken at an ensemble of points. All the measured  $\mathbf{H}$ -values—which can pertain to multiple transmitters, multiple receivers, and different vector components—are strung together in a one-dimensional array, while the corresponding Green functions are stacked as matrix rows. The resulting composite  $G$  matrix can then be (pseudo)inverted to find the strengths of the sources. This procedure, which is nothing other than the dipole model if each body is taken to be represented by one source only, works well for one or two sources, but for larger numbers becomes very time-consuming (since the Green matrix becomes very large) and increasingly ill-posed, usually requiring regularization. The ONVMS method is designed to circumvent these difficulties.

### 3.1.1 Orthonormal Green functions

The method starts from the realization that the matrix-vector product (0) is valid at any observation point  $\mathbf{r}$ , and in particular at every point  $\mathbf{r}_s$ . If we introduce the inner product

$$\langle A, B \rangle = \int_S A^T B ds = \int_{R_{X_0}} A^T B ds + \int_{R_{X_1}} A^T B ds + \cdots, \quad (0)$$

where the integral is computed over the “sensitive” surfaces of the sensor, and if furthermore we can find a basis of Green functions orthogonal under this measure,

$$\mathbf{H}(\mathbf{r}_s) = \sum_{j=1}^M \Psi_j(\mathbf{r}_s) \mathbf{b}_j \quad \text{such that} \quad \langle \Psi_j, \Psi_k \rangle = F_j \delta_{jk}, \quad (0)$$

where  $\delta_{jk}$  is a Kronecker delta, then it is possible to find the source amplitudes  $\mathbf{b}_j$  without costly and ill-conditioned inversions simply by exploiting the sifting property of the orthogonal basis:

$$\langle \Psi_k, \mathbf{H} \rangle = \sum_{j=1}^M \langle \Psi_k, \Psi_j \rangle \mathbf{b}_j = \sum_{j=1}^M F_k \delta_{kj} \mathbf{b}_j = F_k \mathbf{b}_k \quad (0)$$

and thus

$$\mathbf{b}_k = F_k^{-1} \langle \Psi_k, \mathbf{H} \rangle, \quad (0)$$

which clearly does not involve solving a linear system of equations; it is necessary to invert only the  $6 \times 6$  matrix  $F_k$ . Moreover, this definition of the coefficients  $\mathbf{b}_j$  guarantees that they are “optimal” in the sense that the expansion (0) yields the least mean-square error  $\langle \mathbf{H} - \sum_{j=1}^M \Psi_j \mathbf{b}_j, \mathbf{H} - \sum_{j=1}^M \Psi_j \mathbf{b}_j \rangle$  [14].

To construct the set of orthonormal Green functions we resort to a generalization of the Gram-Schmidt procedure [15]. Assuming that the Green matrices are linearly independent—i.e., that we cannot have a collection of distinctly located dipole sources combining to produce no measurable field unless their amplitudes all vanish—we define

$$\begin{aligned} \Psi_1 &= G_1, \\ \Psi_2 &= G_2 - \Psi_1 A_{21}, \\ &\vdots \\ \Psi_m &= G_m - \sum_{k=1}^{m-1} \Psi_k A_{mk}, \\ &\vdots \\ \Psi_M &= G_M - \sum_{k=1}^{M-1} \Psi_k A_{Mk}, \end{aligned} \quad (0)$$

where the  $6 \times 6$  matrices  $A_{jk}$  obey  $A_{jk} = 0$  for  $j \leq k$ . Enforcing the orthogonality relation (0) is equivalent to setting  $\langle \Psi_n, G_m \rangle = F_n A_{nm}$  for  $n < m$ , and using this relation twice in definition (0) we find that

$$A_{mn} = F_n^{-1} \left( C_{nm} - \sum_{k=1}^{n-1} A_{nk}^T F_k A_{mk} \right), \quad (0)$$

where the overlap integral  $C_{mn} = \langle G_m, G_n \rangle$ .

At the end of the process it is necessary to recover an expansion expressed, like (0), in terms of the actual Green functions, in part because the functions  $\Psi_j$  are orthogonal (and defined) only at points on the receivers, and in part because of the non-uniqueness of the coefficients  $\mathbf{b}_j$  due to the arbitrary order in which the  $G_j$  enter the recursion (0). To that end, we express

$$\Psi_m = \sum_{k=1}^m G_k B_{mk}, \quad (0)$$

and to find the coefficients  $B_{mk}$  we compare expansion (0) term-by-term to the definition (0) and use the rule that  $A_{jk} = 0$  for  $j \leq k$  to find

$$\begin{aligned} B_{mm} &= I, \text{ the identity,} \\ B_{m(m-1)} &= -A_{m(m-1)}, \\ B_{mq} &= -\sum_{l=q}^{m-1} B_{lq} A_{ml} \text{ for } 1 \leq q \leq m-2, \end{aligned} \quad (0)$$

in terms of which we recover the physical polarizability elements:

$$\mathbf{H} = \sum_{k=1}^M \Psi_k \mathbf{b}_k = \sum_{k=1}^M \left( \sum_{l=1}^k G_l B_{kl} \right) \mathbf{b}_k = \sum_{l=1}^M G_l \left( \sum_{k=l}^M B_{kl} \mathbf{b}_k \right) = \sum_{l=1}^M G_l \mathbf{m}_l. \quad (0)$$

### 3.1.2 ONVMS procedure

With all the pieces in place, we can sketch an algorithm to invert EMI data using the ONVMS model:

- 1) Given a number of sources and their tentative locations, find the Green tensors  $G_i$  using the equation given in Appendix B in [8] and compute the overlap integrals  $G_{mn}$  using the inner product (0).
- 2) Determine the first normalization factor,  $F_1 = \langle G_1, G_1 \rangle$ , and use it to find all the Gram-Schmidt coefficients  $A_{mn}$  with  $n = 1$ :  $A_{m1} = F_1^{-1} C_{1m}$ .
- 3) Set  $m = 2$ ; compute, in sequence,
  - a) The coefficients  $A_{mn}$  with  $n = 2, \dots, m-1$  using equation (0);
  - b) The function  $\Psi_m$  using the expansion (0);
  - c) The normalization factor  $F_m = \langle \Psi_m, \Psi_m \rangle$ ;
 increase  $m$  by 1 and iterate until all sources have been included.
- 4) Once all the  $A_{mn}$ ,  $F_m$ , and  $\Psi_m$  are known, find  $B_{mq}$  using (0).
- 5) Use the orthonormality of the new Green functions to determine the source amplitudes using  $\mathbf{b}_q = F_q^{-1} \langle \Psi_q, \mathbf{H}^{\text{data}} \rangle$ , as in (0). Take the measured field to be piecewise constant—i.e., constant throughout each receiver—when evaluating the integrals.
- 6) Use the computed  $\mathbf{b}_q$ ,  $B_{mq}$ , and  $G_m$ , along with the expansion (0), to generate the secondary field prescribed by the given number of sources at the given locations.
- 7) Compare the model prediction with the measured data, vary the source locations, and iterate until the least-squares discrepancy between prediction and measurement attains a suitable minimum.

The procedure as written applies to only one time gate, but the extension to fully time-dependent functions is straightforward: we need only substitute the vectors  $\mathbf{b}_q$  and  $\mathbf{H}^{\text{data}}$  for two-dimensional arrays where the columns denote time. The relations between the two, namely (0) and (0), acquire multiple right-hand-sides, and the optimization mentioned on Step 7 of the algorithm is constrained further. As a final remark we note that rigorously speaking the

coefficients  $\mathbf{b}_q$  (and, for that matter, the amplitudes  $\mathbf{m}_k$ ) are *not* the polarizabilities themselves but relate more closely to their time derivatives [18]-[26].

The great advantage of the ONVMS technique is that it takes into account mutual couplings between different parts of targets and avoids matrix singularity problems in cases with multiple objects. Once the polarizability tensor elements and the locations of the elemental responding dipoles are determined one can group them according to their volume distribution. For each group a total polarizability tensor can be computed and diagonalized using joint diagonalization, the topic of Section 3.2. The resulting time-dependent diagonal elements have been shown to be intrinsic to the objects and can be used, on its own or combined with other quantities, in discrimination processing.

### **Joint diagonalization for multi-target data pre-processing**

In real-life situations the targets of interest are usually surrounded by natural and artificial debris with metallic content, including, for instance, the remains of ordnance that did explode. Thus it is usually not clear how many objects are producing a given detected signal; all sensing methods, including EMI, are fraught with detection rates that overwhelm cleanup efforts and hike their cost. Here we introduce a data pre-processing technique based on joint diagonalization (JD) that estimates the number of targets present in the field of view of the sensor as it takes a data shot, and, in a good number of cases, even provides the capability to perform real-time characterization and classification of the targets without the need for a forward model.

Joint diagonalization [9], [17] has become an important tool for signal processing and inverse problems, used as part of independent component analysis [13], blind source separation or BSS [14], common principal component analysis, and, more recently, kernel-based nonlinear BSS [15]. We further extend the applicability of the method by using it to detect and locate buried targets without the need for inversion. As we say above, a variation of the method can be used to extricate time-dependent electromagnetic signatures from attitude information. Here we outline the detailed procedure as applied to the TEMTADS sensor array, a time-domain device with 25 transmitter/receiver pairs that provides 625 measurements over  $N_g = 123$  time gates at each sensor location.

### 3.1.3 The multi-static response matrix

JD estimates the eigenvalues and eigenvectors of a square time- or frequency-dependent multi-static response (MSR) matrix synthesized directly from measured values. To construct the MSR matrices one just has to stack the 625 readings at each time gate in a  $25 \times 25$  array so that each column stands for one of  $N_t$  transmitters and each row represents one of  $N_r$  receivers:

$$\mathbf{S}(t_k) = \begin{bmatrix} H_{11} & H_{12} & \cdots & H_{1N_t} \\ H_{21} & H_{22} & \cdots & H_{2N_t} \\ \vdots & \vdots & \ddots & \vdots \\ H_{N_r1} & H_{N_r2} & \cdots & H_{N_rN_t} \end{bmatrix}, \quad (0)$$

where the element  $H_{ij}$  is the field measured by the  $i$ -th receiver when the  $j$ -th transmitter is fired. The second step of the procedure is to diagonalize the 123 matrices at one stroke so they all share a single set of orthonormal eigenvectors. In other words, given the MSR matrix  $\mathbf{S}(t_k)$  at the  $k$ -th time gate, we look for a unitary matrix  $\mathbf{V}$  such that the products

$$\mathbf{D}_k = \mathbf{V}^T \mathbf{S}(t_k) \mathbf{V} \quad (0)$$

are “as diagonal as possible” (i.e., their off-diagonal elements vanish within a preset tolerance). By diagonalizing all the matrices simultaneously we separate the time-dependent intrinsic features of the responding sources (and hence the interred objects), which get encapsulated in the eigenvalues, from the other factors—notably the location and orientation of the target with respect to the sensor—that influence the signal but do not change as the data are being taken; these get bundled into the eigenvectors. (The fact that the locations and orientations can be dissociated in this way from the electromagnetic signatures is an upside of the low frequencies of the quasistatic EMI range, because the relevant Green functions are time-independent.) Thus the measured data can be resolved as a superposition of “elemental” sub-signals, each corresponding to an elementary dipolar source, whose combination corresponds to the buried objects. Each source—and the corresponding field singularity—can moreover be localized numerically: the TEMTADS geometry is such that the diagonal of the unprocessed MSR matrix mimics a set of monostatic measurements, akin to those taken with a handheld sensor, which peak sharply when there is a target directly underneath. The maxima in the diagonal thus point to the

transmitter/receiver pairs closest to any responding sources. These location estimates can be grouped and correlated to the eigenvalue distributions to estimate target locations.

### 3.1.4 Interpretation and diagonalization of the MSR matrix

We now proceed to express our above considerations quantitatively. Initially we consider the transmitter assembly, which in TEMTADS consists of a set of coplanar square loops forming a regular grid. The Biot-Savart law gives the primary magnetic induction established at the location  $\mathbf{r}_i$  of the  $l$ -th source when the  $j$ -th transmitter antenna (whose area is  $\sigma_{\text{Tx}_j}$ ) is excited immediately before shutdown by a current  $I_j$ :

$$\mathbf{B}_{jl}^{\text{pr}} = \frac{\mu_0 I_j}{4\pi} \sigma_{\text{Tx}_j} \frac{1}{\sigma_{\text{Tx}_j}} \oint \frac{d\mathbf{l}' \times (\mathbf{r}_l - \mathbf{r}')}{|\mathbf{r}_l - \mathbf{r}'|^3} \equiv \mathbf{g}_{jl}^{\text{pr}} \sigma_{\text{Tx}_j} I_j, \quad \text{with} \quad \mathbf{g}_{jl}^{\text{pr}} \equiv \frac{\mu_0}{4\pi} \frac{1}{\sigma_{\text{Tx}_j}} \oint \frac{d\mathbf{l}' \times (\mathbf{r}_l - \mathbf{r}')}{|\mathbf{r}_l - \mathbf{r}'|^3}. \quad (0)$$

This primary field induces in the  $l$ -th source a dipole moment given by

$$\mathbf{m}_{jl} = \mathbf{U}_l \mathbf{\Lambda}_l \mathbf{U}_l^T \mathbf{B}_{jl}^{\text{pr}}, \quad (0)$$

where the Euler rotation matrix  $\mathbf{U}$  relates the instrument's coordinate axes to the principal axes of the source, and the diagonal polarizability matrix  $\mathbf{\Lambda}_i$ , the only quantity intrinsic to the source, measures the strength with which the primary field induces a moment along each of those axes.

According to Faraday's law, the signal measured by a receiver coil is the electromotive force given by the negative of the time derivative of the secondary magnetic flux through the coil. Since the field at point  $\mathbf{r}$  of a dipole of moment  $\mathbf{m}$  placed at  $\mathbf{r}_0$  is given by

$$\mathbf{B} = \frac{\mu_0}{4\pi} \nabla \times \left( \mathbf{m} \times \frac{\mathbf{r} - \mathbf{r}_0}{|\mathbf{r} - \mathbf{r}_0|^3} \right), \quad \text{and thus} \quad \int \mathbf{B} \cdot d\mathbf{s} = -\mathbf{m} \cdot \frac{\mu_0}{4\pi} \oint d\mathbf{l} \times \frac{\mathbf{r} - \mathbf{r}_0}{|\mathbf{r} - \mathbf{r}_0|^3} \quad (0)$$

by straightforward application of Stokes's theorem, one obtains that the signal sampled at time  $t_k$  by the  $i$ -th receiver (of area  $\sigma_{\text{Rx}_i}$ ) when the  $l$ -th source is excited by the  $j$ -th transmitter is

$$\begin{aligned} H_{ij}^l(t_k) \sigma_{\text{Rx}_i} \sigma_{\text{Tx}_j} I_j &= \frac{\mu_0}{4\pi} \sigma_{\text{Rx}_i} \frac{1}{\sigma_{\text{Rx}_i}} \oint \frac{d\mathbf{l}' \times (\mathbf{r}' - \mathbf{r}_l)}{|\mathbf{r}' - \mathbf{r}_l|^3} \cdot \dot{\mathbf{m}}_{jl}(t_k) = \mathbf{g}_{il}^{\text{sc}} \sigma_{\text{Rx}_i} \cdot \dot{\mathbf{m}}_{jl}(t_k) \\ &= \mathbf{g}_{il}^{\text{sc}} \sigma_{\text{Rx}_i} \cdot [\mathbf{U} \dot{\mathbf{\Lambda}}_l(t_k) \mathbf{U}^T] \cdot \mathbf{g}_{jl}^{\text{pr}} \sigma_{\text{Tx}_j} I_j, \end{aligned} \quad (0)$$

where a dot over a variable indicates its time derivative. In equations (0) and (0) the line element  $d\mathbf{l}'$  lies on the  $x$ - $y$  plane. Note that we have included the exciting current  $I_j$  and the transmitter and receiver areas in the definition of the signal; we have explicit knowledge of these quantities and can factor them out. If only the  $l$ -th source is illuminated, we construct the MSR matrix for the complete transmitter/receiver array by tiling  $N_r \times N_t$  instances of the expression (0):

$$\mathbf{S} = \mathbf{G}^{\text{sc}} \mathbf{U}_l \mathbf{\Lambda}_l \mathbf{U}_l^T (\mathbf{G}^{\text{pr}})^T, \quad (0)$$

where the primary (or transmitter) dyad  $\mathbf{G}^{\text{pr}}$  is of size  $N_t \times 3$ , the secondary (or receiver) dyad  $\mathbf{G}^{\text{sc}}$  is of size  $N_r \times 3$ , and the response matrix  $\mathbf{U} \mathbf{\Lambda} \mathbf{U}^T$  is  $3 \times 3$ . When there is more than one source present, the MSR matrix of equation (0) is readily generalized:

$$\begin{aligned} \mathbf{S} &= \begin{bmatrix} \mathbf{G}_1^{\text{sc}} & \mathbf{G}_2^{\text{sc}} & \cdots \end{bmatrix} \begin{bmatrix} \mathbf{U}_1 \dot{\mathbf{\Lambda}}_1 \mathbf{U}_1^T & 0 & \cdots \\ 0 & \mathbf{U}_2 \dot{\mathbf{\Lambda}}_2 \mathbf{U}_2^T & \cdots \\ \vdots & \vdots & \ddots \end{bmatrix} \begin{bmatrix} (\mathbf{G}_1^{\text{pr}})^T \\ (\mathbf{G}_2^{\text{pr}})^T \\ \vdots \end{bmatrix} \\ &= \begin{bmatrix} \mathbf{G}_1^{\text{sc}} \mathbf{U}_1 & \mathbf{G}_2^{\text{sc}} \mathbf{U}_2 & \cdots \end{bmatrix} \begin{bmatrix} \dot{\mathbf{\Lambda}}_1 & 0 & \cdots \\ 0 & \dot{\mathbf{\Lambda}}_2 & \cdots \\ \vdots & \vdots & \ddots \end{bmatrix} \begin{bmatrix} (\mathbf{G}_1^{\text{pr}} \mathbf{U}_1)^T \\ (\mathbf{G}_2^{\text{pr}} \mathbf{U}_2)^T \\ \vdots \end{bmatrix}, \end{aligned} \quad (0)$$

where we see that the features intrinsic to the targets can be separated formally from the particulars of the measurement—that is, from the geometry and dimensions of the sensor and the sensor-target attitude. The array  $\mathbf{S}$  has size  $N_r \times N_t$  and is square if  $N_r = N_t$ , as is the case with TEMTADS. This allows us to diagonalize the matrix but does not suffice to guarantee that the extracted information is useful—i.e., that the eigenvalues and eigenvectors are real, and that the latter are orthonormal. For that to hold we must have a real, symmetric matrix, which requires  $\mathbf{G}_l^{\text{sc}} = \mathbf{G}_l^{\text{pr}} \equiv \mathbf{G}_l$ . This cannot be rigorously true, because the receivers cannot coincide exactly with the transmitters, but holds approximately for TEMTADS if we factor the exciting current and the coil areas out of  $\mathbf{S}$ , as we did in equation (0). The diagonalization we perform is thus a particular case of singular value decomposition (SVD), and in what follows we use “diagonalization” as shorthand for “SVD of a symmetric matrix.”

The decomposition (0) exhibits the actual polarizability elements but is not directly available to us because the Green tensors are not orthogonal. To see what we do get when we diagonalize  $\mathbf{S}$  we can perform the SVD on  $\mathbf{G}$ :

$$\mathbf{S} = \mathbf{G}\mathbf{U}\mathbf{\dot{\Lambda}}\mathbf{U}^T\mathbf{G}^T = \mathbf{W}\left[\mathbf{\Sigma}\mathbf{V}^T\mathbf{U}\mathbf{\dot{\Lambda}}\mathbf{U}^T\mathbf{V}\mathbf{\Sigma}\right]\mathbf{W}^T = \mathbf{W}\mathbf{Z}\mathbf{\Delta}\mathbf{Z}^T\mathbf{W}^T = \mathbf{Y}\mathbf{\Delta}\mathbf{Y}^T \quad (0)$$

In the intermediate step we have used the fact that the matrix within the brackets is real and symmetric and thus has a purely real eigendecomposition. Result (0) shows that the eigenvalue matrix  $\mathbf{\Delta}$ , though time-dependent, is not solely composed of source responses, but also contains location and orientation information extracted from the Green tensors. The eigenvectors, likewise, include information from both the polarizabilities and the measurement particulars.

We also see in the decomposition (0) that  $\mathbf{S}$  contains an unknown “hidden dimension”— $3N$ , where  $N$  is the number of sources—in the size of the block-diagonal response matrix. Numerical diagonalization (or, in general, the SVD) of  $\mathbf{S}$  imposes this middle dimension to be  $N_r = N_t$ . Ideally, the method should be able to resolve up to  $\lfloor N_r / 3 \rfloor$  responding sources, or eight for TEMTADS, but the actual number is lower. For one, the procedure resolves targets only when they are spatially separated: two distinct dipoles sharing one location decrease the rank of the  $\mathbf{G}$  matrices, and hence of  $\mathbf{S}$ , by 3. In any case, diagonalization of  $\mathbf{S}$  can again let us estimate the number of responding dipole sources illuminated by the sensor; since the only time-dependent quantities are the intrinsic polarizabilities of the sources, we expect the additional information provided by the time decay of the eigenvalues to be useful for classification.

The development outlined above corresponds to each time gate taken separately. To make sense of the time-dependent information we have to find a way to “follow” each of the eigenvalues as the signal decays. (A similar process must be carried out when using the dipole model for inversion.) One could in principle diagonalize the MSR matrix at each time channel, and the eigenvectors, which depend only on geometry and pose, should stay constant; however, it is not possible to know a priori the order in which the eigenvalues will be given by the diagonalization; this fact—not to mention noise and experimental uncertainty—makes it inevitable to have to disentangle the tensor elements by hand, which is easily done wrong. Instead, we explicitly look for an orthogonal matrix of eigenvectors that diagonalizes all the MSR matrices simultaneously. The procedure we employ is a generalization of the method for single matrices, and is well known; it is illustrated in the next Section.

### 3.1.5 Algorithm for joint diagonalization

The joint diagonalization algorithm we use [9], [16], [17] is a generalization of Jacobi's procedure to find the eigenvalues of a single matrix. Formally we set out to solve the optimization problem

$$\begin{aligned} \min_V \quad & \frac{1}{2} \sum_{q=1}^{N_g} \sum_{i \neq j} ([VA(t_q)V^T]_{ij})^2 \\ \text{s.t.} \quad & V^T V = I, \end{aligned} \quad (0)$$

which we accomplish by making repeated Givens-Jacobi similarity transformations designed to gradually accumulate the “content” of the matrices on their diagonals until a certain tolerance level is reached. The transformations are of the form  $A(t_q) \rightarrow A'(t_q) = V_{rs} A(t_q) V_{rs}^T$ , with the matrix  $I = V_{rs}^T V_{rs}$  being the identity but with the four elements  $V_{rr}$ ,  $V_{rs}$ ,  $V_{sr}$ , and  $V_{ss}$  replaced by the two-dimensional rotation array

$$\begin{bmatrix} \cos \phi_{rs} & \sin \phi_{rs} \\ -\sin \phi_{rs} & \cos \phi_{rs} \end{bmatrix}, \quad \text{with} \quad \tan 2\phi_{rs} = \frac{f_{rs}}{n_{rs} + \sqrt{f_{rs}^2 + n_{rs}^2}}, \quad (0)$$

where

$$n_{rs} = \sum_q \{ [a_{rr}(t_q) - a_{ss}(t_q)]^2 - [a_{rs}(t_q) + a_{sr}(t_q)]^2 \}, \quad (0)$$

$$f_{rs} = 2 \sum_q [a_{rr}(t_q) - a_{ss}(t_q)][a_{rs}(t_q) + a_{sr}(t_q)]. \quad (0)$$

The indices are swept systematically, and the procedure is repeated until convergence is reached. The computational burden is equivalent to that of diagonalizing the matrices one by one. The resulting eigenvalues and eigenvectors are all real because all the MSR matrices are symmetric.

### MUSIC algorithm

The MUSIC algorithm was developed for antenna studies [27] and has been applied to other related fields, including location of subsurface objects [28]-[31].

To apply it here, choose an MSR matrix corresponding to one time channel and perform the singular value decomposition (SVD),

$$\mathbf{S} = \mathbf{U}\mathbf{\Sigma}\mathbf{V}^T, \quad (0)$$

where  $\mathbf{\Sigma}$  is an  $N \times N$  diagonal matrix in which the singular values are arranged in descending order, and  $\mathbf{U} = [u_1, u_2, \dots, u_N]$  and  $\mathbf{V} = [v_1, v_2, \dots, v_N]$  are matrices that contain the corresponding singular vectors.

First, we assume that the MSR matrix comes from  $n$  dipole-represented objects, giving us  $r = 3 \times n$  significant singular values in  $\mathbf{\Sigma}$  (here we assume that we have sufficient Tx and Rx that  $r < N$ ). For the TEMTADS system, the theoretical maximum number of objects it can handle is  $n = 8$ ). Thus  $\mathbf{U}_s = [u_1, u_2, \dots, u_r]$  and  $\mathbf{V}_s = [v_1, v_2, \dots, v_r]$  form the signal subspace while  $\mathbf{U}_n = [u_{r+1}, u_2, \dots, u_N]$  and  $\mathbf{V}_n = [v_{r+1}, v_2, \dots, v_N]$  form the noise subspace.

The error matrix is built as

$$\mathbf{P} = \mathbf{I} - \mathbf{E}_s \mathbf{E}_s^T, \quad (0)$$

in which  $\mathbf{E}_s = \mathbf{U}_s$  or  $\mathbf{V}_s$ .

The Green function array is normalized and projected onto the error matrix:

$$\mathbf{W}_s = \mathbf{P} \frac{\mathbf{G}}{\|\mathbf{G}\|}. \quad (0)$$

Due to the orthogonality between signal and noise subspace, we can expect the outcome to be zero at the correct location. In actual cases, however, in the presence of noise and errors, zero can never be achieved exactly. To evaluate how close the outcome is to zero, and thus how well the orthogonality is, we introduce the  $\mathbf{F}$  function by inverting the length of the vector produced above:

$$\mathbf{F} = \frac{1}{\|\mathbf{W}_s\|} \quad (0)$$

Calculating  $\mathbf{F}$  for each discretized point in the search region returns peaks at those locations where orthogonality is most closely matched.

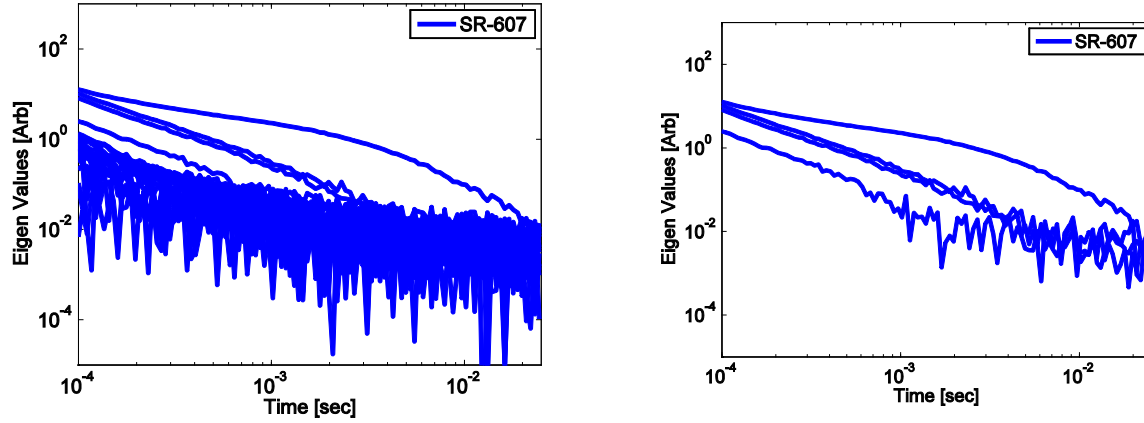


Figure 2. An example case of JD applied to the data of SR-607, a 37-mm projectile from Spencer Range. Plotted on the left are the eigenvalues, of which 4 can be identified above the noise level. On the right shows the proposed way of filtering.

### 3.1.6 Combined JD-MUSIC algorithm

JD is a numerical technique that finds a single group of eigenvectors that can diagonalize the entire set of MSR matrices as well as possible. The procedure allows us to identify the time-independent factors in the transient response and to track each eigenvalue separately as a function of time.

To begin, we construct a set of sensor-specific MSR data matrices and numerically find eigenvectors  $\mathbf{Y}$  such that

$$\mathbf{S}(t_k) = \mathbf{Y} \mathbf{D}_k \mathbf{Y}^T, \quad k=1,2,\dots, N_g, \quad (0)$$

with  $\mathbf{D}_k$  as diagonal as possible:

$$\mathbf{D}_k = \text{diag}[\mathbf{d}_{11}, \mathbf{d}_{12}, \dots, \mathbf{d}_{nn}]. \quad (0)$$

Once the  $\mathbf{D}_k$  eigenvalues are determined, the data is de-noised by artificially setting the eigenvalues found in JD to be zero if they are below the noise threshold  $d_{th}$ :

$$\mathbf{D}'_k = \text{diag}[\mathbf{d}_{11}, \mathbf{d}_{12}, \dots, \mathbf{d}_{th}, 0, \dots, 0]. \quad (0)$$

The filtered data matrices are then reconstructed from the filtered eigenvalue matrix

$$\mathbf{S}(t_k) = \mathbf{Y} \mathbf{D}'_k \mathbf{Y}^T, \quad k=1,2,\dots, N_g. \quad (0)$$

The filtered data matrices are then passed to the MUSIC algorithm, along with the estimated number of sources,  $r$ . This eigenvalue de-noising technique is depicted on Figure 2.

### **Automated separation of signal and noise eigenvalues in JD**

The separation of signal against noise is a critical step before the MUSIC algorithm can be applied. The speed advantage of the MUSIC algorithm cannot be utilized if the signals in JD need to be handpicked. To make this process automatic, we employ the Pasion-Oldenburg power-law decay model also used in UXO classification to fit eigenvalue curves:

$$\text{Eig}(t) = kt^{-b} e^{-gt}. \quad (0)$$

Also, we introduce the average fitting error  $\sigma^2$  as a measure of fluctuations in eigenvalue curves:

$$\sigma^2 = \frac{1}{n} \sum (\log \text{Eig}_{\text{Data}} - \log \text{Eig}_{\text{fit}})^2. \quad (0)$$

After extracting the  $k$ ,  $b$ ,  $g$ , and  $\sigma^2$  parameters from each eigenvalue decay curve using least squares and plotting them on  $(\log k)$ - $b$  space, one can observe the different patterns of distribution between signal and noise eigenvalues. Among them, the most noticeable feature is the straight line formed by the low-magnitude and slowly decaying noise eigenvalue, which can be seen in Figure 3. In response we developed the following strategy to classify between signal and noise: 1) First we found clear signal eigenvalues through their high  $k$ ,  $b$ ,  $g$  and low  $\sigma^2$ , as well as clear noise eigenvalues through their low  $k$ ,  $b$ ,  $g$  and high  $\sigma^2$ . 2) We then identified eigenvalues belonging to the same straight-line cluster as the evident noise eigenvalues found in the previous step, and marked them also as noise. 3) Finally, for the rest of the untagged eigenvalues in “the gray area”, we simply classified them as signal, since we did not want to miss any, and because there is no clear answer in the gray area even for human experts.

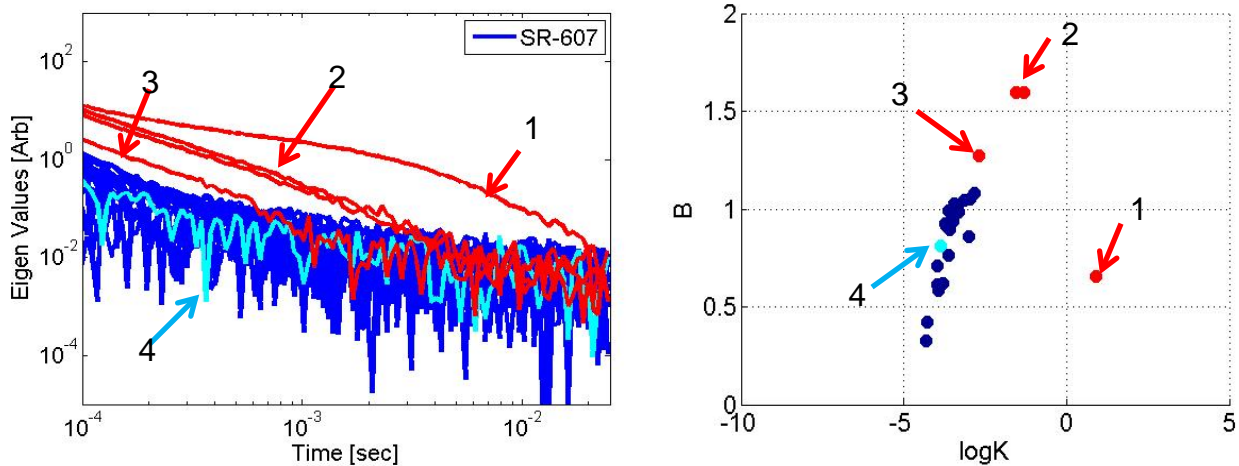


Figure 3. Example of typical signal and typical noise eigenvalues chosen from the same case as in Figure 2 (left) and where they landed on the  $(\log k)-b$  space (right). The  $(\log k)-b$  distribution on the right is classified for signal (red dots) and noise (cyan and blue dots).

### EMI data inversion: A global optimization technique

Determining a buried object's orientation and location is a nonlinear problem. Inverse-scattering approaches are carried out by determining an objective function [18]-[24] as a goodness-of-fit measure between the primary  $\mathbf{H}^{\text{pr}}$  and measured  $\mathbf{d}^{\text{m}}$  magnetic field data. In many cases, the standard gradient-search approaches suffer from an excess of local minima that often lead them to inverting incorrect values for location and orientation. To avoid this problem we recently developed a different class of global optimization search algorithms, including differential evolution (DE) [3], [32]–[33]. DE is a heuristic, parallel, direct-search method for minimizing non-linear functions of continuous variables that is very easy to implement and has excellent convergence properties. We combined the DE algorithm with the ONVMS technique discussed above to invert digital geophysical EMI data [3], [12], taking particular care to split the entire EMI optimization into two parts, linear and nonlinear. For any position, the scattered field from any object depends linearly on the responding source magnitudes. Initially, EMI data are used to determine the amplitudes of the responding ONVMS using the orthonormalization process for each DE iteration, and the positions of the objects are subsequently estimated by minimizing an

objective function. The algorithm iterates between these two parts to minimize an objective function consisting of the difference between measured and modelled data. The target positions thus found are used to determine the amplitudes of the responding ONVMS and to classify the object relative to items of interest.

### **Discrimination parameters**

In this report we use the ONVMS model for live-site UXO discrimination, combining it with the joint diagonalization and optimization search algorithms to invert for the locations and orientations of targets of interest. The models provide at least three independent total ONVMS parameters (each one along a principal axis) for each potential target, parameters that can be used for discrimination. During the inversion stage the total ONVMS (and its time evolution), which depends on the size, geometry, and material composition of the object in question, is determined as a function of time for each potential target. Early time gates bring out the high-frequency response to the shutdown of the exciting field; the induced eddy currents in this range are superficial, and a large total ONVMS amplitude at early times correlates with large objects and large surface area. At late times, when the eddy currents have diffused completely into the object and low-frequency harmonics dominate, the EMI response relates to the metal content (i.e., the volume) of the target. Thus a smaller but compact object has a relatively weak early response that dies down slowly, while a large but thin or hollow object has a strong initial response that decays quickly. These parameters form feature vectors for classification algorithms [34]–[40].

## 4 Results

This section provides numerical and experimental results for Metal Mapper,  $5 \times 5$  and  $2 \times 2$  TEMTADS test-stand and in field data sets. The data are processed using the ONVMS, JD and MUSIC algorithms. The comparisons between estimated and actual locations are demonstrated. Our studies showed that the ONVMS technique is robust for deep target detection and classification.

### $5 \times 5$ TEMTADS test-stand cases

The JD-MUSIC combined algorithm has been applied to a set of TEMTADS test-stand data arising from UXO and spheroids (which represent clutter), collected in January of 2010. The experiment setup is shown in Figure 4. The TEMTADS sensor was placed atop a frame structure and the testing objects were distributed beneath the sensor on non-metallic shelves. The numerical search was carried out in a region of size  $2 \text{ m} \times 2 \text{ m} \times 1 \text{ m}$ , discretized by a grid spacing of 3 cm.



Figure 4. Test-stand setup showing three targets: a 105-mm shell, a 60-mm mortar (center, half-shrouded), and an aluminum spheroid (top left).

We first extracted the time-dependent eigenvalues for the background data shots and determined the  $k$ ,  $b$ ,  $g$ , and  $\sigma^2$  feature parameters that characterized the noise. These parameters were kept in memory and used for separating signal from noise: eigenvalues with high  $k$ ,  $b$ , and  $g$  and low  $\sigma^2$  were considered to be signal-related.

We begin with a single object case containing a 105-mm shell placed 63 cm below the center of the sensor, with nose oriented toward the positive  $x$ -axis. JD finds seven eigenvalues above the noise level (Figure 5) because the 105-mm is too big to be describable by one dipole. The eigenvalues have shown good separation between signal and noise in  $(\log k)$ - $b$  space. The automatic separation correctly identifies all seven signal eigenvalues without difficulty (Figure 6) and then sends the filtered data to the MUSIC algorithm (Figure 7), which then provides peaks of the  $F$  function around the ground-truth location of  $(0, 0, -63)$  cm marked by the cross. The best orthogonality is found at  $(-15, 0, -60)$  cm. The location error is 3 cm vertically (one grid) and 15 cm horizontally in the  $x$ -axis, which agrees with the fact that the munition is placed along the  $x$ -axis. The peak of the  $F$  function determines the number of responding sources needed to represent the measured signal.

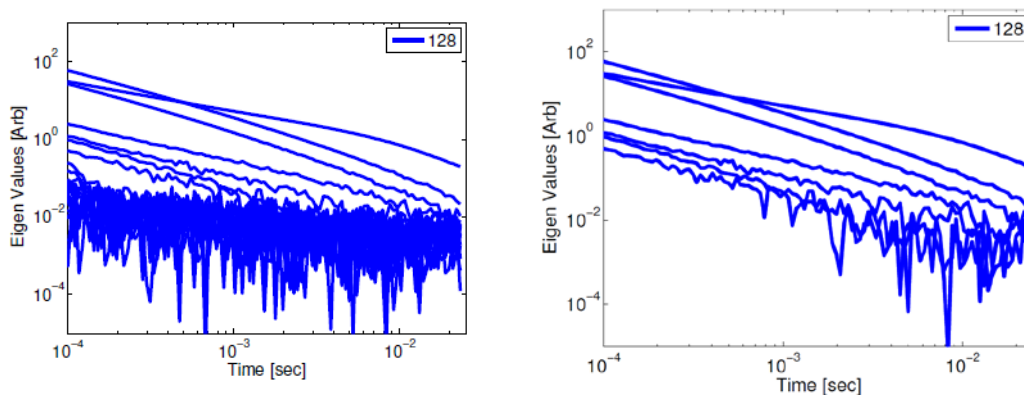


Figure 5. Eigenvalues of the 105-mm shell test-stand data from JD, unfiltered on the left and automatic-filtered on the right.

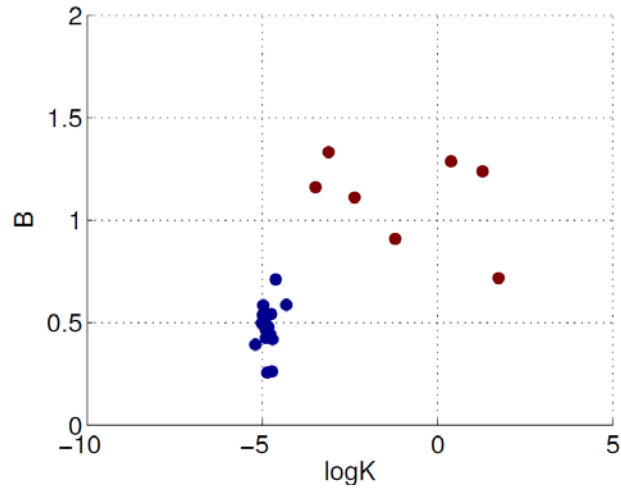


Figure 6. Eigenvalue distribution of the 105-mm test-stand case in  $(\log k)$ - $b$  space with automated classification into signal (red) and noise (blue) results.

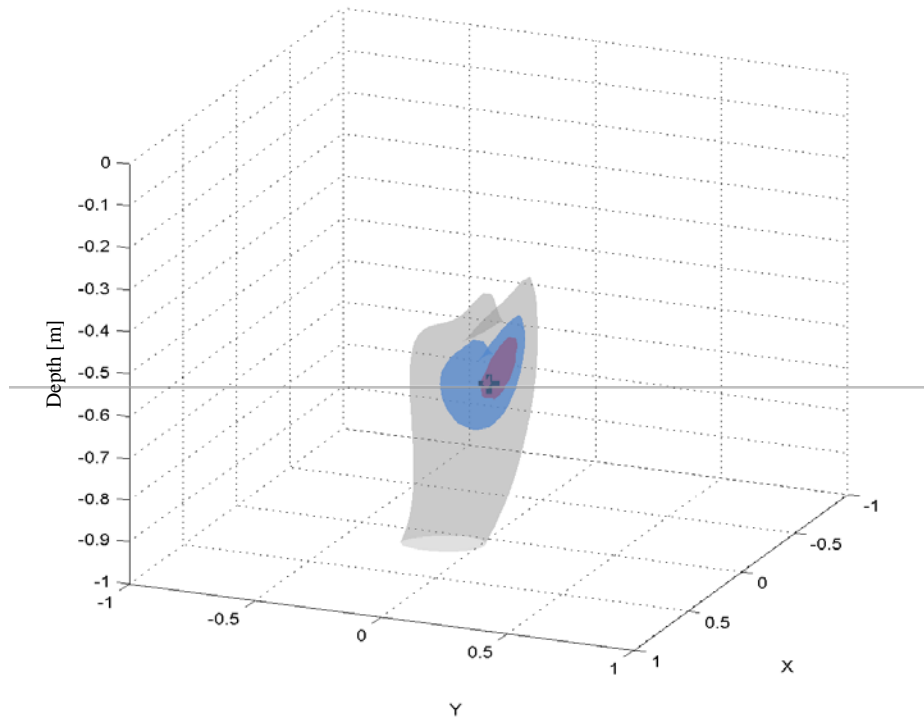


Figure 7. Contour surfaces of the  $F$  function for the 105-mm test-stand case. Red, blue, and gray show 70%, 50%, and 30% of the maximum value, respectively. The true location is marked by the cross.

Next we considered a scenario with three targets. In this case, the objects are a the 105 mm shell at (0, 0, -63) cm, a 60-mm mortar at (0, -40, -38) cm, and an aluminum spheroid at (20, 20, -27.5) cm. The automatic separation algorithm for signal and noise eigenvalues (described in Section 3.5) using  $k$ ,  $b$ ,  $g$  and  $\sigma^2$  features identifies 11 eigenvalues to be signal-related (Figure 8 and Figure 9). Even though one of the noise eigenvalues appears close to a signal eigenvalue in  $(\log k)$ - $b$  space (see Figure 9), the algorithm is able to use the error  $\sigma^2$  to discriminate between signal eigenvalues with low  $\sigma^2$  and noise eigenvalues with high  $\sigma^2$ . Filtering out the noise identified by automatic separation and searching with  $r = 11$  in MUSIC finds three peaks at (-6, 0, -60) cm, (3, -39, -42) cm, and (21, 24, -27) cm, respectively, as shown in Figure 10. The location of all three targets agreed within 2 grid separations, or 6 cm.

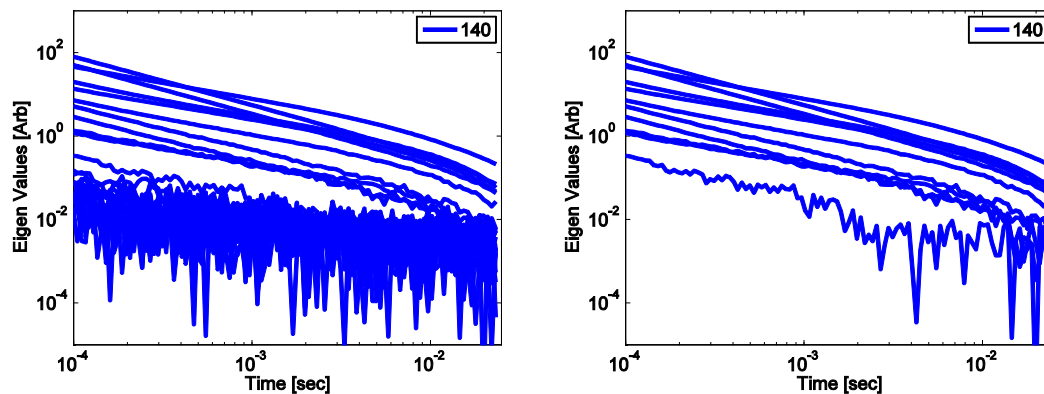


Figure 8. Eigenvalues of the three-object test-stand case, unfiltered on the left and filtered on the right.

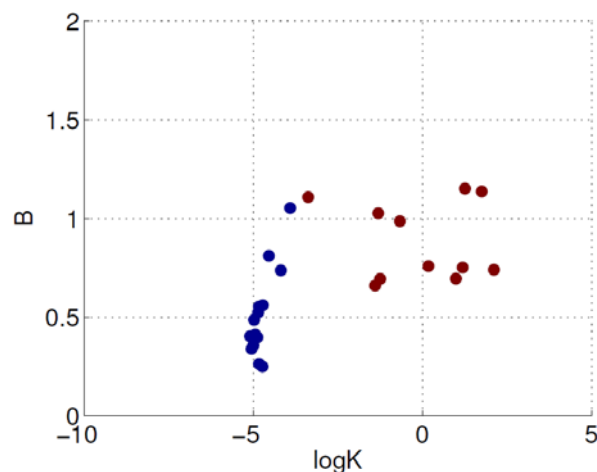


Figure 9. Signal (red) and noise (blue) classification results for the three-object test-stand case.

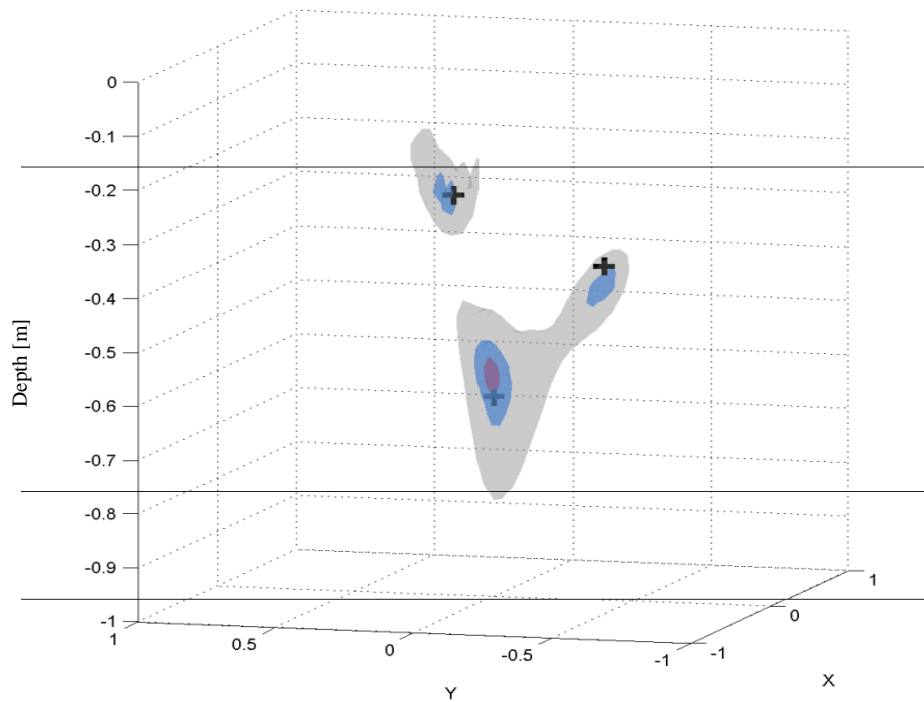


Figure 10. Peaks found by MUSIC algorithm displayed using the contour surface of  $F$  from (0). The ground truth locations are marked out by the three crosses. Red, blue, and gray show 70%, 50%, and 30% of the maximum value, respectively. The true location is marked by the cross.

Next is another set of test-stand data corresponding to a single 37-mm projectile placed at a depth of 61 cm. This low-SNR case validates the effectiveness of JD de-noising in this application. The target location is found using the MUSIC algorithm, both with and without applying JD filtering (compare with Figure 11). The peak is calculated to be at a depth of 75 cm, with an error of 14 cm. After the noisy eigenvalues are removed, the peak is found at a depth of 66 cm, and the depth error reduces to 5 cm, which is within 2 grid spacings, as shown in Figure 12. The contour surfaces in the filtered results are also much more densely packed, which is an indication of the sharper peak and the better orthogonality achieved.

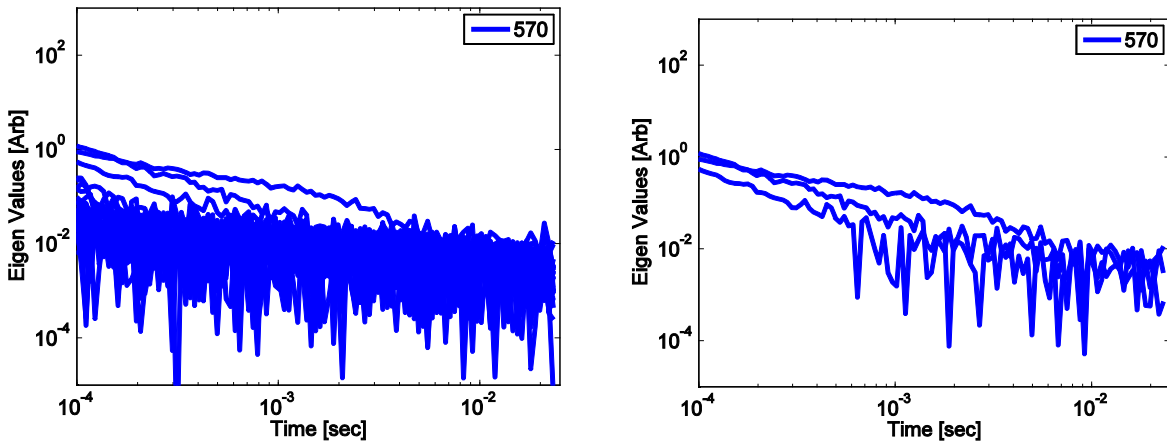


Figure 11. Eigenvalues of the 37-mm test stand case, unfiltered on the left and filtered on the right. The SNR in this case is noticeably lower, evidencing that signal eigenvalues on the left are not as high above the noise level as in other examples.

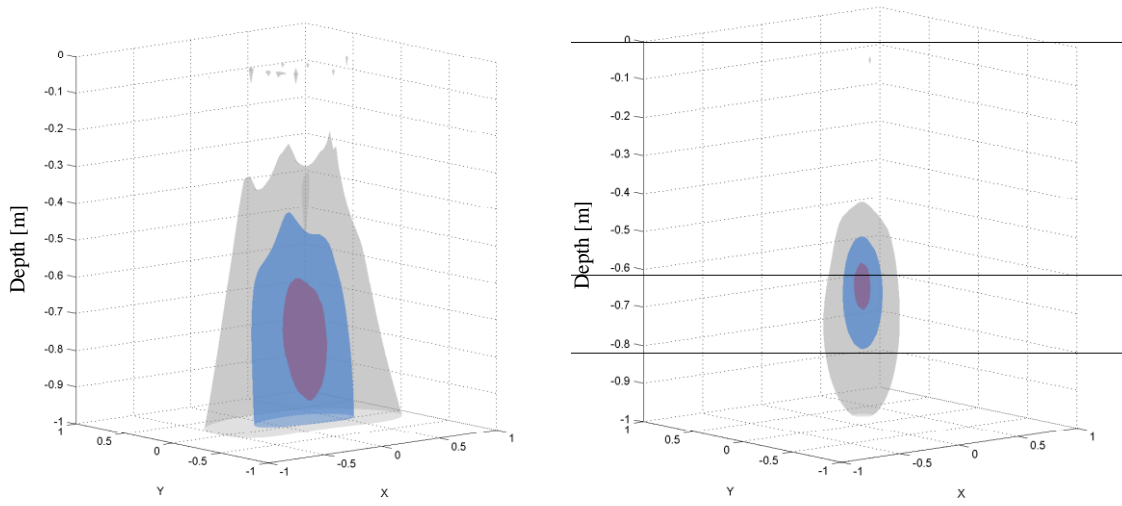


Figure 12. Location found using the MUSIC algorithm, unfiltered on the left and filtered on the right. Red, blue, and gray show 70%, 50%, and 30% of the maximum value, respectively.

## 5 × 5 TEMTADS field test cases

The method was then applied to live-site data taken at the Spencer Artillery Range in Spencer/Van Buren County, TN. Figure 13 shows the time-dependent eigenvalues for anomaly SR-614, a 37-mm projectile (Figure 14). The automatic signal separation algorithm identifies five eigenvalues with higher  $k$ ,  $b$ , and  $g$  and lower  $\sigma^2$  than the Spencer range background data eigenvalues (Figure 15). The filtered signal generated using the five signal-related eigenvalues was passed to the MUSIC algorithm, which in return provided the peaks of the  $F$  function (Figure 16). The result shows that the maximum of the  $F$  function (red surface) is 36 cm under the center of the TEMTADS sensor. The ground truth for this target is reported to be 21 cm into the ground. With the gap between ground and sensor known to be around 10 cm (note the uncertainty in this number, due to the roughness of ground surface), this gives a total separation from the sensor of about 31 cm. These data were also inverted using differential evolution, which predict a depth of 33 cm below the sensor. The three inverted depth values agree well. The surface corresponding to 50% of the  $F$  function maximum shows additional peaks close to the edges of TEMTADS. These peaks could be related to nearby targets or noise.

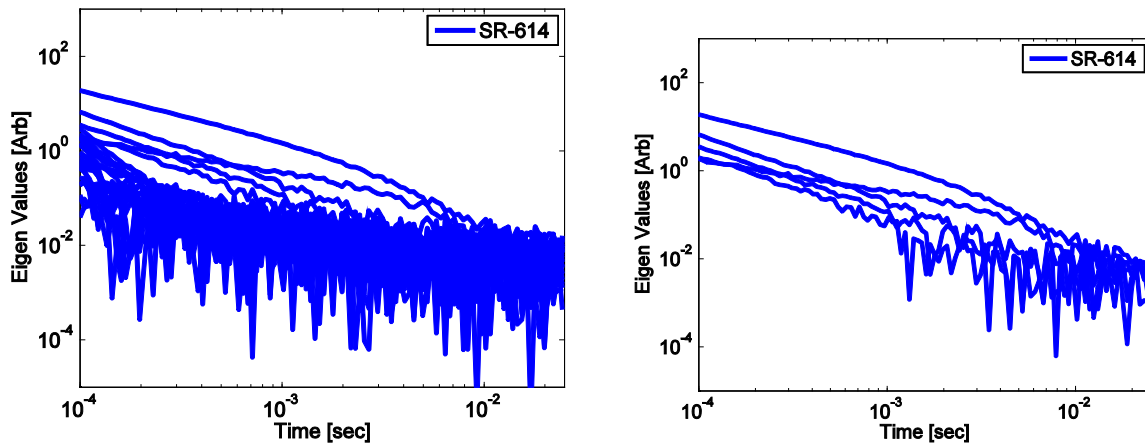


Figure 13. Eigenvalues of the SR-614 anomaly, unfiltered on the left and filtered on the right.

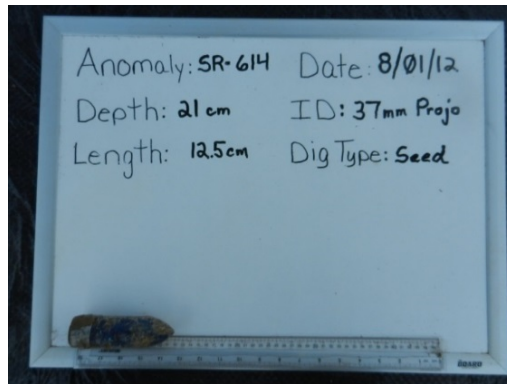


Figure 14. Ground truth photo of anomaly SR-614.

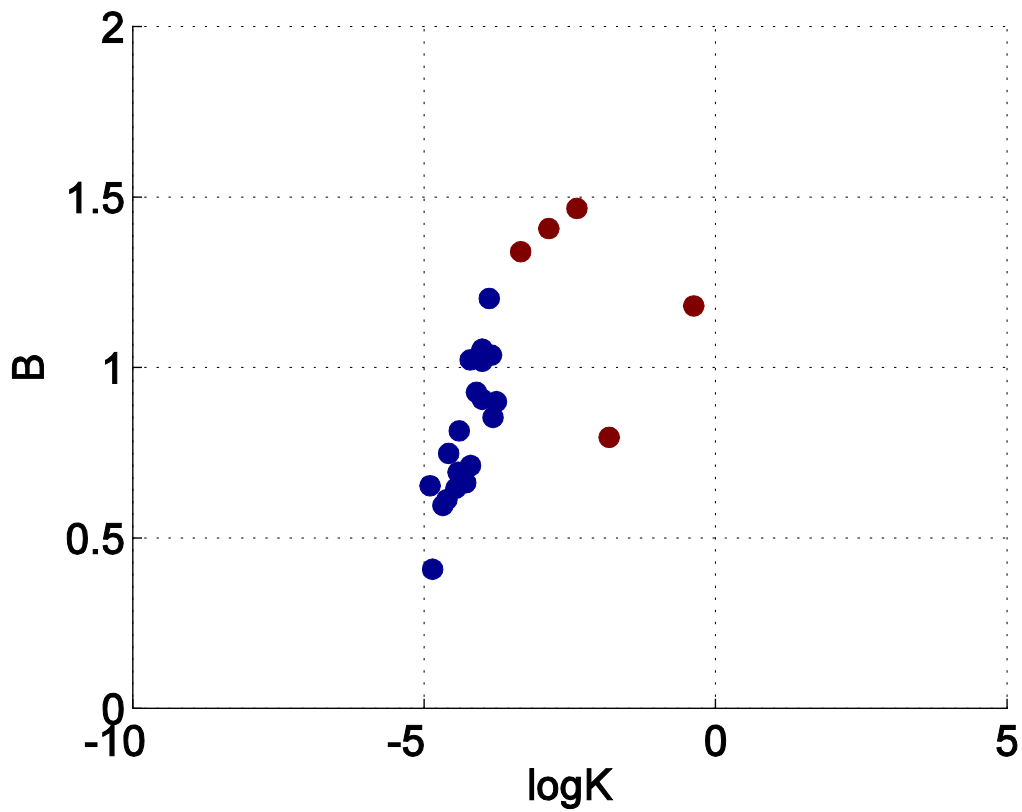


Figure 15. Signal (red) to noise (blue) classification result for anomaly SR-614.

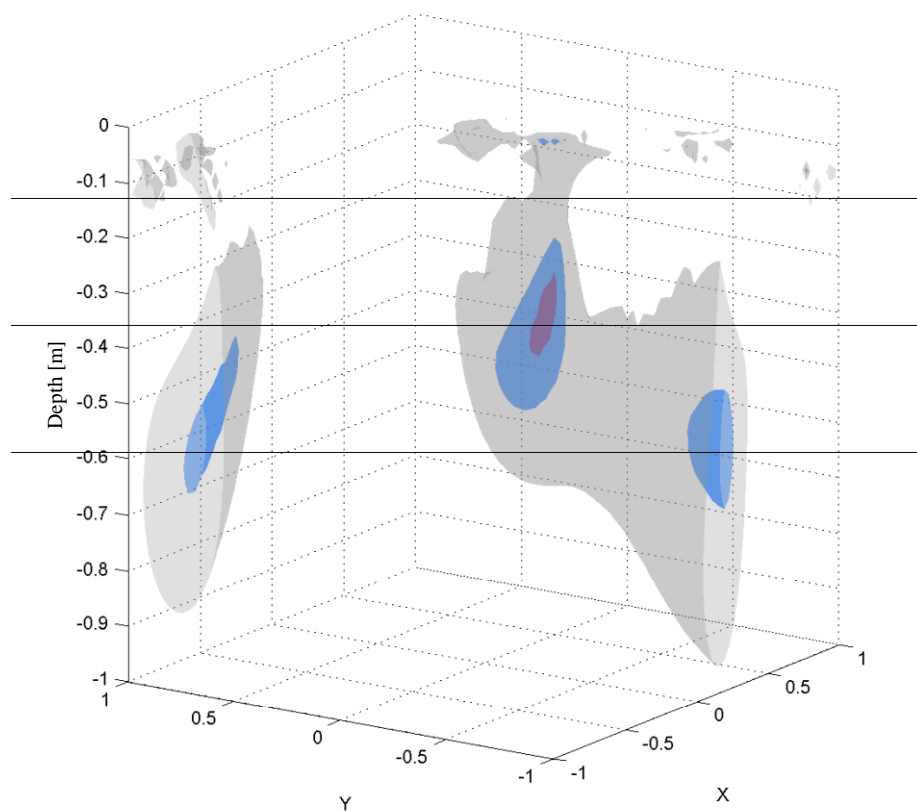


Figure 16. Target location found by the MUSIC algorithm for SR-614. Red, blue and, gray show 70%, 50%, and 30% of the maximum value, respectively.

## **Combined joint diagonalization-MUSIC algorithm applied to $2 \times 2$ TEMTADS Test-stand and field results**

The above approach was applied to test-stand data in which the target was a 37-mm projectile placed at a depth of 46.5 cm. The search was carried out in a region directly covered by the TEMTADS sensor with 1 m depth, which is  $-40$  cm to  $40$  cm for  $x$  and  $y$ , and  $-2.5$  cm to  $-100$  cm for  $Z$ , with a grid spacing of  $2.5$  cm, resulting in a grid of  $33 \times 33 \times 40$  in the search region. The data in the 10th time channel (recorded  $0.3$  ms after Tx-current turnoff) was used for maximum SNR, as well as to avoid ringing from the Tx and Rx coils at the earliest time channels. The maximum is found at location  $(-10, -10, -45)$  cm.

The filtered and unfiltered eigenvalues are depicted on Figure 17. Due to the limited number of sensors, the  $2 \times 2$  TEMTADS static data does not provide very high spatial resolution. This can be observed from the cone region in Figure 18, similar to that of a shadow cast in the presence of few light sources.

For the described case, the SNR is good enough to run MUSIC correctly without denoising in JD (Figure 17). When the 37-mm shell is placed deeper, at  $86$  cm in depth, filtering begins to make a difference (Figure 19). MUSIC finds the highest peak at  $z = -60$  cm for unfiltered data, while for filtered data in JD, the maximum moved to location  $(-17.5, -22.5, -92.5)$  cm, much closer to the ground truth depth of  $86$  cm (Figure 20).

Finally, the method was applied to live-site data taken at Spencer Artillery Range. Figure 21 shows unfiltered and filtered JD for anomaly SR-2059, a 37-mm projectile. The ground truth for this target is  $17.5$  cm in depth and  $24$  cm from the center of the sensor in an unknown direction. MUSIC in this case gives peak coordinates of  $(17.5, -27.5, -12.5)$  cm, which is  $12.5$  cm in depth and  $32.6$  cm from the center (Figure 22).

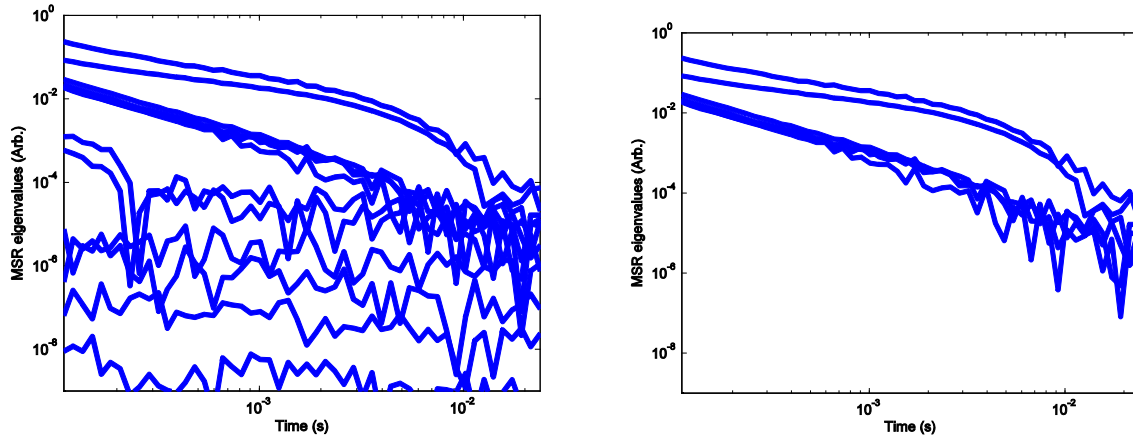


Figure 17. Eigenvalues for the 37 mm projectile at a depth of 46.5 cm before (left) and after (right) the filtering process in JD. The characteristic curve of the 37 mm projectile can be identified.

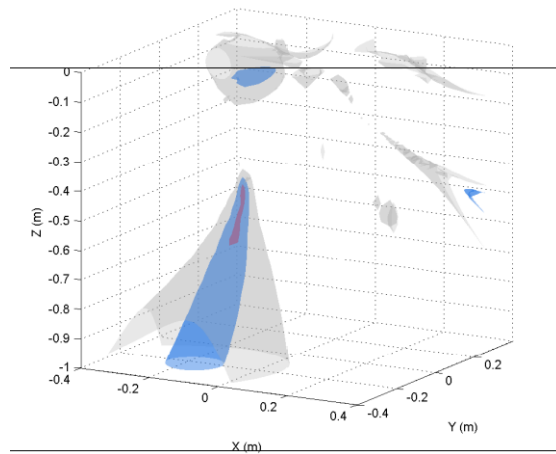


Figure 18. The  $F$  function of the MUSIC algorithm plotted in the search region. Gray, blue, and red show the contour surfaces of 60%, 75%, and 90% of the maximum value, respectively.

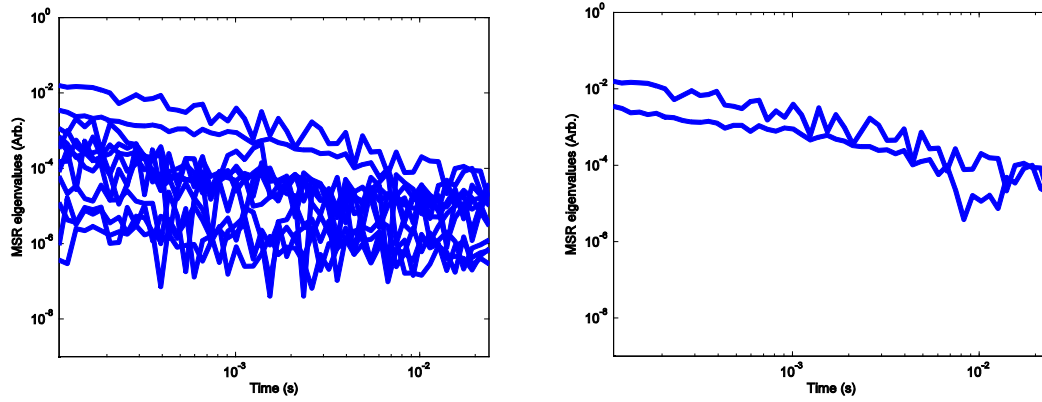


Figure 19. Eigenvalues for a 37-mm projectile at a depth of 86 cm, before (left) and after (right) the filtering process in JD. The lower SNR means that only two eigenvalues are above the noise level.

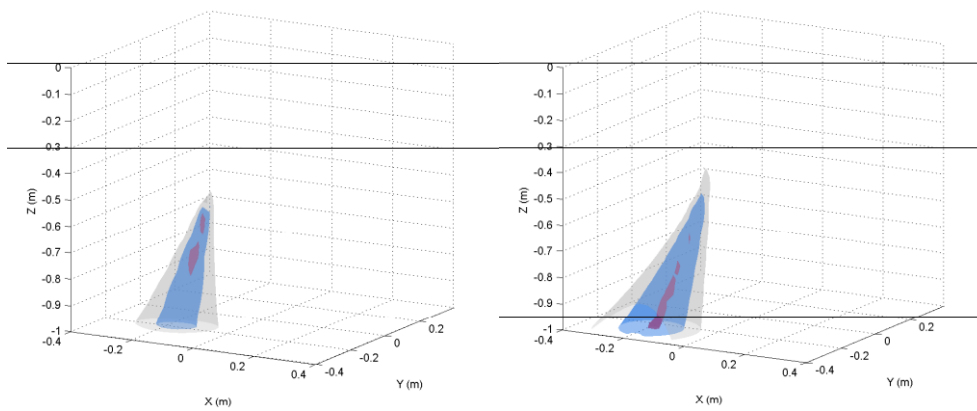


Figure 20. Target location found in MUSIC algorithm for the 86 cm depth case before (left) and after (right) the filtering, gray, blue and red shows the contour surface of 60%, 75% and 90% of the maximum value, respectively.

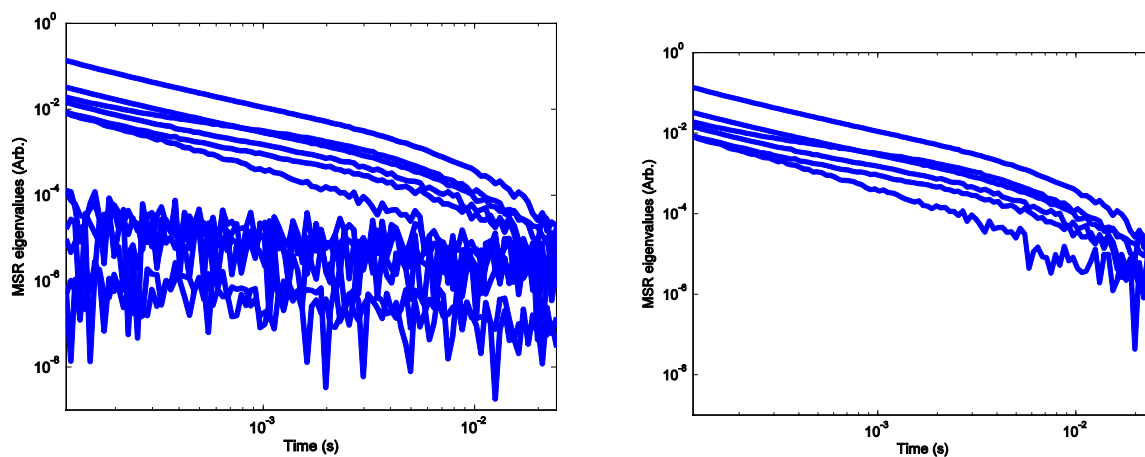


Figure 21. Eigenvalues for the SR-2059, a 37-mm projectile at a depth of 17.5 cm, before (left) and after (right) the filtering process in JD.

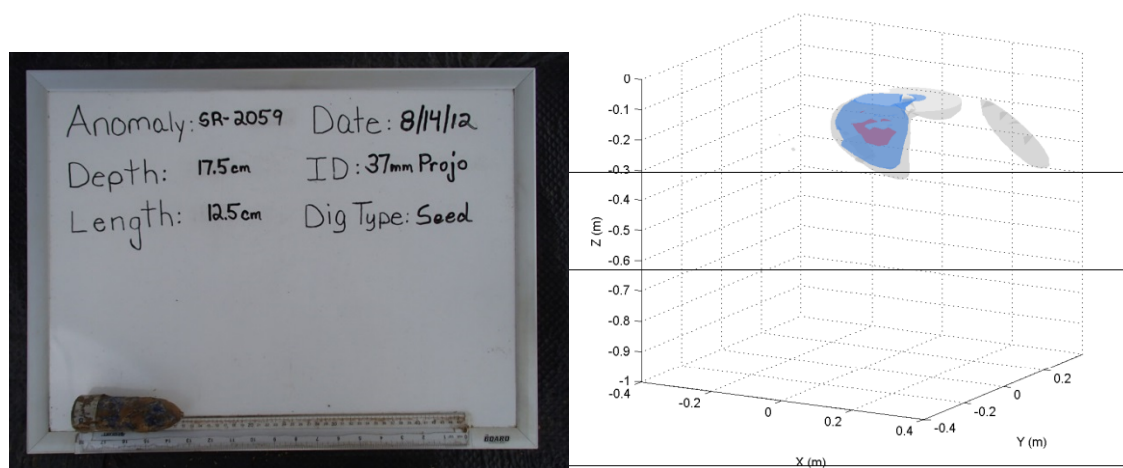


Figure 22. Ground truth photo and MUSIC result for SR-2059 at Spencer Range. Gray, blue, and red show the contour surface of 60%, 75%, and 90% of the maximum value, respectively.

## The JD algorithm for guiding data collection in real time

This section presents an analysis of numerical and experimental data involving small and/or deep targets. The data were collected by NOVA and SAIC personnel using TEMTADS. The detection depth of TEMTADS and other EMI sensors is limited by the Tx moment, a quantity directly proportional to the magnitude of the transmitter currents and the area of the Tx coils. In this section we demonstrate the applicability of JD to guide data collection in real time, combine and investigate different Tx signals to improve classification of small targets, and finally use JD to choose optimal Tx/Rx configurations.

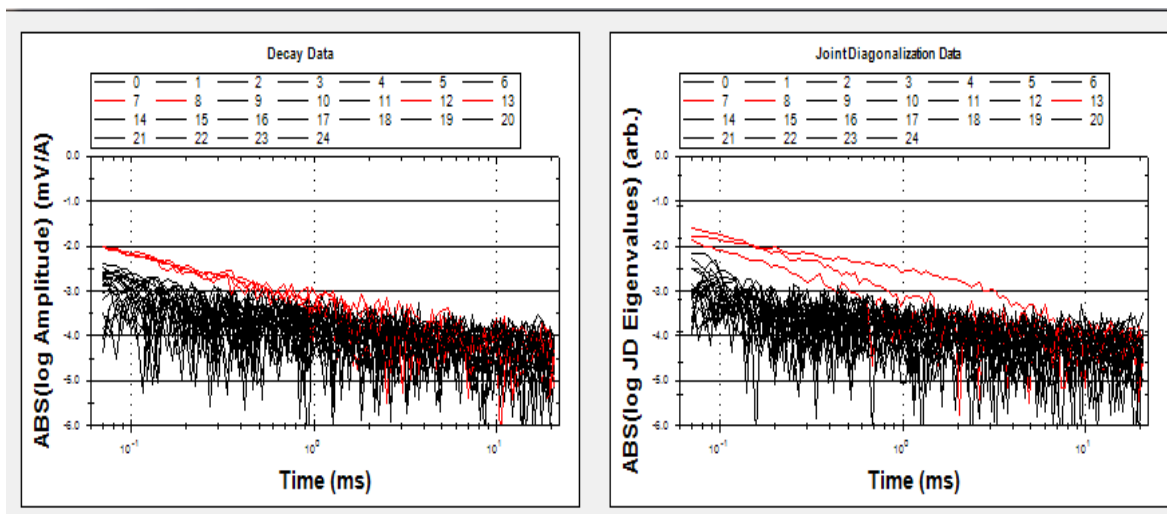


Figure 23. Left: Measured  $5 \times 5$  TEMTADS monostatic signal versus time for a 37-mm projectile placed 60 cm below the sensor center. Right: MSR matrix eigenvalues versus time extracted via JD from the same 37-mm projectile dataset.

The current practice for TEMTADS cued-data collection is as follows: (a) first, survey data are collected using the cart-based EM61 system; (b) the EM61 survey data collection team creates a detection anomaly list and gives it to the TEMTADS cued-data collection team; (c) the TEMTADS team uses the EM61 detection anomaly list as a guide as it collects cued EMI data; (d) the TEMTADS team drives the sensor at the anomaly position and collects data. For data quality control the team takes all  $25 \text{ Tx} \times 25 \text{ Rx}$  data and creates a monostatic set that uses only the collocated Tx/Rx. For example, the left panel of Figure 23 shows the measured monostatic data vs. time for a 37-mm projectile placed at a depth of 60 cm. The red lines are measured

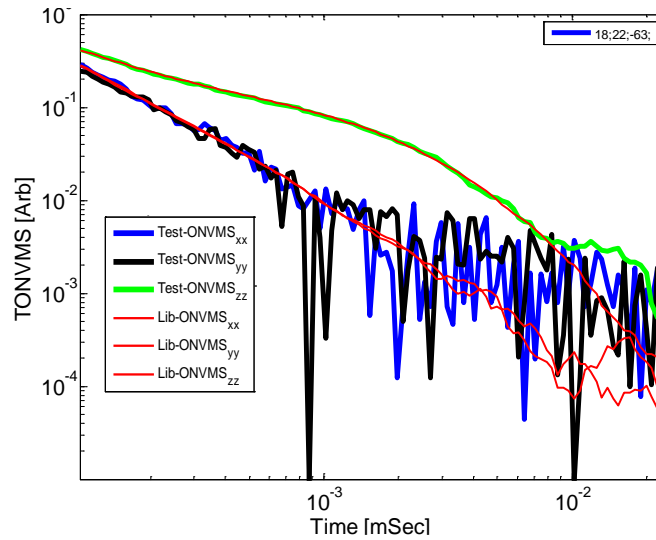


Figure 24. Inverted total ONVMS for a 37-mm projectile placed 60 cm below the  $5 \times 5$  TEMTADS center.

signals above the threshold (in this case  $10^{-2.5}$  at the fifth time channel). From this result it is difficult to conclude that there is a target, and furthermore it is impossible to say that it is a 37-mm-like target. Using the same data set we constructed the MSR matrix and extracted the time-dependent eigenvalues, which are depicted on the right panel of Figure 23. Using the same threshold level, we see a good separation between signal (red) and noise (black) eigenvalues. Studies have shown that the time-decay patterns of eigenvalues are related directly to the target's effective principal magnetic polarizabilities [3], [8], [9], [41]. The comparison between time-decay patterns of eigenvalues (red) on the right panel of Figure 23 and the time-decay pattern of the primary polarizability ( $\text{TONVMS}_{zz}$ ) of the 37-mm library target (Figure 24) clearly shows that the eigenvalues above the noise level correspond to a 37-mm-like target. Thus, we see that the JD technique can be used to guide the data-collection team. Note that JD provides information about potential targets and that the eigenvalues depend on the sensor-target distance. To demonstrate the classification performance for the 37-mm UXO buried at a depth of 60 cm we inverted data using the ONVMS technique. The extracted total ONVMS is depicted on Figure 24. The inverted total ONVMS matches well the primary total ONVMS (red) of the 37-mm projectile from the library. To determine the limitations of the technique we placed the target 90 cm below the sensor. We applied both JD and ONVMS to the data, obtaining the results shown in Figure 25. The MSR analysis shows that the response from the target is indistinguishable from the noise, which means that in this case it is difficult to extract reliable

classification parameters from the data. We investigated the same data using ONVMS. From Figure 25 (right) it can be seen that the inverted classification features are not close to the total ONVMS of the expected 37-mm projectile.

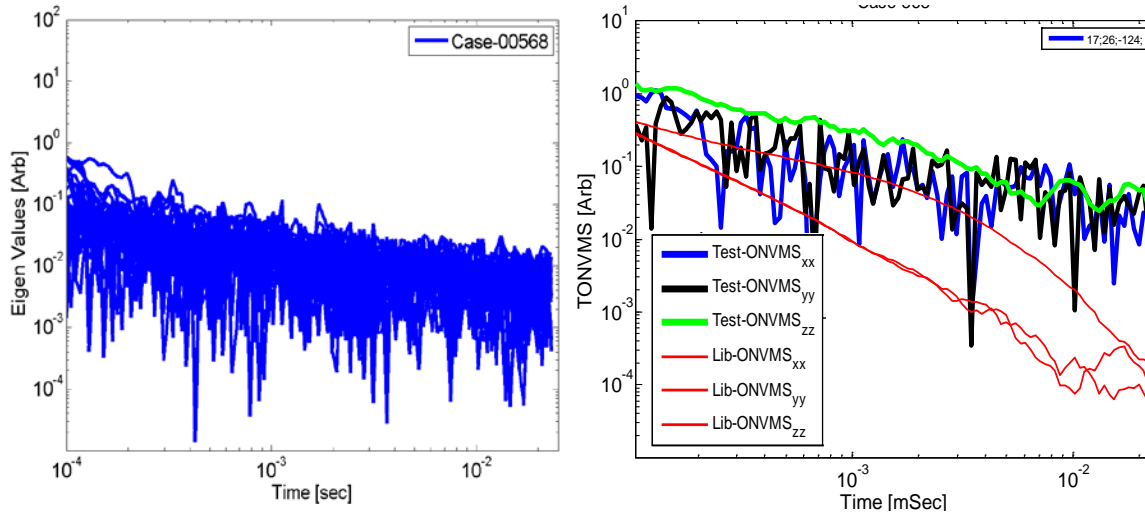


Figure 25. A vertical 37-mm projectile placed 90 cm below the center of the  $5 \times 5$  TEMTADS sensor. Left: MSR data matrix eigenvalues. Right: inverted total ONVMS.

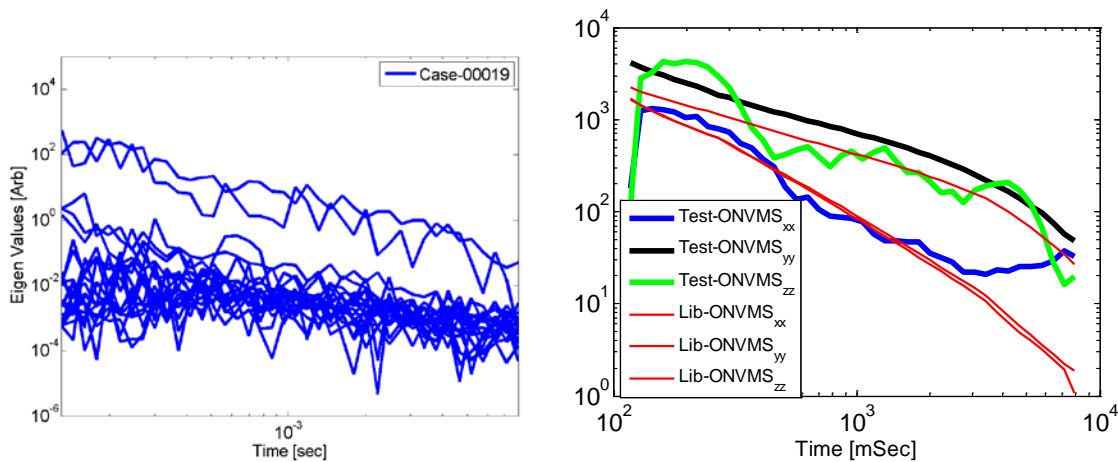


Figure 26. A vertical 37-mm projectile placed 90 cm below the center of the MetalMapper sensor. Left: MSR data matrix eigenvalues. Right: inverted total ONVMS.

## **Improving the capability of current advanced EMI sensors to detect and discriminate small and deep targets**

EMI sensing is based on the near magnetic field. As a result, target responses decay very rapidly (as  $\sim 1/\text{distance}^6$ ), which poses a significant challenge for current advanced EMI sensors as they attempt to detect and classify small and/or deep targets. There are two ways to improve detection depth: increasing the amplitude of the transmitter (Tx) current, or increasing the area of the Tx coils. Since a sensor's noise floor depends linearly on the Tx currents, it is more practical to increase the size of the Tx coils. To demonstrate the applicability of a large Tx loop for detecting deep and small targets, we consider data collected for the 37-mm projectile using the MetalMapper sensor. The MetalMapper is an advanced, commercially available EMI system [2] that has three orthogonal  $1\text{ m} \times 1\text{ m}$  square Tx loops. The 37-mm projectile was placed 90 cm below the instrument. The resulting time-dependent MSR eigenvalues are depicted in Figure 26. The result shows that the target's eigenvalues are above the threshold. The data were inverted using the ONVMS technique; the estimated total ONVMS is shown on Figure 26 at right. The result illustrates that the extracted  $\text{TONVMS}_{xx}$  and  $\text{TONVMS}_{zz}$  are noisier than  $\text{TONVMS}_{yy}$ . We can also see that  $\text{TONVMS}_{yy}$  follows to the expected library total  $\text{TONVMS}_{zz}$ . Thus, the data are insufficient to extract the target polarizabilities and orientation reliably. However we see that increasing the Tx loop size can improve the capability to detect and classify small targets, since at least one extracted polarizability can be used for classification.

One of simplest ways to improve target detection depth is to use an existing system and stack the transmitter responses numerically. To understand this, we investigate the detection and classification ability of the  $5 \times 5$  TEMTADS for a deep 105 HEAT-round UXO. The data were collected at the Aberdeen Proving Ground. The target was buried horizontally at 115 cm below the surface. We considered two cases: 1) using all data and 2) combining the signals of Tx loops by row and column (see Figure 27). The data were inverted using ONVMS. The results, shown on Figure 27 at right, illustrate that combining Tx signals produces slightly better classification features than using data from all  $25 \times 25$  Tx/Rx combinations.

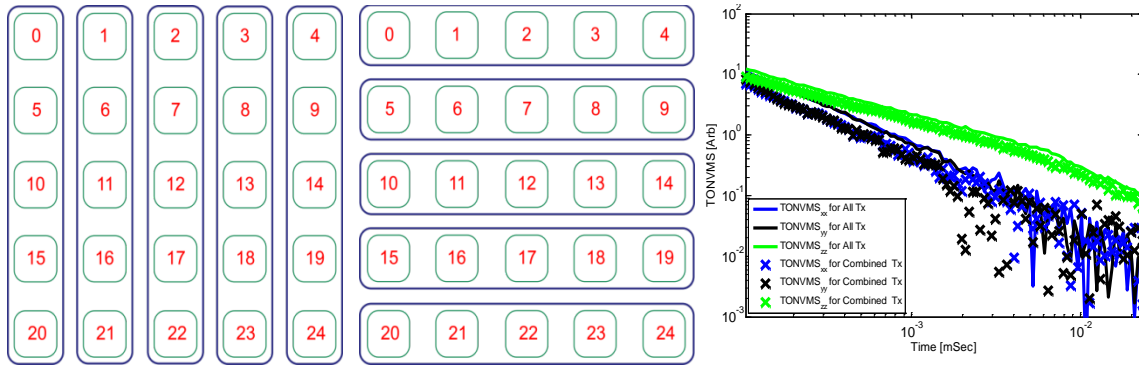


Figure 27. (Left) Combining TEMTADS Tx loops column-wise and row-wise. (Right) Extracted total ONVMS for the 105 HEAT-round buried horizontally at 115 cm depth: original  $5 \times 5$  TEMTADS (solid lines) and combined Tx (crosses).

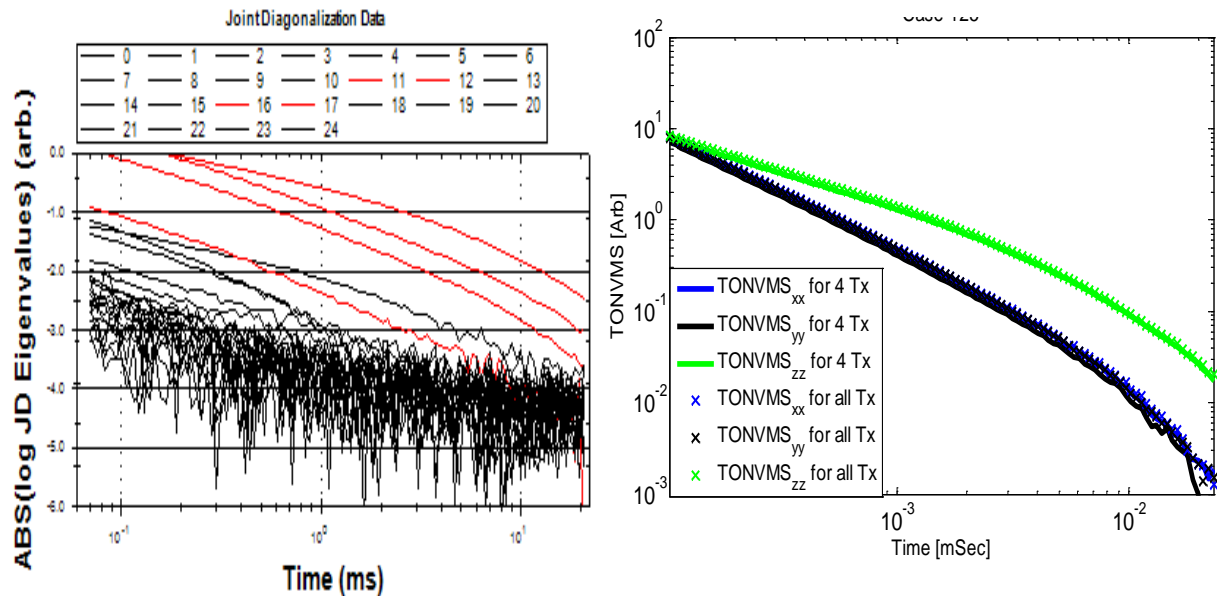


Figure 28. Left:  $5 \times 5$  TEMTADS MSR eigenvalues for a 105-mm HEAT round buried at a depth of 35 cm. Right: Extracted total ONVMS using all Tx/Rx pairs (solid lines) and using only 4 Tx and all 25 Rx combinations (crosses). The data were collected at the APG blind grid.

Finally, we used the JD technique to determine an optimal Tx/Rx configuration to estimate classification feature parameters. The studies were done for a 105-mm HEAT round buried at depths 35 cm and 115 cm. The data were collected at the APG blind grid using the  $5 \times 5$  TEMTADS. First, the original complete set of  $25 \text{ Tx} \times 25 \text{ Rx}$  pairs were used and the total ONVMS was extracted. Then the JD technique was used and the above-threshold eigenvalues were determined. The time-dependent eigenvalues are shown on Figure 28 (left) for the 105-mm

projectile buried at the shallower depth of 35 cm. The eigenvalues above the threshold and their corresponding Tx are highlighted in red. Finally, the total ONVMS were extracted from data belonging to four Tx (#11, #12, #16, and #17; refer to Figure 28 on left) and all 25 Rx. The inverted total ONVMS are shown on Figure 28 (right). The solid lines correspond to the total ONVMS extracted from the original data ( $25 \text{ Tx} \times 25 \text{ Rx}$ ), and crosses to the optimal data for the  $4 \text{ Tx} \times 25 \text{ Rx}$  configuration. The results are identical, which clearly indicates that there is an optimal Tx/Rx configuration. The optimal data provide as good classification parameters as all Tx/Rx pairs. The same results were observed for the deep target (but are not shown here). This information is important during data collection because it can help improve SNR by lowering the sensor if applicable, or use only the optimal number of Tx and collect data for longer.

### **Understanding noise in an EMI system**

Advanced EMI systems have been developed and demonstrated under SERDP-ESTCP programs [1], [2], [5], [6], [7]. One such sensor is the Time-Domain Electromagnetic Towed Array System (TEMTADS). In its current configuration, the instrument consists of 25 transmit/receive pairs of square coil antennas arranged in a  $5 \times 5$  grid. The sensor activates the transmitter loops one at a time, and for each transmitter all receivers measure the complete transient response over a wide dynamic range of time. Thus, in cued interrogation mode the sensor provides a total of 625 high-fidelity data points data at each instrument location. The detection depth of TEMTADS and other EMI sensors is limited by the Tx moment, a quantity directly proportional to the transmitter current and the area of the Tx coils.

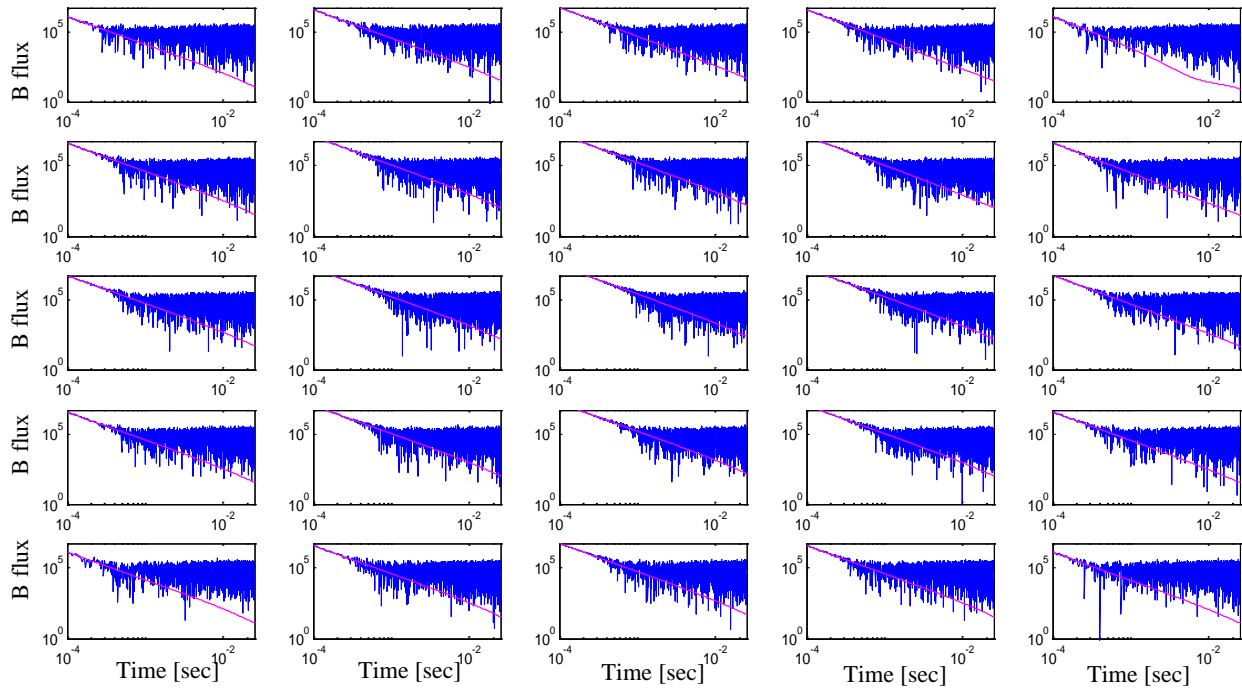


Figure 29. EMI response versus time for a heterogeneous target placed 1.2 m below a  $35 \text{ cm} \times 35 \text{ cm}$  Tx loop. Magenta lines correspond the target's responses at  $5 \times 5$  Rx positions, while blue lines are for target responses plus noise.

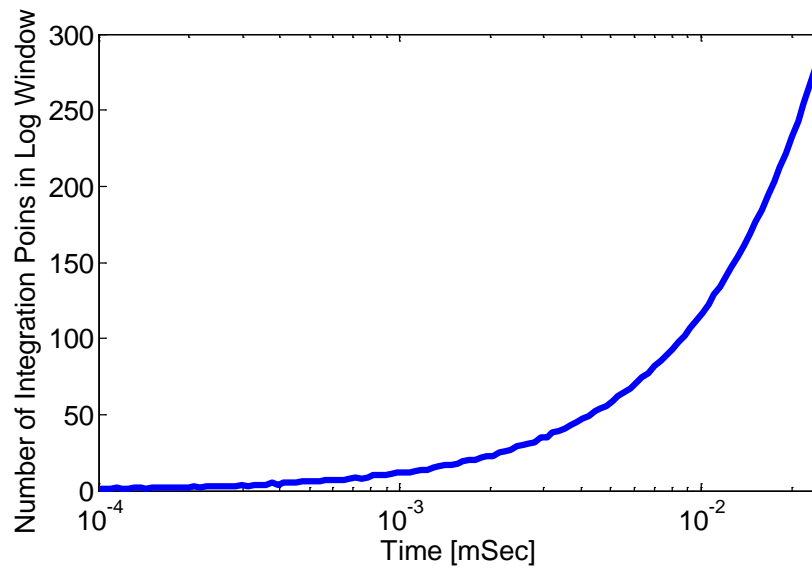


Figure 30. Number on data points in each logarithmic interval.

The subsurface target responses also depend linearly on the Tx currents. The system collects data in a linear scale at 4  $\mu$ s time steps from 100  $\mu$ s to 25ms. To understand the system's noise distribution, we modeled EMI responses from a heterogeneous target consisting of three different permeable and conducting sections. The target was placed at 1.2 m below the system and illuminated with 35 cm  $\times$  35 cm horizontal Tx coils. Calculations were done for two cases: 1) no noise added (see magenta lines on Figure 29); and 2) the same level of random noise added to the signals at each receiver (see blue lines on Figure 29). The results show that the target signals are masked entirely by noise at late times. Thus, the target detection and classification is difficult, and even impossible, in the presence of noise. We would like to improve the signal-to-noise ratio at late times. Current systems first take the logarithm of time, divide it into equal intervals, and then integrate the data in each logarithmic interval. The number of data points inside each log window is nonlinear (Figure 30). The distribution illustrates that at later times the number of data points increases nonlinearly. The integrated signal is depicted on Figure 31 in green. The result shows that the integration improves the signal-to-noise ratio at late times, but the data quality is still not good enough for data inversion and classification. These studies prompted us to reduce the number of time gates (or equal logarithmic intervals) from 121 to 24 time channels for further data quality improvement (Figure 32).

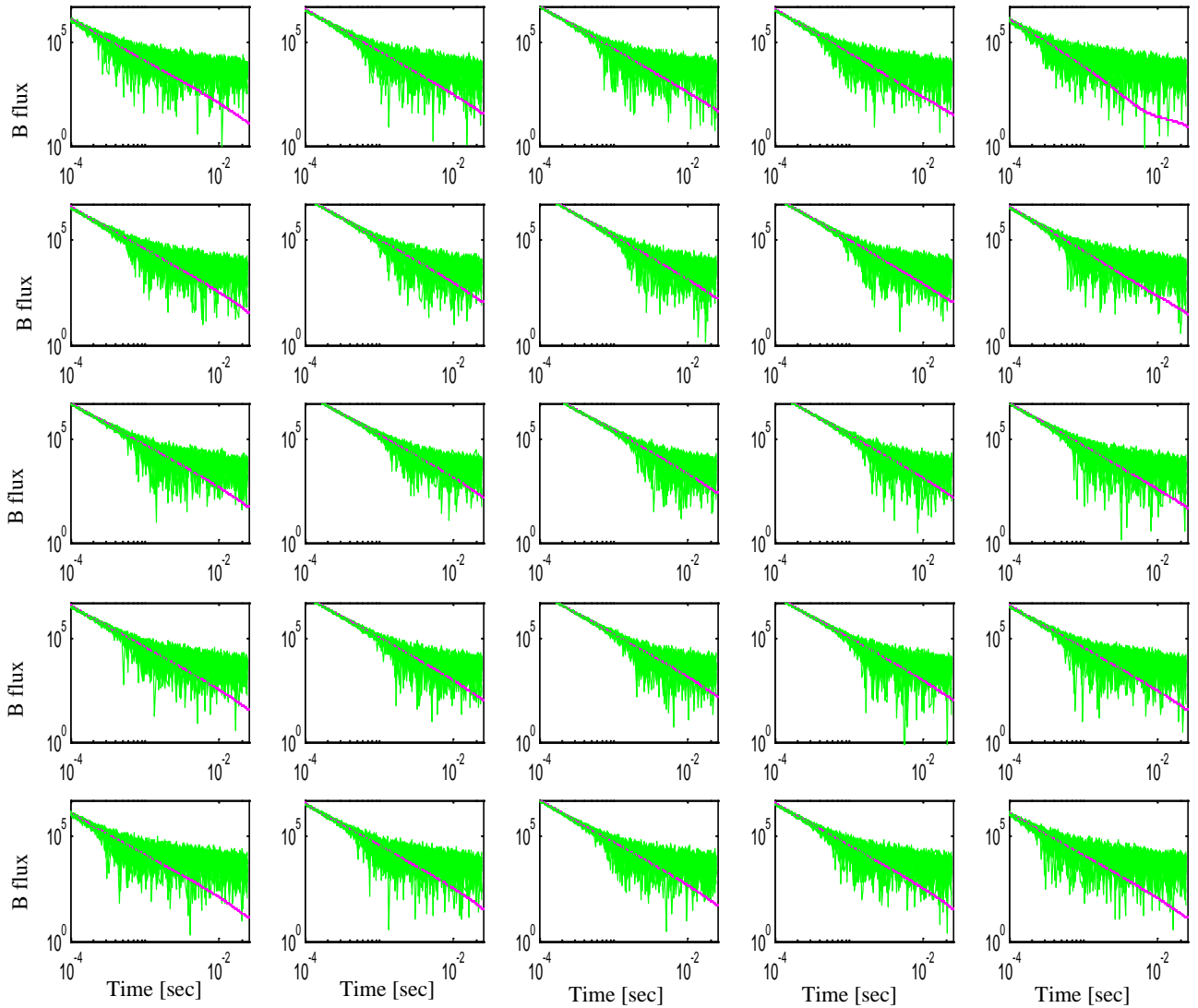


Figure 31. EMI response vs. time at 121 equally spaced logarithmic intervals for a heterogeneous target placed 1.2 m below a  $35 \text{ cm} \times 35 \text{ cm}$  transmitter coil. Magenta lines correspond to the target's responses at  $5 \times 5$  receiver positions; green lines are for target responses plus noise. The data are integrated at each logarithmic interval.

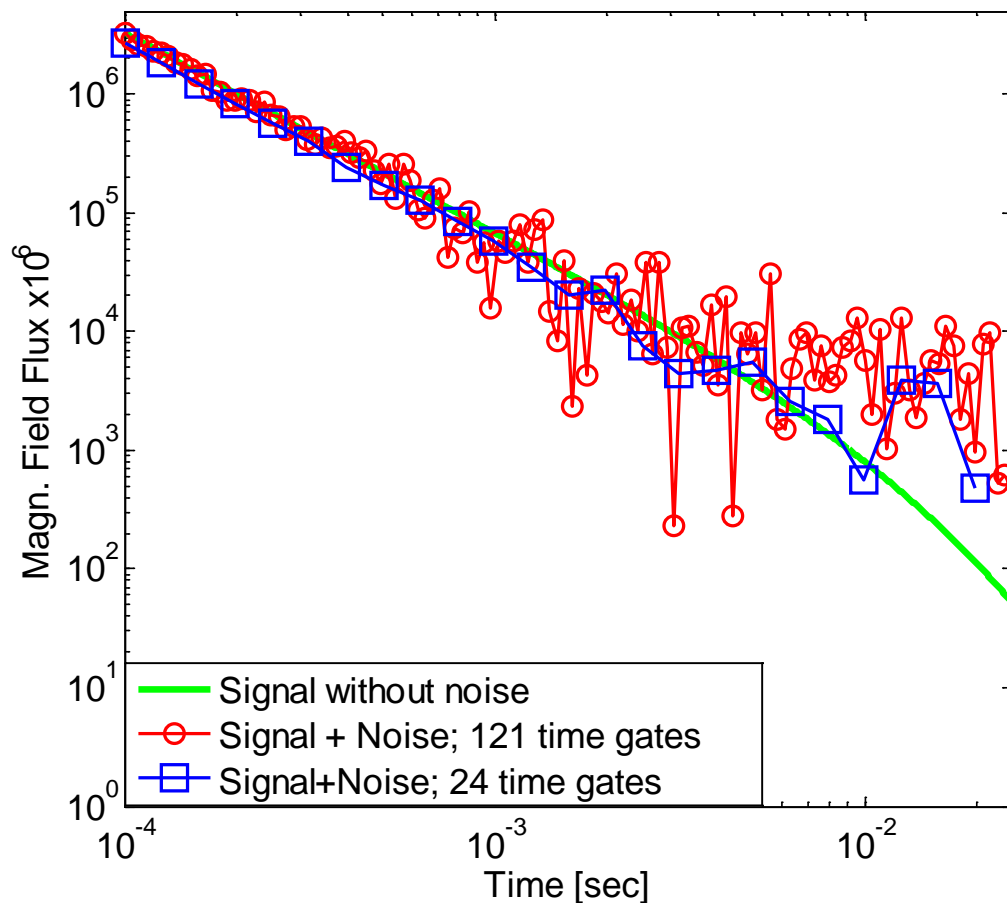


Figure 32. Comparisons between magnetic fields for a heterogeneous target with noise (blue and red lines) and without noise (green line). First, data were calculated at every 4  $\mu$ s in a linear scale and then reduced to time gates with equal logarithmic intervals. Comparing between 24 (blue lines) and 121 (red lines) timegates shows that reducing the timegate number improves the data quality at times later than 1 ms.

### **Tx-combination/high-current effect**

In order to improve SNR further, we investigated how Tx coil combinations and size affect target EMI responses. Data from the previously mentioned heterogeneous target were simulated for three cases: 1) two Tx coils with 1 A Tx currents acting simultaneously, plus noise; 2) one Tx coil with 2 A Tx current plus noise; and 3) one Tx coil with 2 A current without noise. The comparisons between the three different cases are depicted on Figure 33. There is no significant

improvement in the data quality between using two Tx coils with 1 A currents simultaneously or using one Tx coil with 2 A. Splitting the current evenly between the two Tx coils is a challenge for background subtraction, data normalization, and classification. It is thus preferable to use one Tx with twice the current for live-site UXO detection and classification.

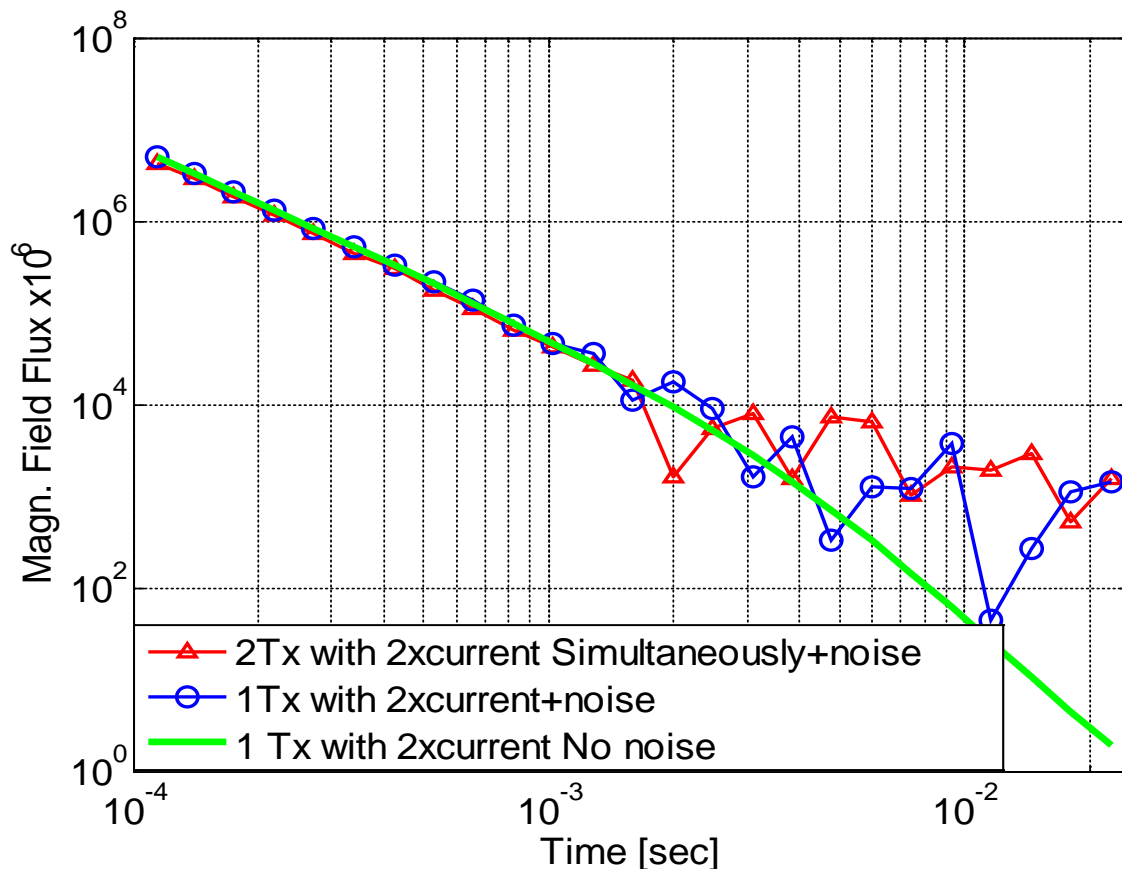


Figure 33. EMI signal versus time for a heterogeneous target.

### Large Tx currents: experimental validation

To validate the theoretical studies, we conducted actual experiments using the  $2 \times 2$  TEMTADS system [5]. The system has a  $2 \times 2$  grid of Tx coils (which are activated sequentially) and four vector Rx. The data were collected on a test stand with a 37-mm projectile, placed below the system at a depth of 86 cm, as target.



Figure 34. An experimental setup for the  $2 \times 2$  3D system with large Tx currents.

Three cases were considered: 1) using the existing system hardware, which has a current of 6 A, or 2-3) using hardware updates that produce Tx currents of either 11 A or 14 A. In all cases the data were analyzed using the joint diagonalization [9] and ONVMS techniques [8]. The time-dependent JD eigenvalues and inverted total ONVMS effective polarizabilities are shown in Figure 35 using the standard system with a 6 A Tx current. In this case, the results show that the eigenvalues are very close to the noise level; however, one of the eigenvalue time-decay profiles matches the effective polarizability time-decay curves of 37-mm projectiles, clearly indicating that one such target is present. However, due to low SNR, the inverted effective polarizabilities

are noisy and do not match well with the expected total ONVMS polarizability decay curves. It is therefore difficult, even impossible, to classify this target as a 37-mm projectile.

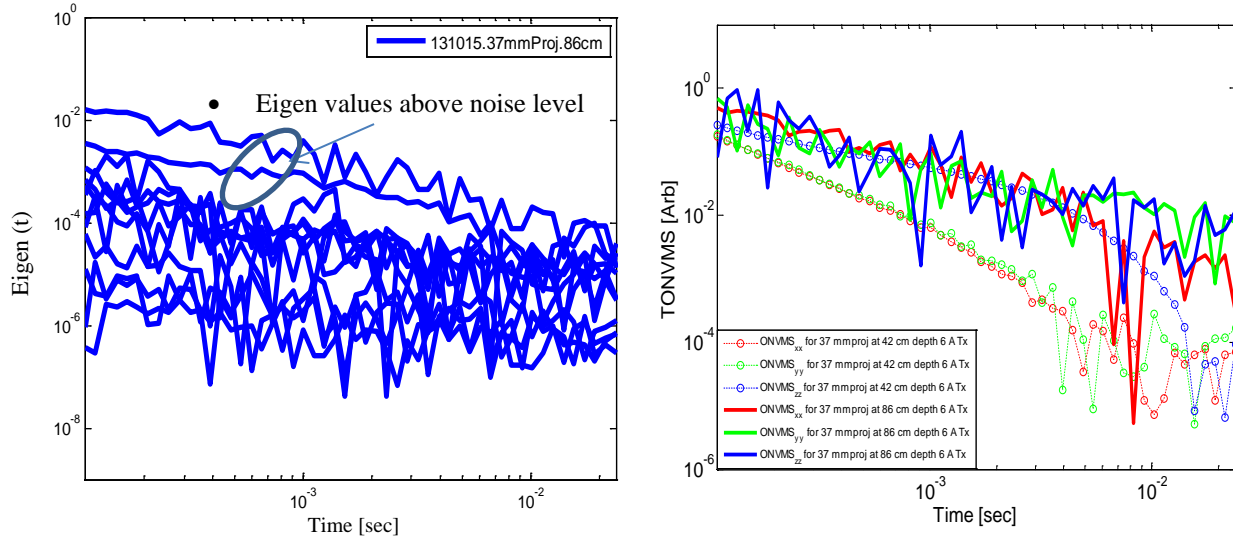


Figure 35. Transmitter coil with a 6 A current. Left: time-dependent eigenvalues for a 37-mm projectile placed below the system at a depth of 86 cm. Right: extracted total ONVMS for the 37-mm projectile buried at depths of 42 cm (dashed circle lines) and 86 cm (solid lines).

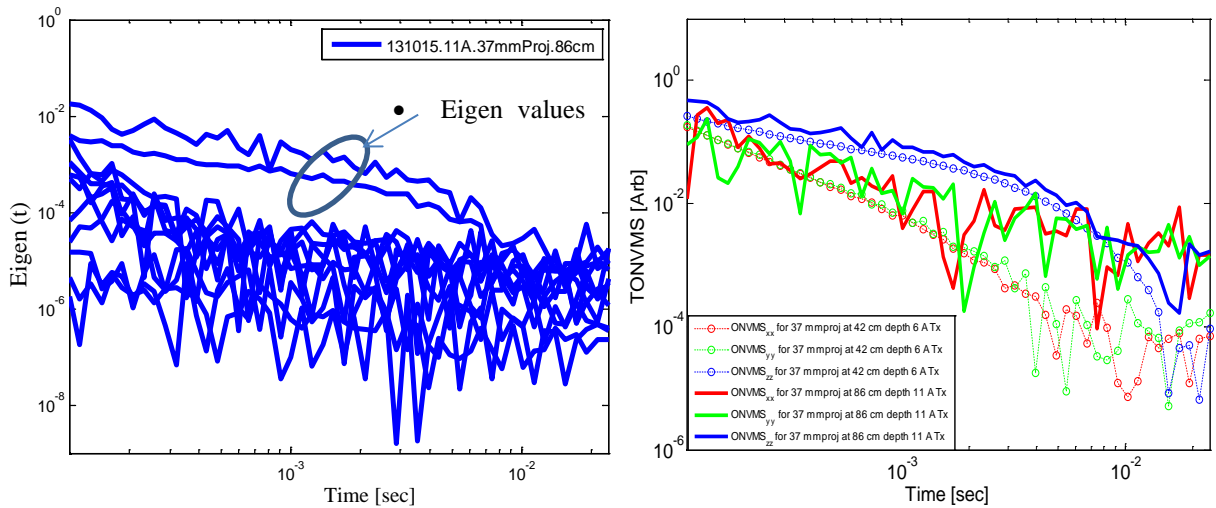


Figure 36. Transmitter coil with an 11 A current. Left: time-dependent eigenvalues for a 37-mm projectile placed below the system at a depth of 86 cm. Right: extracted total ONVMS for the 37-mm projectile buried at depths of 42 cm (dashed circle lines) and 86 cm (solid lines).

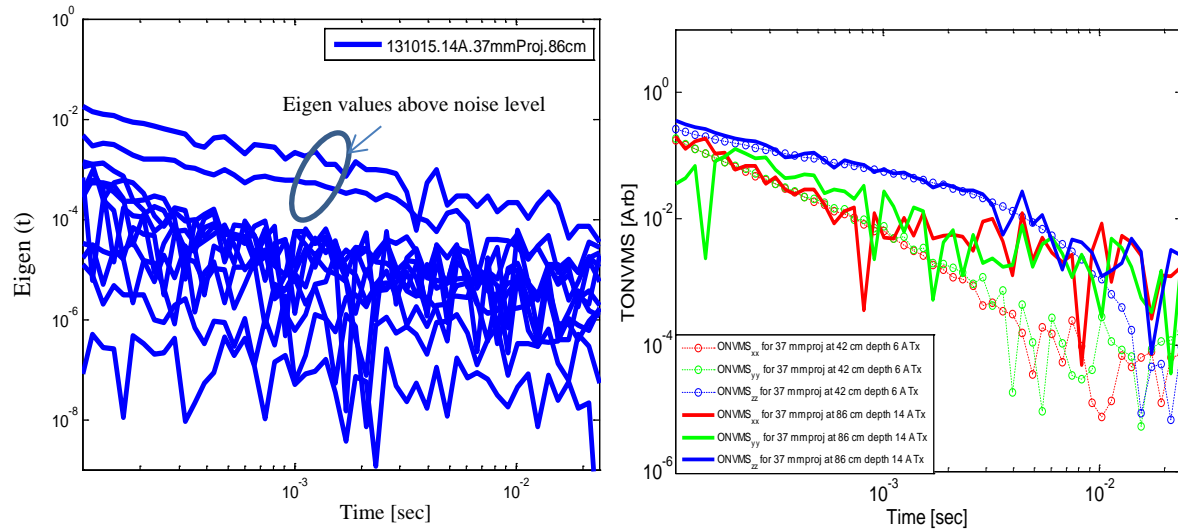


Figure 37. Transmitter coil with a 14 A current. Left: time-dependent eigenvalues for a 37-mm projectile placed below the system at a depth of 86 cm. Right: extracted total ONVMS for the 37-mm projectile buried at depths of 42 cm (dashed circle lines) and 86 cm (solid lines).

Next, we modified our hardware system and increased the transmitter current from 6 A to 11 A and then to 14 A. The results are depicted on Figure 36 and Figure 37. These results show that, as the Tx current magnitudes increase, there is a clear separation between target eigenvalues and noise eigenvalues. As a result of the large current employed, the extracted total ONVMS are less noisy and match the expected total ONVMS time decays. Thus, not only does the system detect deep targets, but also provides classification capabilities.

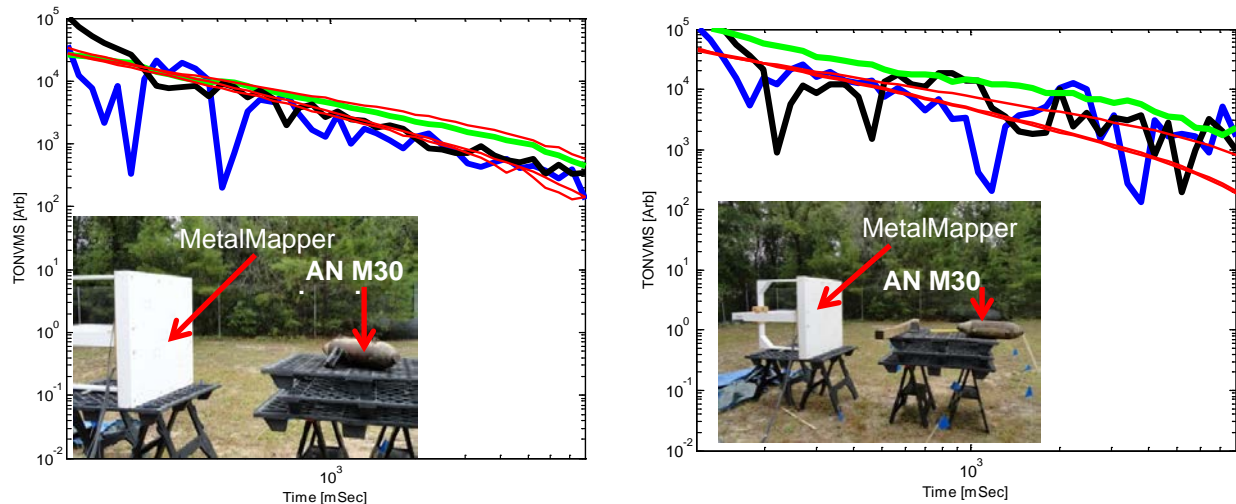


Figure 38. Inverted effective ONVMS for an M30 Bomb in a test-stand scenario. The target is oriented 45 degrees at a depth of 150 cm depth (top) and oriented vertically at a depth of 210 cm (bottom). The red lines are the total ONVMS for a library AN M30 Bomb, and the other lines correspond to the effective primary (green), secondary (black), and tertiary (blue) effective polarizabilities for the test AN M30 target.

### ONVMS for deep target classification

The ONVMS technique, readily applicable to both single- and multi-object data, is next applied to deep target detection and classification at the West Mesa site. One of the potential targets of interest is the AN M30 Bomb, which is ~36 inches in length and 11 inches in diameter, and weighs 100 pounds. These bombs are found at different depths and orientations ranging anywhere from the surface to depths of two meters. Thus, one of the challenging problems for this site is to detect and reliably discriminate low-signal-to-noise targets. The task here is to classify deeply buried AN M30 bombs accurately. In an effort to understand the complexities involved in this detection and discrimination process, personnel from the Environmental and Munitions Center of Expertise at the U.S. Army Corps of Engineers collected test-stand data using the MetalMapper. We took these data sets and inverted for target classification parameters, which are shown in Figure 38. The extracted polarizabilities match very well with the expected library parameters for such a target placed at 150 cm from the sensor. The extracted primary effective polarizability (green) for AN M30 bomb 210 cm away from the sensor shows the same

trend as the expected library targets primary polarizability. This result indicates that at least the primary effective polarizability can be extracted accurately for both shallow and deep targets. The ONVMS technique is thus able to classify deep and challenging targets.

## 5 Modeling advanced EMI sensors: searching for optimal Tx/Rx combinations and configurations

### Introduction

Recently, a wide-range of different electromagnetic induction sensing technologies with novel waveforms, multi-axis transmitters, and scalar/vector receivers were developed under SERDP-ESTCP programs. The advanced EMI sensors, which include the MetalMapper, TEMTADS, the Berkeley UXO Discriminator (BUD), the Man-Portable Vector Time-Domain (MPV-TD) sensor, and the Portable Decoupled Electromagnetic Induction Sensor (PEDEMIS), provide a combination of measurement spatial diversity, full vector definition of signals from a variety of viewpoints, and an extremely wide time range. These current state-of-the-art EMI systems offer unprecedented data quality for discrimination-processing algorithms. This chapter studies how to take advantage of this data diversity and further enhance the detection and discrimination abilities of these advanced EMI systems in order to achieve multi-angle illumination of deep targets. We consider different Tx/Rx combinations and configurations, review modeling approaches for transmitted and received EMI fields, and present comparisons between actual and de-noised data. We first describe the high-power  $2 \times 2$  TEMTADS, then analyze the different Tx combinations that we considered, and finally present results of classification studies performed on APG blind and small-munition test-site data.

### The high-power $2 \times 2$ TEMTADS

The high-power  $2 \times 2$  TEMTADS, also known as the mini-MetalMapper, is an updated version of the standard NRL TEMTADS  $2 \times 2$  system developed with the intended purpose of improving the detection and classification of small and/or deep UXO. The standard NRL TEMTADS  $2 \times 2$  system, an advanced EMI instrument for UXO detection and discrimination, was developed in its initial stages primarily by the NRL, NOVA, Inc., and G&G Sciences. Recently, the system's transmitter electronics were updated to produce higher Tx currents. (That work was carried out as part of the present SERDP project, MR-2225, whose lead organization is Dartmouth College. Another state-of-the-art instrument, a commercially available version of the  $2 \times 2$  TEMTADS called the Geometrics mini MetalMapper, also has high-power transmitters.) The high-power  $2 \times 2$  TEMTADS has a Tx array with four coplanar square coils, each of which has a triaxial Rx

placed at its center. Each Rx cube contains three orthogonal coils and thus registers all three vector components of the impinging signals. The Tx coils illuminate buried targets using currents higher than 10 A; when the excitation pulse is turned off, the Rx collect target responses at a sample rate of 500 kHz. Figure 39 and Figure 40 respectively show a schematic diagram of the NRL  $2 \times 2$  TEMTADS and a photograph of the actual hardware. The system operates in both static (cued) and dynamic modes. For dynamic mode, the raw decay measurements are grouped into 19 logarithmically spaced time gates whose center times range from 25  $\mu$ s to 2.77 ms with 20% widths. For cued mode, the raw decay measurements are grouped into 121 logarithmically spaced time gates whose center times range from 25  $\mu$ s to 24.35 ms with 5% widths. The sensor is placed on a cart that provides a sensor-to-ground offset of 20 cm or less. The updated NRL TEMTADS  $2 \times 2$  system is straightforward to operate. In survey mode, the system collects a series of closely spaced parallel lines of survey data whose processing results in a list of detected target positions to be interrogated in cued mode. Each target position is flagged with a non-metallic pin flag using centimeter-level GPS. The sensor is positioned over each target in turn. At each target position, the system's Tx coils are activated sequentially while all four Rx record data. The complete set of data for each target is then inverted to extract target characteristics and classification features.

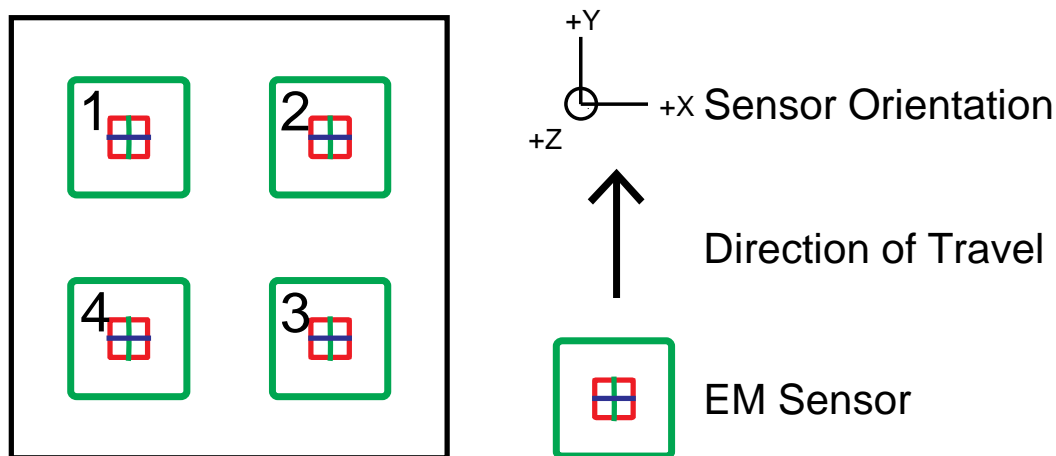


Figure 39. Schematic diagram of the NRL TEMTADS  $2 \times 2$  EMI sensor array. Each unit consists of a  $35 \times 35$  cm Tx loop with an 8 cm triaxial Rx cube at its center. The complete system is  $0.8 \times 0.8$  m in size.



Figure 40. The NRL TEMTADS  $2 \times 2$  system (a) on its cart and (b) with its weather shield removed.

The TEMTADS transmitters are modeled as infinitesimally thin rectangular wires. The complete primary field produced at any observation point  $\mathbf{r}$  by the  $T$ th loop is determined from the Biot-Savart law,

$$\mathbf{B}_T(\mathbf{r}) = N_{turns} \frac{\mu_0}{4\pi} \sum_{i=1}^{N_{Tx}} \frac{I_T [\Delta \ell_{T,i} \times \mathbf{R}_{T,i}]}{R_{T,i}^3}, \quad T=1,2,3,4, \quad (35)$$

where, for the  $T$ th transmitter loop,  $\mathbf{R}_{T,i} = |\mathbf{r} - \mathbf{r}'_{T,i}|$ ,  $\mathbf{r}'_{T,i}$  is the location of the  $i$ th current element, and  $\Delta \ell_{T,i}$  is the tangential length vector for the  $i$ th subsection of the loop (see Figure 41). In all subsequent analysis, unless otherwise noted, each transmitter coil ( $T=1,2,3,4$ ) was divided into  $N_{Tx} = 40$  subsections and the primary magnetic field  $\mathbf{B}_T(\mathbf{r})$  was calculated using equation (35).

Each of TEMTADS's four cube Rx measures the induced voltage along three orthogonal directions. The induced voltage is the negative of the time derivative of the secondary magnetic flux through each coil. The induced voltage on the  $R$ th cube ( $R=1,2,3,4$ ) along the  $\alpha$ th direction ( $\alpha = z, y, x$ ) is calculated as

$$V_R^\alpha = - \int_{S_R^\alpha} \frac{\partial \mathbf{B}}{\partial t} \cdot d\mathbf{s}_R^\alpha = \sum_{i=1}^{N_{Rx}} \frac{\partial \mathbf{B}_i(\mathbf{r}_{i,R} - \mathbf{r})}{\partial t} \cdot \hat{\mathbf{n}}_\alpha \Delta s_{i,R}^\alpha \quad (36)$$

where  $s_R^\alpha$  is the area of the receiver in the  $\alpha$ th direction of the  $R$ th Rx cube (which is  $8 \times 8 \text{ cm}^2$  for the  $2 \times 2$  TEMTADS),  $\Delta s_{i,R}^\alpha$  and  $\mathbf{r}_{i,R}$  are respectively the  $i$ th sub-area and observation point

on the surface  $s_R^\alpha$ , and  $\hat{\mathbf{n}}_\alpha$  is normal to  $s_R^\alpha$ .  $\mathbf{B}(\mathbf{r}_{i,R}^\alpha) = \mu_o \mathbf{H}(\mathbf{r}_{i,R}^\alpha)$  is the magnetic field produced by a magnetic dipole/charge source placed at point  $\mathbf{r}$ ; see Figure 42.

Transmitter coils

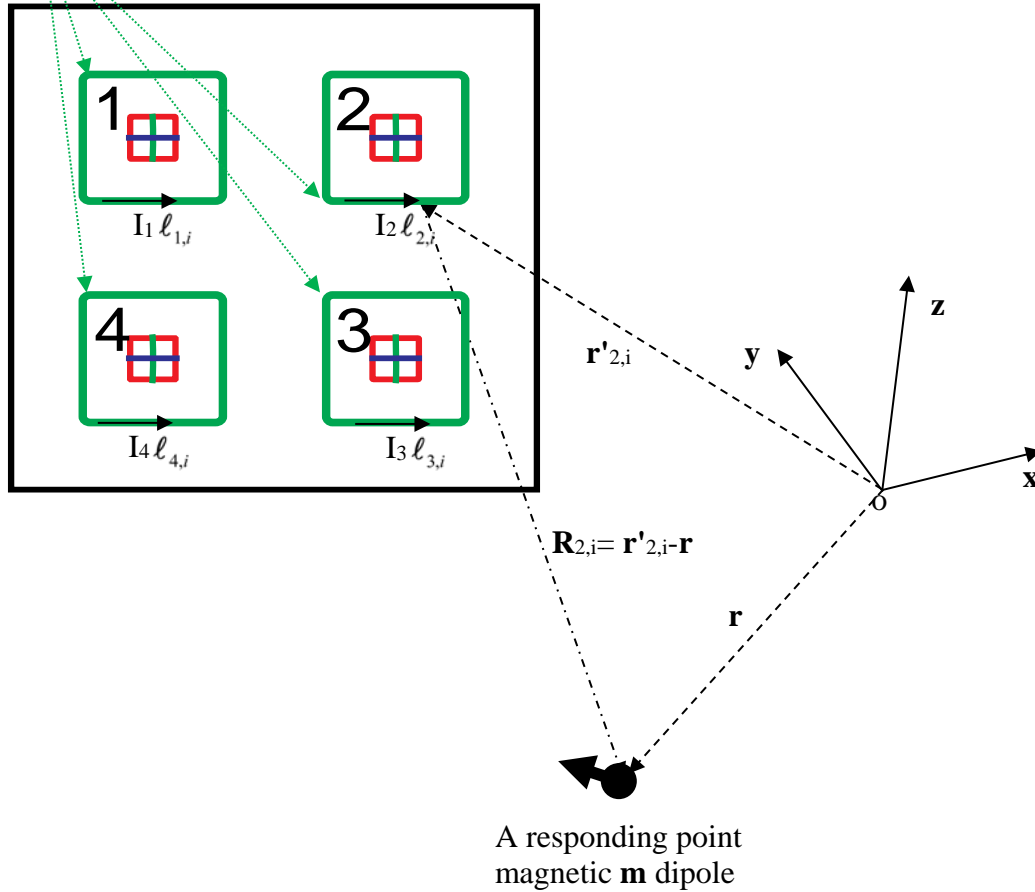


Figure 41. The  $2 \times 2$  TEMTADS geometry. XYZO is a global Cartesian coordinate system,  $\mathbf{r}$  is an observation point measured with respect to XYZO, and  $\mathbf{r}'_{2,i}$  is the  $i$ th current element on the  $T = 2$  transmitter with respect to the global coordinate system.

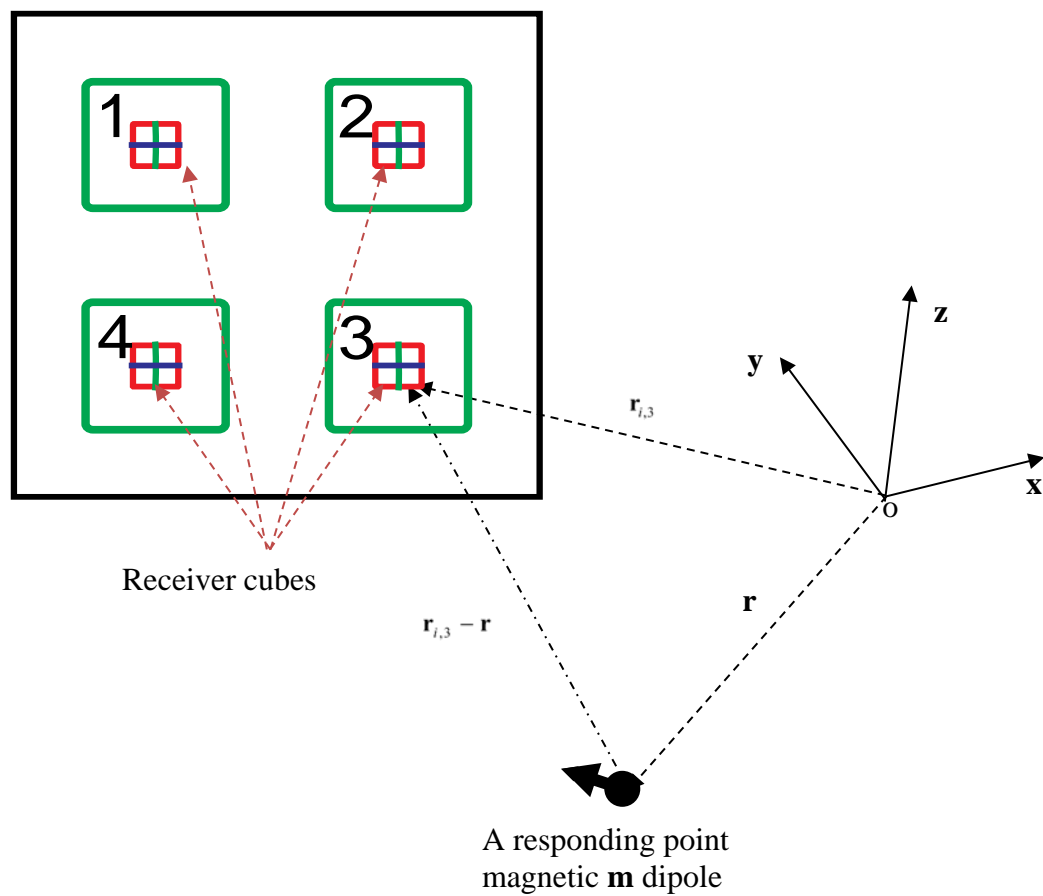


Figure 42. A schematic diagram for calculating the secondary magnetic field at location  $\mathbf{r}_{i,3}$  produced by a responding magnetic dipole  $\mathbf{m}$  placed at  $\mathbf{r}$ .

## Assessing transmitter coil detection and classification performance

In this section, numerical data are provided to assess performance improvements of advanced EMI sensors for detecting and classifying small and deep targets. Detection and classification/characterization are different processes. Detection consists of determining a yes/no answer, while characterization is a process of determining whether a target already known to be there is either UXO or clutter. Detection is a process that has not been pursued much during the development of the modern advanced TEM systems, probably because any target that can be characterized is certain to be easily detected, and because characterization is the activity that drives cost savings during clean-up of a UXO site. Characterization is a process that is more like classical *estimation* – after estimating the shape of the decay transient at every receiver, for every transmitter, the data are fed into a process that decides whether the target is UXO or non-UXO. In general, characterization (*estimation*) requires a significantly higher signal-to-noise ratio than detection. This study is based on the assumption that both *detection and classification* are objectives. In an elementary sense, detection can be thought of as a process where a signal (or, in this case, multiple signals) are processed to determine a statistic that is compared to a threshold. That statistic determines the usual receiver-operating characteristic (ROC) curves that are commonly taken to indicate the adequacy of performance of a system. This section does not look into the use of multiple sensors. It is based on a single sensor. Yet the use of multiple sensors is crucial in modern systems.

From an oversimplified perspective, there are two things that can be done to increase the maximum depth of detection and characterization: 1) increase signal, and 2) decrease noise. This section outlines EMI sensor performance improvements that result from increasing signal amplitude using either high-power and/or large transmitter loops. We also study performance improvements that could be expected from converting existing  $dB/dt$  sensors into B-field sensors, thus modifying the signal-to-noise ratio.

### 5.1.1 Primary field at target

For this study, we chose the loops shown in Table 1. This includes the *standard* TEMTADS loop that is 35 cm  $\times$  35cm, a MetalMapper loop that is 1 m  $\times$  1m, a *Large* loop that is 1.2 m  $\times$  1.2 m,

and a TEMTADS high-power loop that is the same as a TEMTADS loop but with enough more turns to make the length of wire it contains comparable to the MetalMapper loop.

**Table 1.** Electrical properties of transmitting loops modeled.

I.D.	TEMTADS	MM	Large	TEMTADSHP
Notes	Litz	Solid Cu	Litz	Litz
Length of side (m)	0.35	1	1.2	0.35
Turns	25	20	25	55
Wire length (ft)	114.8	262.4	393.6	252.56
Wire strands	16	1	16	16
Wire size	26	14	26	26
Wire strand ohms/ft	-.04102	0.002524	0.04102	0.04102
Wire ohms/ft	0.002564	0.002524	0.002564	0.002564
Wire resistance (ohms)	0.294	0.662	1.009	0.648
Wire ft/lb/strand	1310	128	1310	1310
Wire ft/lb	81.875	128	81.875	81.875
Wire wt. (lb)	1.4	2.1	4.8	3.1
Misc resistance (ohms)	0.1	0.1	0.1	0.1
Total resistance (ohms)	0.894	0.862	1.209	0.848
Battery voltage (V)	15	11	11	15
Voltage losses in switches (V)	6.5	6.5	6.5	6.5
Voltage across loop (V)	4.5	4.5	4.5	4.5
Loop Current (A)	9.5	5.2	3.7	10.0

For each of the loops we have used the numbers of turns and the wire sizes that are standard for existing systems. In all cases, for these computations, we made the *solenoid height* of the windings equal to 10 cm, which corresponds to the Tx coil heights used in the TEMTADS and MM systems. The important results in Table 1 are highlighted. The comparisons show that there is no significant difference in total resistance between a TEMTADS Litz loop, a *standard* MM loop, and a high-power TEMTADS loop.

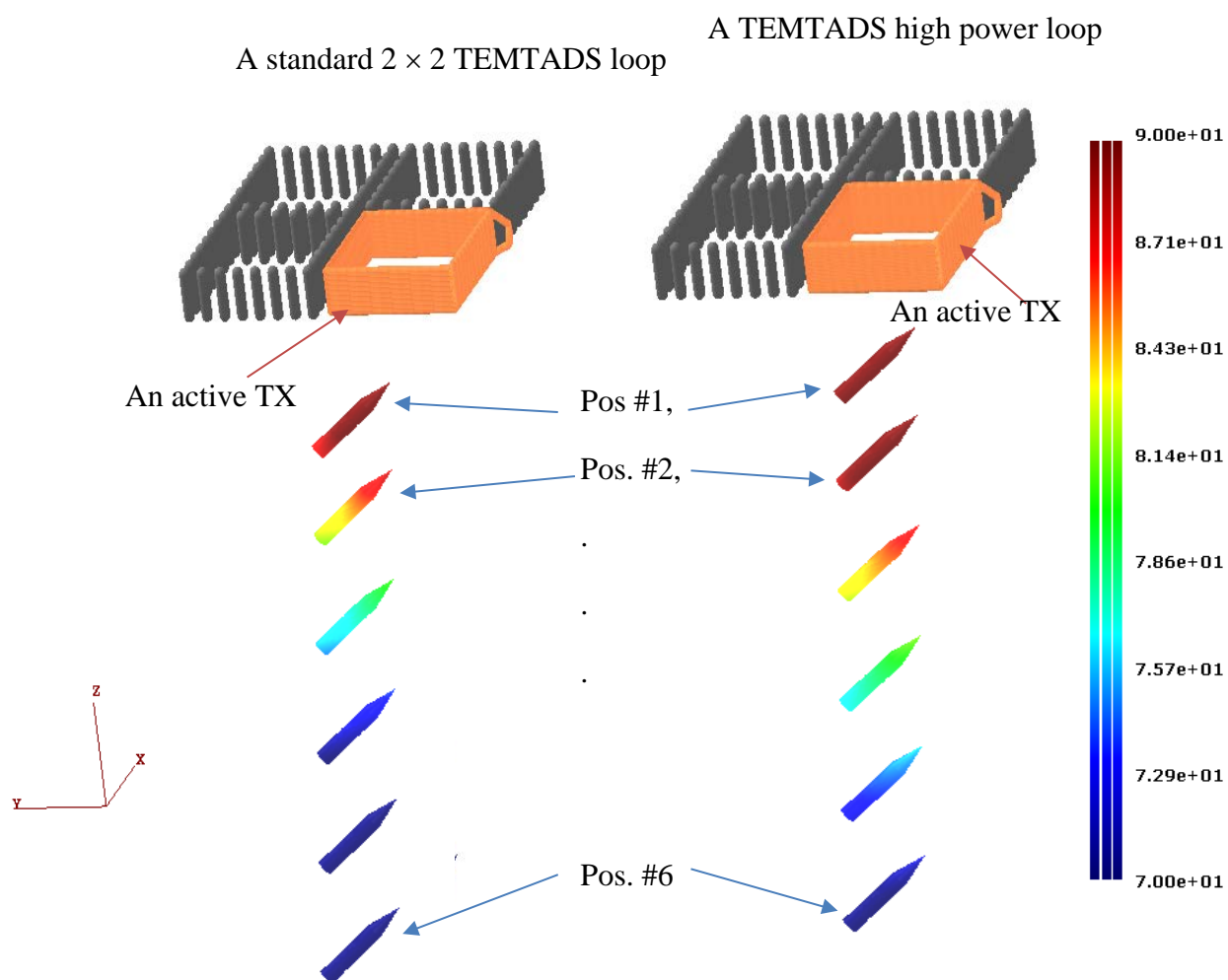


Figure 43. Primary magnetic B field due to standard (left) and high-power (right) TEMTADS transmitter loops around a small (37-mm-like) target placed at six positions. The depths at positions  $\# = 1, 2, \dots, 6$  are 30 cm, 50 cm, 75 cm, 100 cm, 125 cm and 150 cm, respectively.

Each transmitter is modeled using the method of moments. The wires are divided into segments. The transmitters are excited using an input voltage source in a wire segment. For each transmitter configuration, the input voltages are normalized to produce the loop currents specified in Table 1. The primary field around a small (37-mm-like) target for the standard TEMTADS, the high-power TEMTADS, the MetalMapper (MM), and a large  $1.2 \text{ m} \times 1.2 \text{ m}$  coil appear respectively in Figure 43 (left, right) and Figure 44 (left, right). All primary magnetic field values are given in units of dB/nT. We assume that a target is detectable for a primary field value of 78 dB/nT.

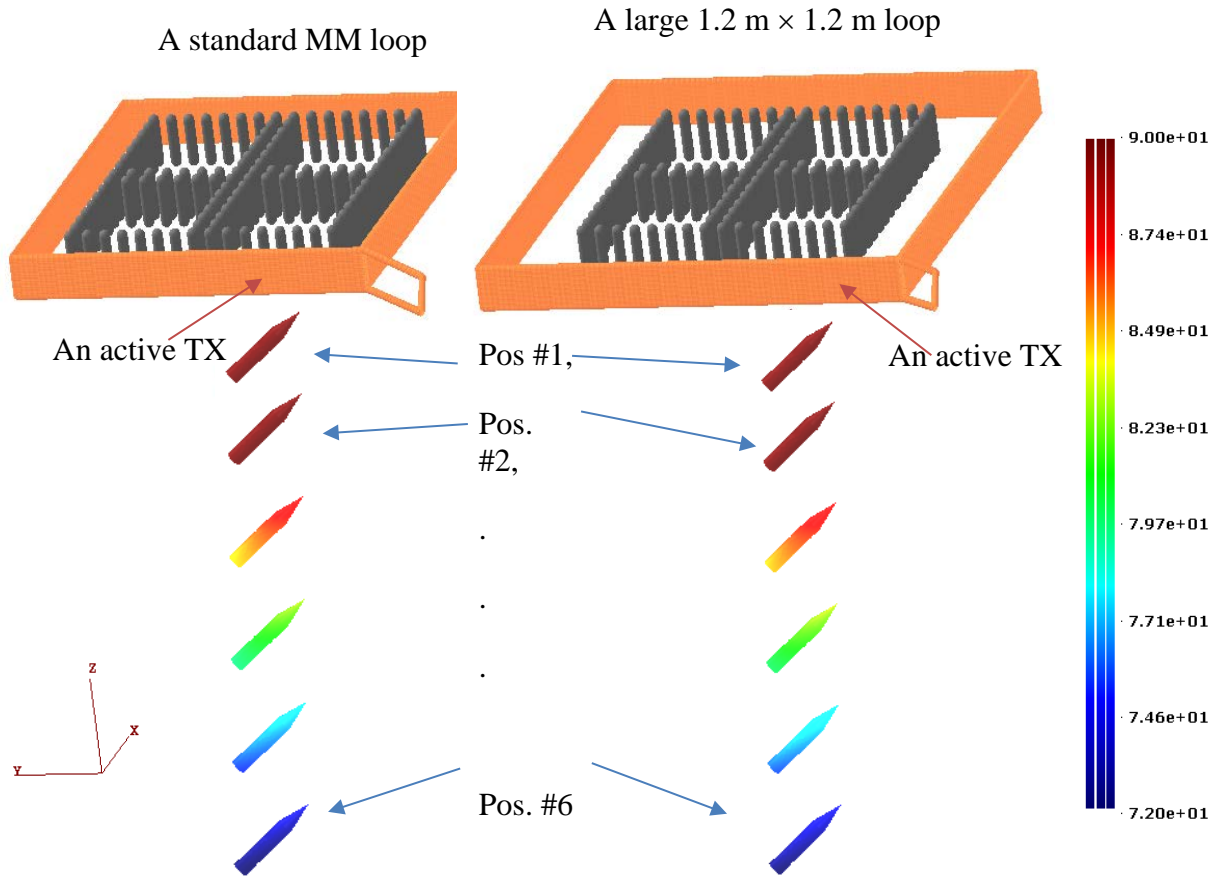


Figure 44. Primary magnetic B field due to standard MM (left) and large 1.2 m  $\times$  1.2 m (right) transmitter loops around a small (37-mm-like) target is placed at six positions. The depths at positions  $\# = 1, 2, \dots, 6$  are 30 cm, 50 cm, 75 cm, 100 cm, 125 cm and 150 cm, respectively.

This value corresponds to the strength of the standard TEMTADS primary magnetic field at a depth of  $\sim 75$  cm, where a calibration ball is barely detectable.

Note that these discussions are only about the primary magnetic field, which decays as  $\sim 1/R^3$ . Target EMI responses, which decay as  $\sim 1/R^6$ , are given in section 5.3.4. These results show that a) the primary magnetic field varies along length of the 37-mm-like target and b) standard and high-power TEMTADS coils produce good primary fields below 75 cm and 110 cm, respectively, and that the standard MM and large coils produce good signals below 130 cm. To illustrate differences between the primary magnetic field thresholds for different systems, Figure 45 shows the primary magnetic field as a function of versus distance for each system's Tx coil. The primary magnetic field is calculated at a set of points placed on the z-axis, (i.e.,  $x = y = 0$ ). In

all these calculations, the MM and large  $1.2 \text{ m} \times 1.2 \text{ m}$  Tx coils are centered at  $(x = y = z = 0)$  and the standard TEMTADS and high-power TEMTADS coils are centered at  $(x = y = 20 \text{ cm}, z = 0)$ .

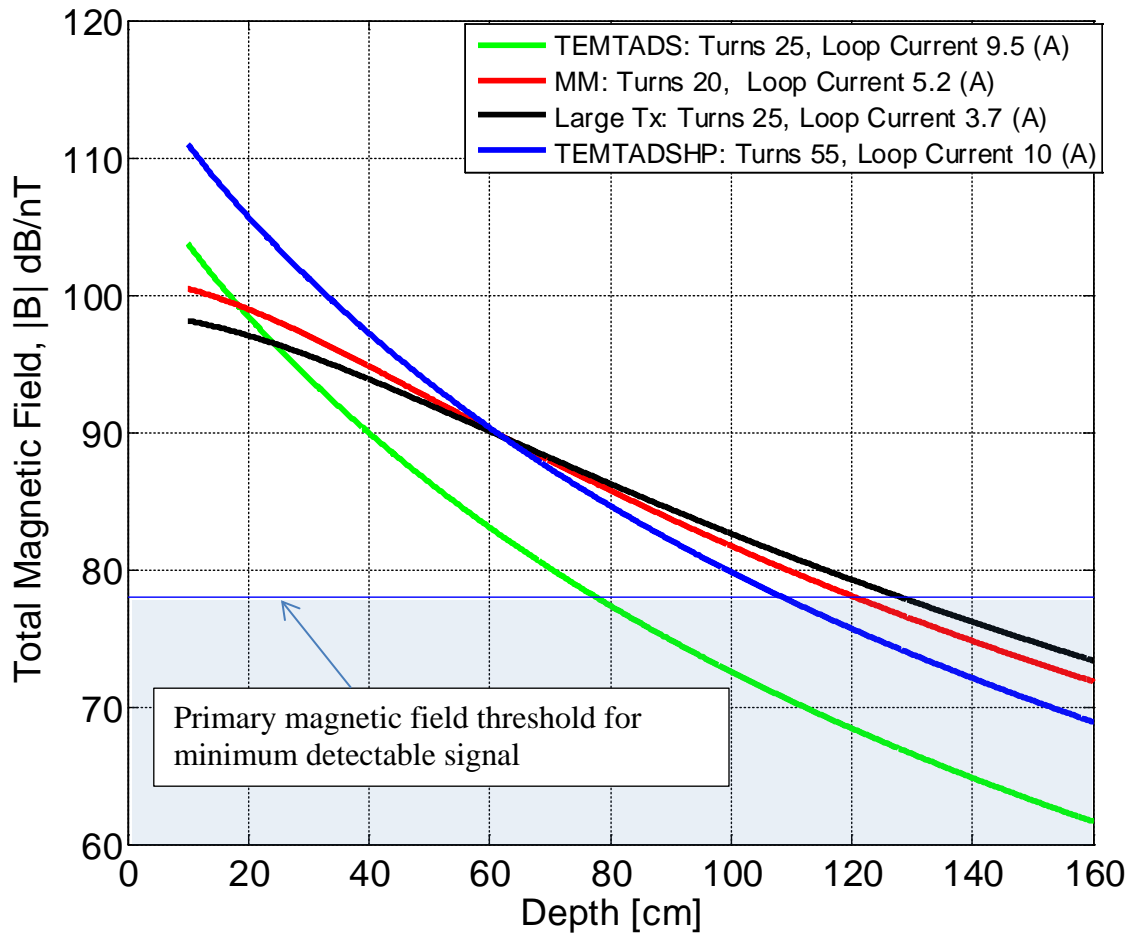


Figure 45. Primary field versus depth for standard TEMTADS, MM, large Tx, and high-power TEMTADS coils. The electrical properties of each transmitter loop are given in Table 1.

### 5.1.2 Secondary field at receiver

We use the orthonormalized volume magnetic source (ONVMS) model for estimating the secondary magnetic field at the receiver. In the ONVMS model, the magnetic field  $\mathbf{H}_i(\mathbf{r}_{i,R}^\alpha)$  is calculated using

$$\mathbf{H}_i(\mathbf{r}) = \mathbf{G}_i(\mathbf{r})\mathbf{m}_i, \quad (37)$$

where the Green function  $\mathbf{G}_i$  is given in detail in [8]. In all reported TEMTADS data studies,  $\mathbf{s}_R^\alpha$  is divided into  $N_{\mathbf{R}\mathbf{x}} = 4$  sub-areas.

To validate our advanced EMI code for the  $2 \times 2$  TEMTADS system, we conducted comparisons between modeled and measured data for different targets. Figure 46 through Figure 48 compare actual data to ONVMS predictions for one 57-mm and two 105-mm projectiles buried at the APG calibration site at depths of 32 cm, 105 cm, and 5 cm; each figure shows the  $z$ ,  $y$ , and  $x$  components of the received field. Columns 1,2,3,4 correspond to Tx #1,2,3,4, while rows 1,2,3,4 inside each cell correspond to Rx #1,2,3,4. In each case we used three responding ONVMS sources and determined their locations using a combined ONVMS-DE algorithm. The inverted locations match the actual target locations very well for all cases. The comparisons show that the model predicts a target's EMI responses very accurately.

To assess the secondary magnetic field at a receiver, in (37), the magnetic dipole moment  $\mathbf{m}$  is computed as  $\mathbf{m} = V\mathbf{H}_o$ , where  $V$  is volume of the target in  $\text{m}^3$ ,  $k$  is a polarizability factor ranging from 2 (along an axis) to 0.5 (crosswise), and  $\mathbf{H}_o$  is the primary field at the target in A/m. In this formulation we assume the target has a single polarizability aligned with the primary field, in which case  $\mathbf{m} = V\mathbf{B}_o/\mu_o$ . Next we compute the field at the receiver using (37), where

$$\mathbf{B}_s = \mu_o \mathbf{H}_s = \mu_o \mathbf{G}(\mathbf{r})\mathbf{m} = \frac{\mu_o}{4\pi R^5} (3\mathbf{R}\mathbf{R}^T - R^2\mathbf{I})\mathbf{m} \quad (38)$$

or

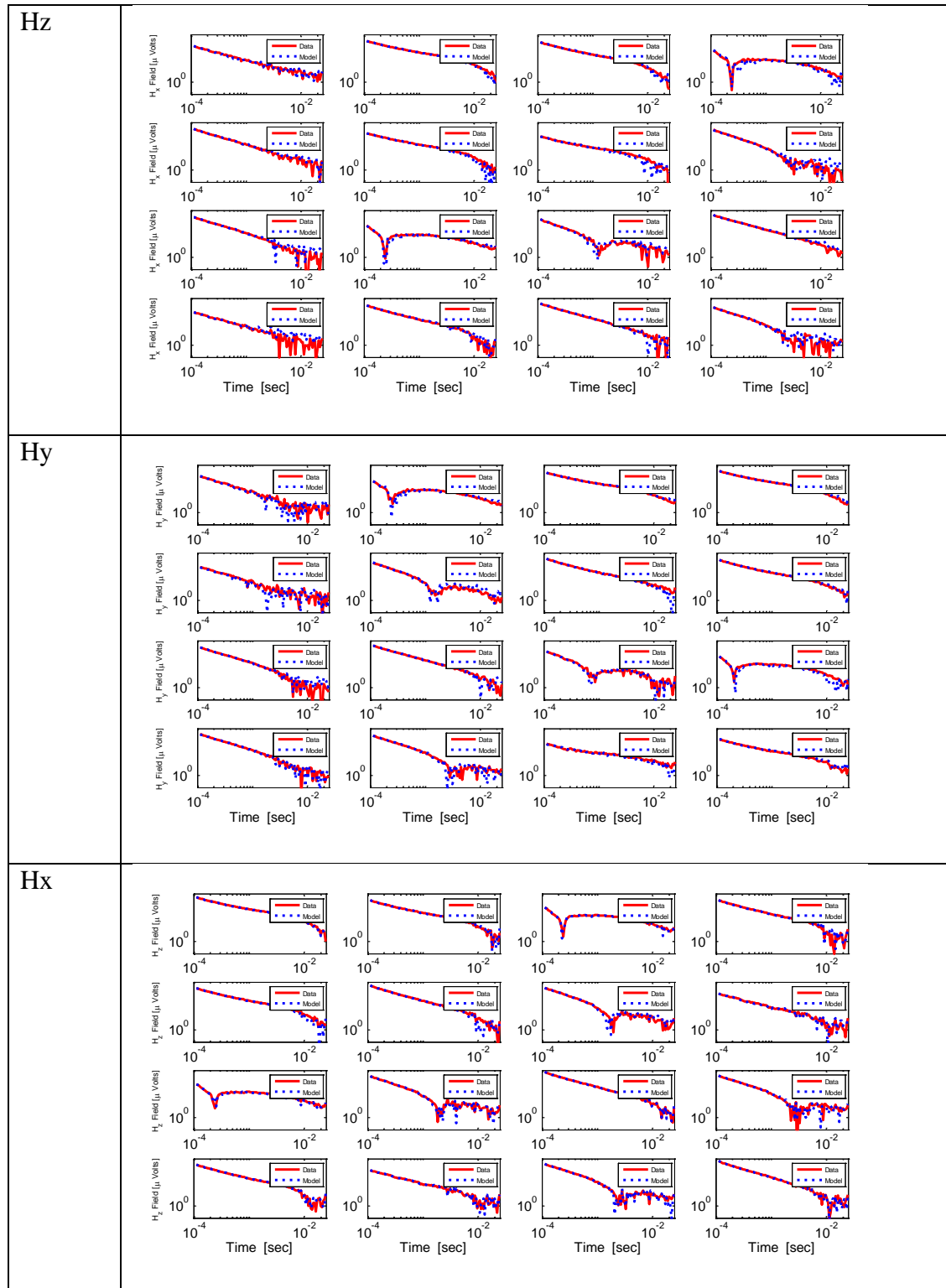


Figure 46. Comparison between modeled and measured data for APG calibration anomaly #B2. The anomaly is a 57-mm projectile buried at a depth of 32 cm.

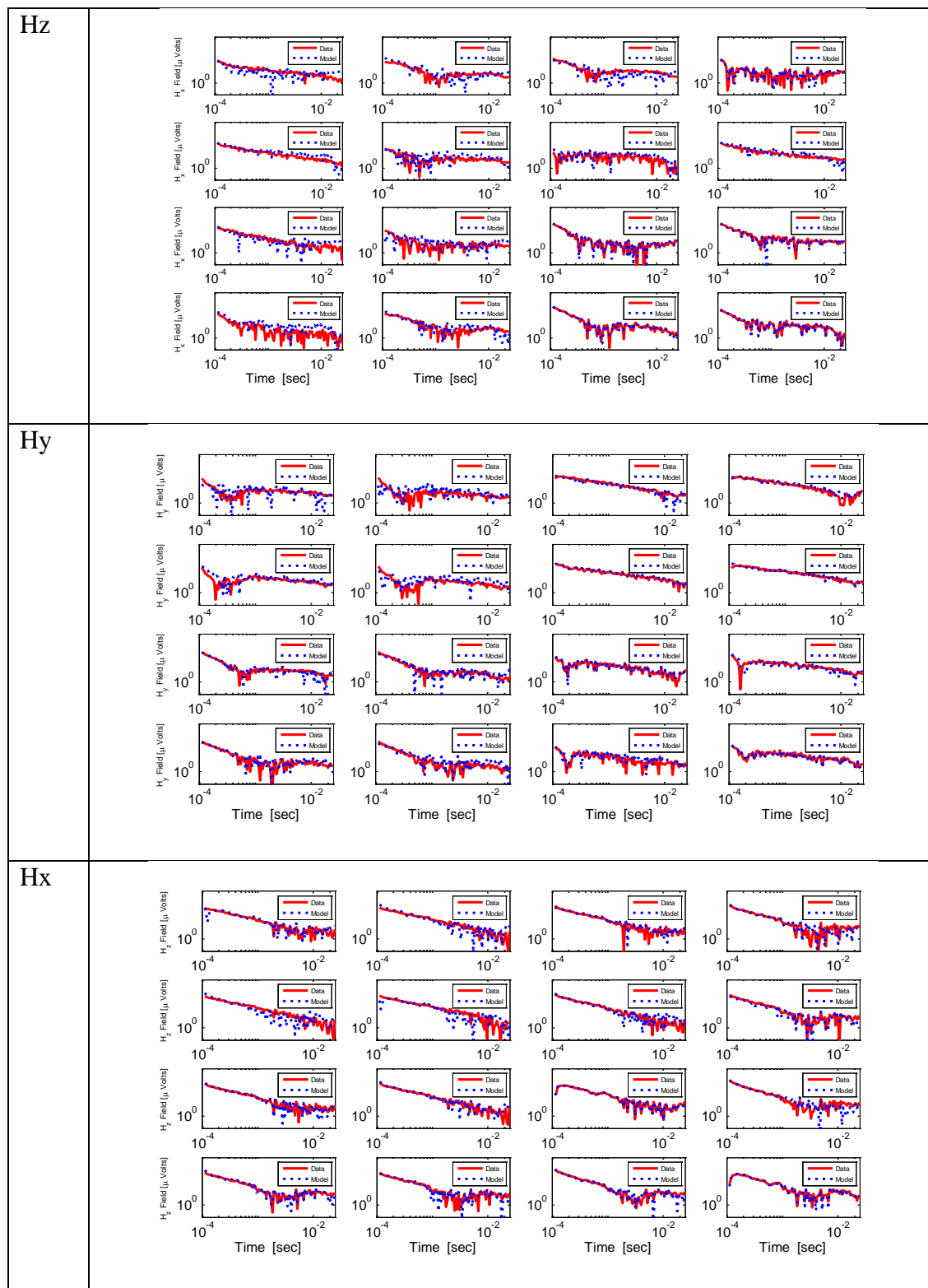


Figure 47. Comparison between modeled and measured data for APG calibration anomaly #K4. The anomaly is a 105-mm projectile buried at a depth of 105 cm.

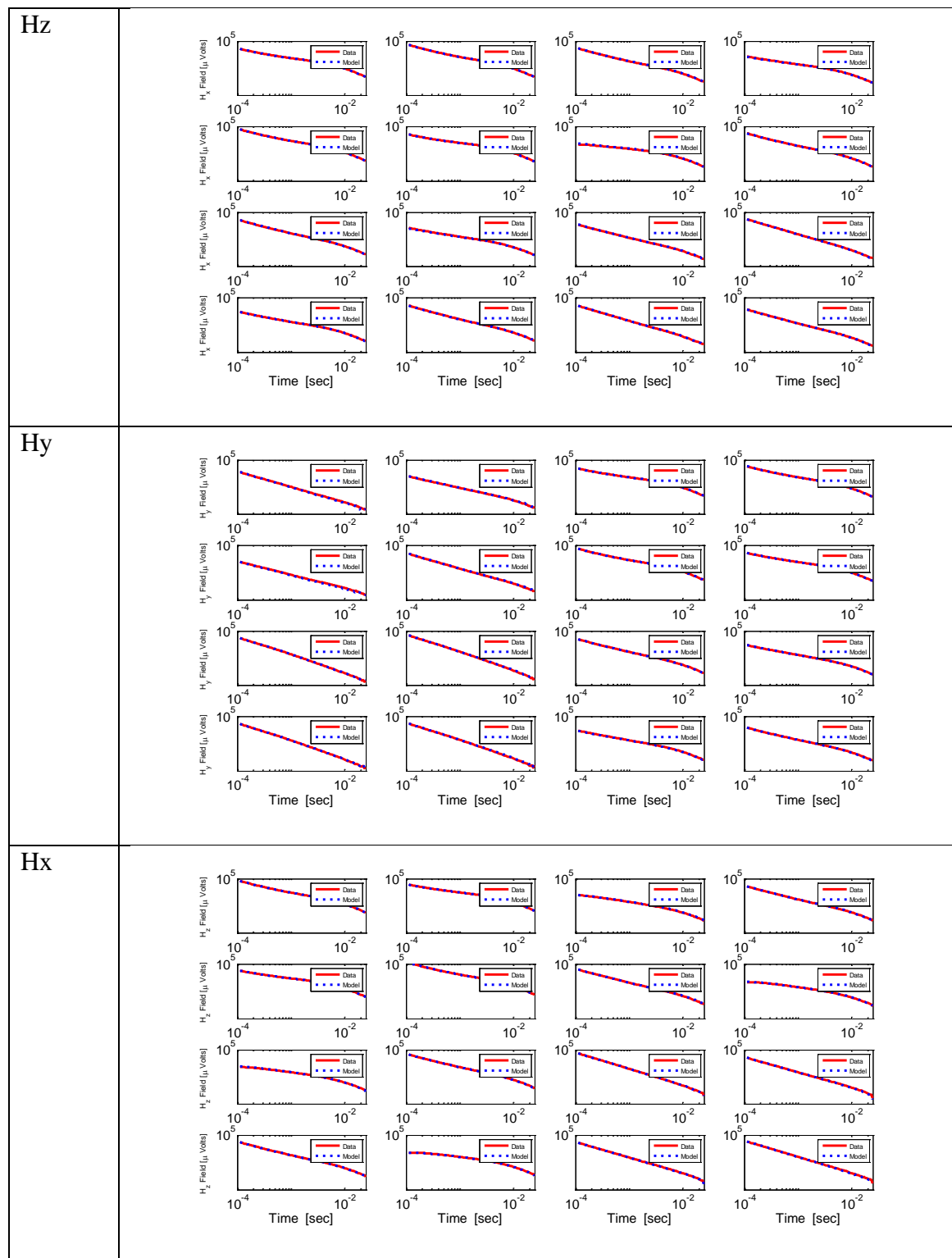


Figure 48. Comparison between modeled and measured data for APG calibration anomaly #E1. The anomaly is a 105-mm projectile buried at a depth of 5 cm.

$$\mathbf{B}_s = Vk \frac{\mu_o}{4\pi R^5} (3\mathbf{R}\mathbf{R}^T - R^2 \mathbf{I}) \mathbf{B}_p \quad \mathbf{B}_s = Vk \frac{\mu_o}{4\pi R^5} (3\mathbf{R}\mathbf{R}^T - R^2 \mathbf{I}) \mathbf{B}_p, \quad (39)$$

where  $\mathbf{R}$  is a vector pointing from the target to the receiver,  $R$  is its magnitude, and  $\mathbf{I}$  is the identity matrix. For simplicity, in this study we assume that the target has a diameter of 10 cm.

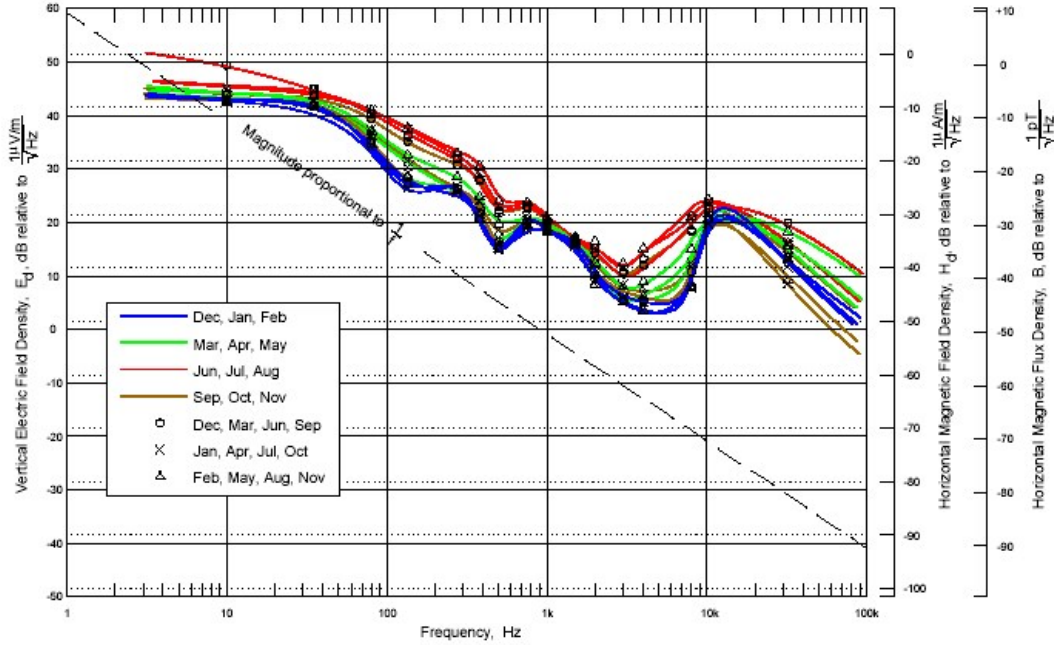


Figure 49. Noise Spectrum from Meloy 2003, taken from Chrissan and Fraser-Smith (1996).

### 5.1.3 Minimum detectable signal

To interpret the signal levels shown in the figures herein, it is necessary to make a rough estimate of a minimum detectable signal. This is done first in terms of environmental noise and second in terms of first-amplifier thermal noise. An environmental noise spectrum is shown in Figure 49. The figure shows horizontal magnetic field density because the primary data source is electromagnetic waves produced by lightning, whose propagation is waveguide-like between the earth and the ionosphere. From the practical viewpoint of estimating the noise induced into the sensors studied here, it's enough to know that a waveguide-like propagating wave has a

significant electric field vertical component as long as the earth is not a perfect conductor. Furthermore, the sensors studied here detect three components of the signal, one vertical and two horizontal.

Since we are detecting a signal transient, we must consider some appropriate bandwidth, and then integrate the curve indicated in Figure 49 over that bandwidth. For this exercise we chose an exponential signal with a 1 ms decay time constant. Note that the typical cubes used in the MM and TEMTADS systems have an effective area of  $0.5 \text{ m}^2$ , and that a typical preamp has a gain of  $\sim 2000$ , which makes an effective area of  $1000 \text{ m}^2$ . Thus care must be taken to differentiate whether we are talking voltages at the output or voltages referred to the preamplifier input or dB/dt field values. Since the signal is an exponential, it becomes easy to transform B-field signals into dB/dt field signals: both the B-field transient and the dB/dt transient are exponentials with the same time constant, and their peak amplitudes are related by the time constant. A B-field transient having a peak amplitude of 1 pT is equivalent to a dB/dt transient having a peak amplitude of 1 nT/s. For noise-spectrum purposes, the spectrum of this signal is a single pole response with a 3 dB corner frequency of 160 Hz and an equivalent noise bandwidth of 250 Hz.

First we compute the noise expected in the received signal due to environmental sources. From Figure 49 we choose an approximating spectrum that is  $1000 \text{ pT}/\sqrt{\text{Hz}}$  at 1 Hz (+30 dB relative to  $1 \text{ pT}/\sqrt{\text{Hz}}$ ), and that decays as  $1/f$  for all frequencies above 1 Hz. Since our approximating spectrum for the B field decays as  $1/f$ , the approximating spectrum for dB/dt is constant as a function of frequency: it becomes a constant noise density of  $1000 \text{ pT/s}/\sqrt{\text{Hz}}$  over the bandwidth of interest. Squaring and integrating over the presumed 250 Hz bandwidth and then taking square root produces an average rms noise of 16 nT/s.

Next we compute the noise expected in the received signal caused by electronic noise in the receiving circuits due to the sensor and its first amplifier. To compute thermal noise level, we assume that the preamp has a noise specification of  $2 \text{ nV}/\sqrt{\text{Hz}}$ , a not uncommon figure. In a bandwidth of 250 Hz this produces 31 nV (rms) referred to the input to the amplifier. For reference it is also not uncommon for electronics designers to assume that the noise produced by a first amplifier is similar to the thermal noise produced by a 1 k $\Omega$  resistor. In this case, that noise, in a 250 Hz bandwidth, is 63 nV (rms).

To compare B or dB/dt field values with voltage values at the first amplifier we assume the effective area of the receiver loop is  $1 \text{ m}^2$ , as computed from the cross-section of the receiving loop times its number of turns. A  $1 \text{ m}^2$  area is common for the receiver loops in this report. This assumption allows us to easily transform B-field or dB/dt field values into voltage values and viceversa. At the first amplifier, the noise due to environmental sources will be 16 nV (rms) and the noise due to the first amplifier will be 31 nV (rms). For the parameters chosen, thermal noise could be the limiting factor in establishing the minimum detectable signal. But the more exact solution is complicated, and is also a function that varies from survey to survey. For our purposes, the objective is to choose a *minimum detectable* signal so we can examine other factors. We choose a minimum detectable signal of 10 nV at the first amplifier, or equivalently 10 nT/s peak (dB/dt) or 10 pT peak (B).

To be thorough, we would like to illustrate that the environmental noise assumption made here is optimistic. Figure 50 shows an actual spectrum recorded with one of the early cube sensors in 2004 during development of the first AOL system. This is a graph of repeated and stacked fast Fourier transforms of a received signal recorded at Blossom Point **Error! Reference source not found.** The plot is a reasonable representation of the dB/dt field spectrum covering a huge frequency range from moderately low frequencies up to the Nyquist frequency of 400 kHz and shows the effect of the anti-aliasing filter with a corner frequency at approximately 50 kHz. More importantly, the graph shows that the observed noise spectrum at the lowest frequencies is up to two orders magnitude greater than the thermal noise level of a  $1 \text{ k}\Omega$  resistor. It also indicates that an assumption that naturally occurring fields as in Figure 49 are almost always just a fraction of the total noise present in the environment, as that noise is more accurately characterized as “noise” from man-made sources (power lines, VLF radio stations, and LF radio stations). These man-made “noise” signals are not at all random (note the spikes in the spectrum).

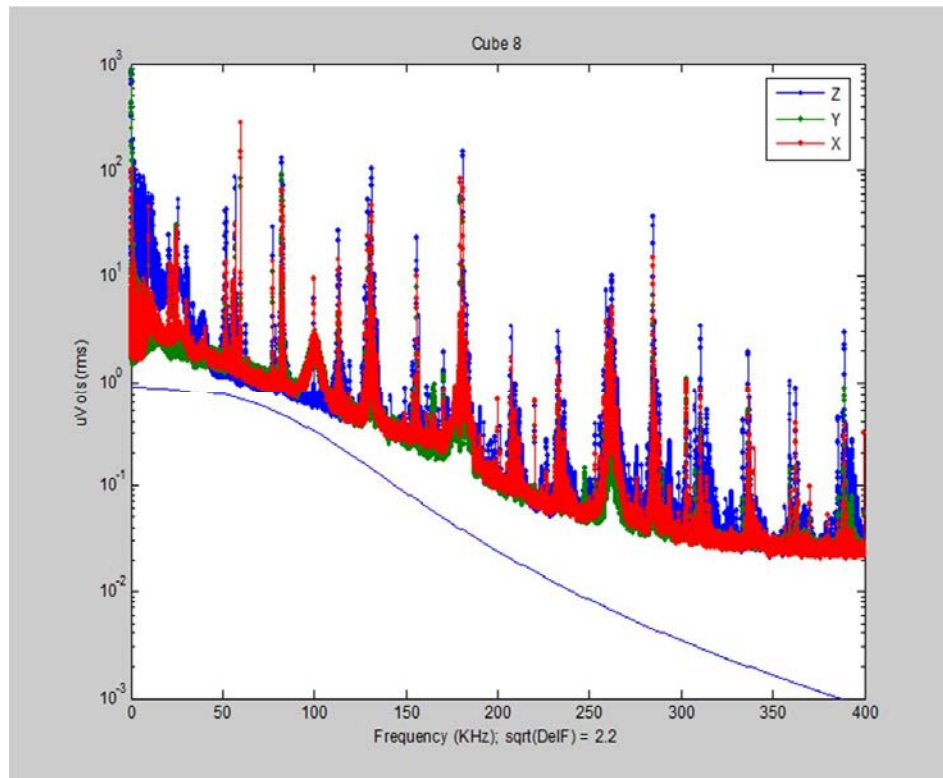


Figure 50. Baseline noise level from cube 8 compared to thermal noise of a 1 k $\Omega$  resistor. The graph shows the output of a loop with an effective area of 115 m<sup>2</sup> in units of  $\mu\text{V} / \sqrt{2.2 \text{ Hz}}$ . One must multiply the output by 5.8 to obtain B field values in nT/sec/ $\sqrt{\text{Hz}}$ .

Figure 51 shows the same spectrum expanded in two views at lower frequencies, one over the range from zero to 1 kHz and the other over the range from 1 kHz to 14 kHz. It is obvious from the figure that the man-made signals in the spectra are likely more important than the random noise levels. Yet, on the other hand, all of the spikes in the spectrum (with one or two exceptions) are due to power-line interference and are significantly reduced by the signal-repetition rates chosen for current-generation TEM systems. However, it is much harder to reduce the background induced from VLF and LF radio stations that are modulated signals. It is interesting to note that the z-component is the largest over the range from a few kHz to 14 kHz. This would not normally be expected from a propagating signal, and thus it indicates that the signals observed are from some other source: In this case, they are likely due to local power lines. Finally, it is important to point out that the magnitude of these man-made “noise” sources is varies highly from site and even from time to time.

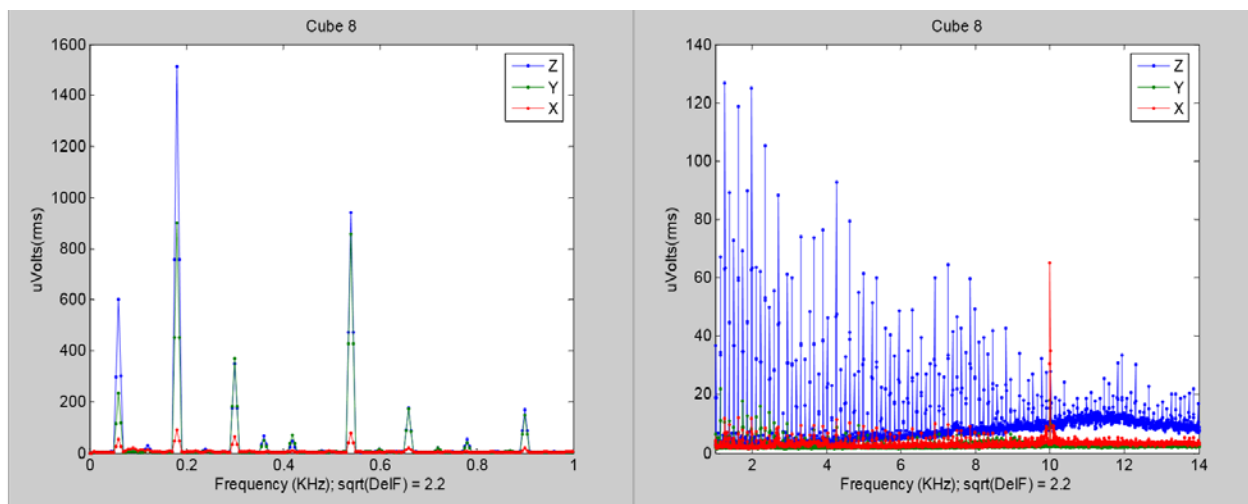


Figure 51. Expanded spectra over the lower part of the frequency range. The y-axes are displayed on a linear scale to illustrate of relative magnitudes in terms of a wideband signal.

#### 5.1.4 Comparisons between secondary field at receiver for different transmitter loops

For this study, we chose the four loops shown in Table 1 and calculated all secondary field values in units of dB/1nT. The results are shown in Figures 2 through 6 at the end of this section. The figures show the magnitude of the received signal that can be expected at the receiver, when a 10 cm diameter spherical (cal-ball) target is placed in and around the transmitter loop. The plots are a contoured cross-section of the earth where the contour indicates the position of the target. Both the receiver point and the center of the transmitter solenoid are placed 10 cm above the surface at the center of the graph. In the figures, the receiver position and the transmitter windings can be inferred by looking at the places where the contour lines bunch together.

Note the position of the 0 dB contour line. This contour corresponds to a depth where a calibration ball becomes marginally detectable: ~75 cm for the TEMTADS system, and ~1 m depth for the MetalMapper. Also note the position of the -20dB contour line. This contour corresponds to the calculation of the minimum detectable signal in the previous section. These

simple observations represent the desired results of this study: they examine the 0 dB and –20 dB contour lines to get a sense of target detectability as a function of depth and position.

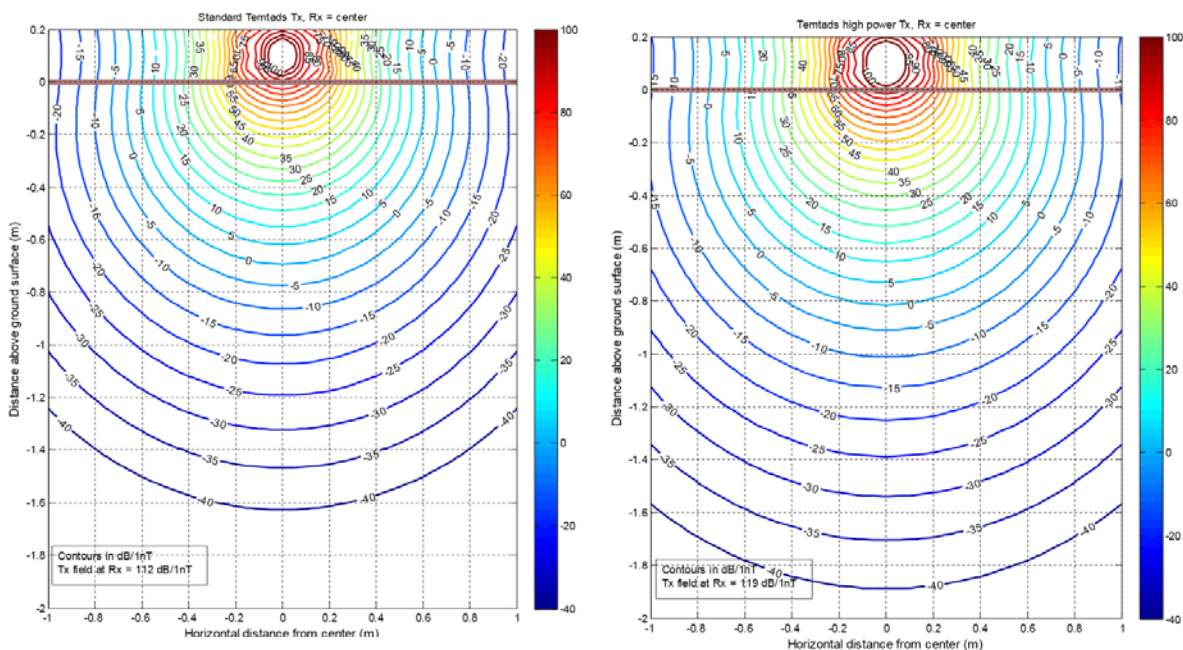


Figure 52. B-field values for (left) standard and (right) high-power TEMTADS transmitter loops.

A summary of results is shown in Table 2. The first two rows of the table show the depth at which each of the systems produces a signal of the stated amplitude. The last row shows the amplitude of the signal for the target at a depth of 2 m.

Table 2. Comparison of four transmitting loops to detect deep targets

Temtads	Temtads HP	MetalMapper	1.2m × 1.2m large coil
Depth at 0 dB contour			
68cm	82 cm	94 cm	96 cm
Depth at –20 dB contour			
106 cm	124 cm	146 cm	152 cm
Signal level at 2 m depth			
< –50 dB/nT	–43 dB/nT	–34 dB/nT	–33 dB/nT

Thus, these results illustrate that:

- Increasing the power of a TEMTADS loop by changing the number of turns from 25 to 55 increases the maximum depth of investigation from 70 cm to 80–85 cm.
- Using a standard MetalMapper loop or a  $1.2\text{ m} \times 1.2\text{ m}$  large loop increases the maximum depth of investigation from roughly 70 cm to about 95 cm.
- These increases become larger when weaker signals (i.e. at the  $-20\text{ dB}$  level) are used as the minimum detectable signal.

### 5.1.5 Combining and adjusting Tx current magnitudes and directions to improve detection and classification of small and deep targets

EMI sensing is based on the near magnetic field. As a result, target responses decay very rapidly (as  $\sim 1/\text{distance}^6$ ), posing a significant challenge for current advanced EMI sensors as they attempt to detect and classify small and/or deep targets. Studies have shown that multi-angle illuminations are required for extracting high-fidelity classification features from EMI data. There are two ways to achieve multi-angle illumination: 1) use orthogonal transmitter loops such as in Metal Mapper, or 2) combine multiple Tx coils and adjust current magnitudes and directions. This report studies the latter approach.

To demonstrate the applicability of a combined Tx loop approach for multi-angle illumination of deep and small targets, we simulated possible field distributions obtainable under the  $2 \times 2$  TEMTADS footprint. First, we calculated  $H_x$ ,  $H_y$ , and  $H_z$  magnetic-field distributions under Tx coil #1. The field distributions are depicted in Figure 53. We then combined Tx #1 and Tx #2 with same-magnitude currents and considered the cases with the currents flowing in a) opposite directions (Figure 54) and b) the same direction (Figure 55). The results show two opposite trends: when the currents flow in opposite directions, the fields are smaller than those due to a single transmitter coil, but the configuration provides richer angular excitations; when both coils carry the same currents, the total fields increase but the angular excitations remain the same. We then simulated adding a large horizontal loop around the  $2 \times 2$  TEMTADS coils. The field distribution under the large coil is depicted in Figure 56. The fields from the large coil are seen to be stronger at deep distances compared to those due to the small coils, which produce stronger fields at closer distances (**Error! Reference source not found.**). The next step was to combine the field of the large coil with the fields from the small coils. The resulting combined field distributions (large coil plus one small coil) appear in Figure 57 and Figure 58 respectively for Tx #1 and Tx #2; in both cases, the coils have currents flowing in opposite directions, and the current in the small loop has five times the magnitude of the current in the large coil. The calculated results show that it is possible to illuminate targets from multiple angles by adjusting the magnitudes and directions of the currents in the Tx coils.

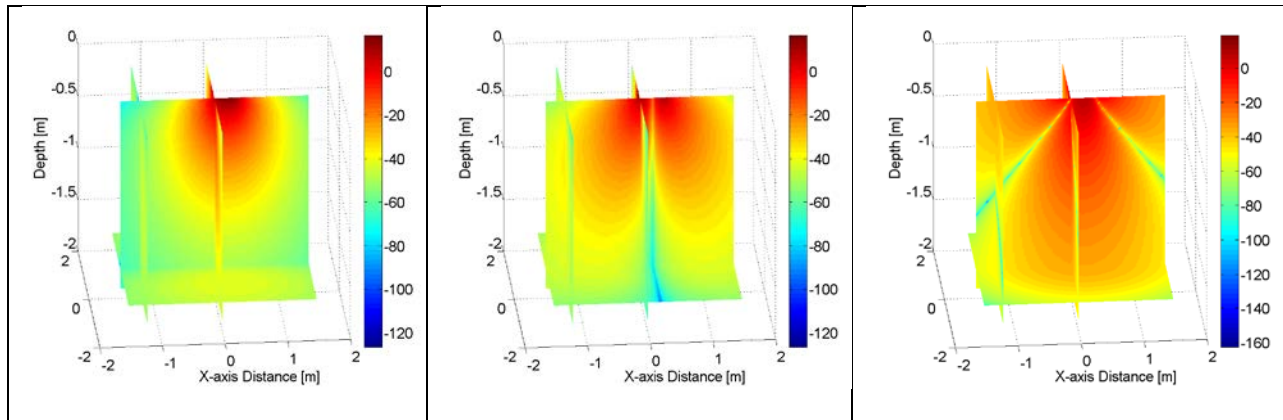


Figure 53.  $H_x$ ,  $H_y$ , and  $H_z$  field distributions (in dB) under the  $2 \times 2$  TEMTADS system footprint for Tx coil #1.

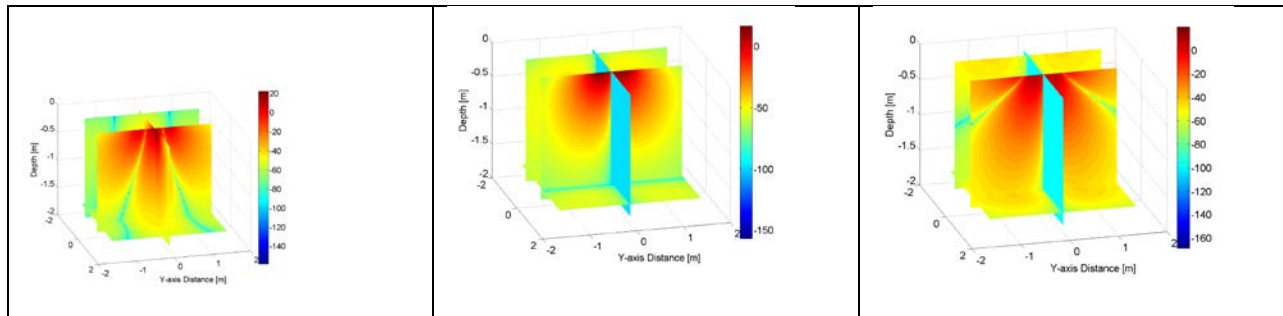


Figure 54.  $H_x$ ,  $H_y$ , and  $H_z$  field distributions (in dB) under the  $2 \times 2$  TEMTADS footprint for Tx coils #1 and #2. The coils carry currents of the same magnitude but in opposite directions.

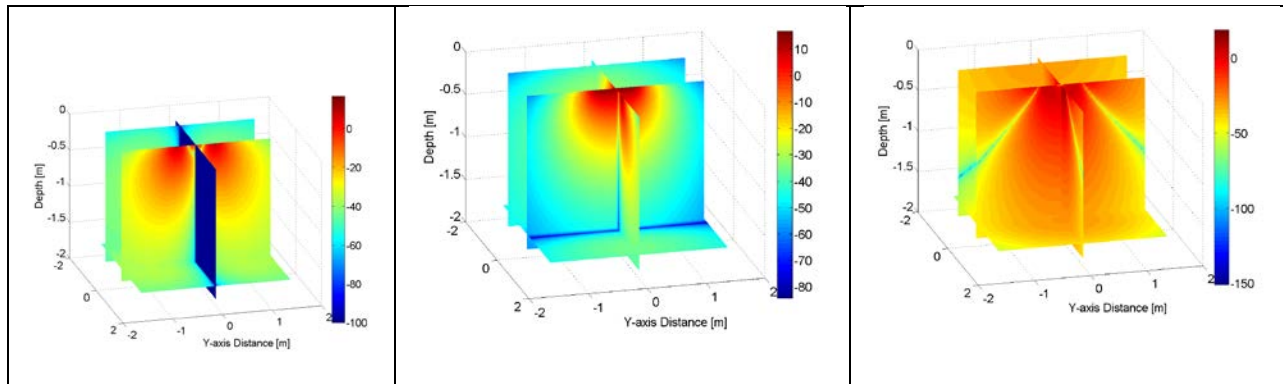


Figure 55.  $H_x$ ,  $H_y$ , and  $H_z$  field distributions (in dB) under the  $2 \times 2$  TEMTADS footprint for Tx coils #1 and #2. The coils carry equal-magnitude currents in the same direction.

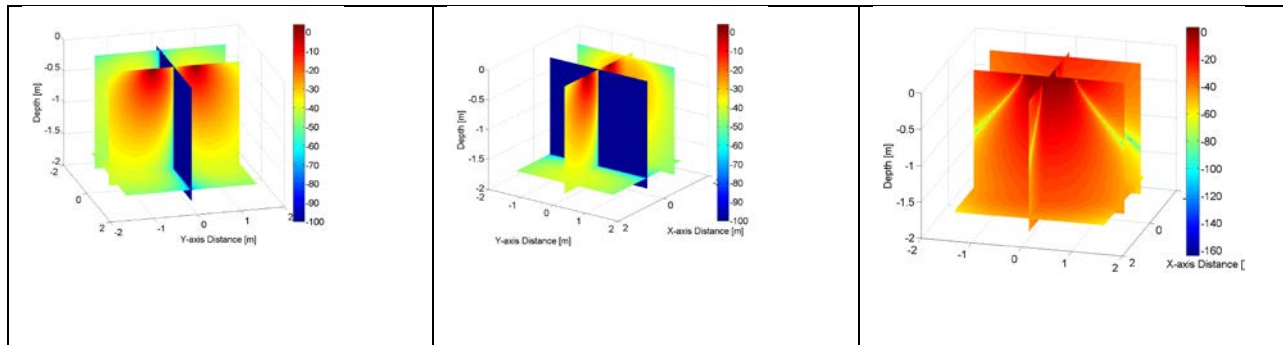


Figure 56.  $H_x$ ,  $H_y$ , and  $H_z$  field distributions (in dB) under the  $2 \times 2$  TEMTADS footprint for a large (1 m  $\times$  1 m) coil.

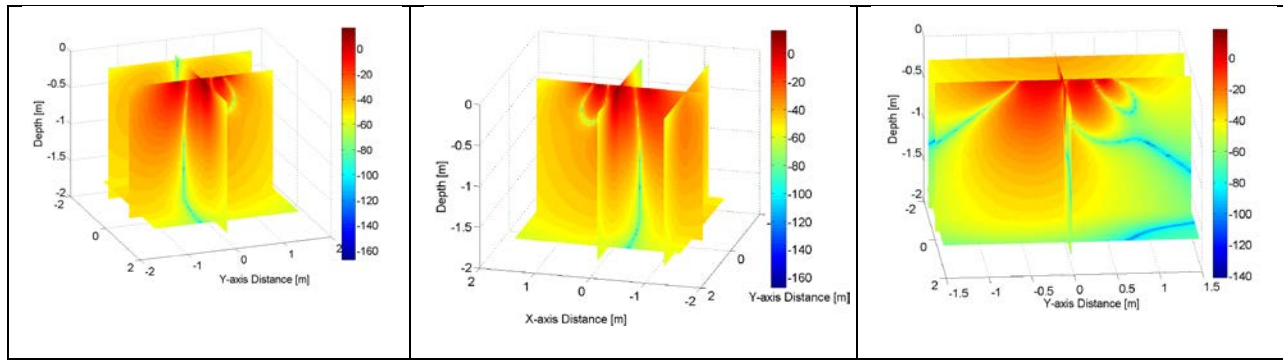


Figure 57.  $H_x$ ,  $H_y$ , and  $H_z$  field distributions (in dB) under the  $2 \times 2$  TEMTADS footprint for a large  $1 \text{ m} \times 1 \text{ m}$  coil combined with Tx #1. Currents have opposite directions in the coils, and the small coil carries a current five times stronger.

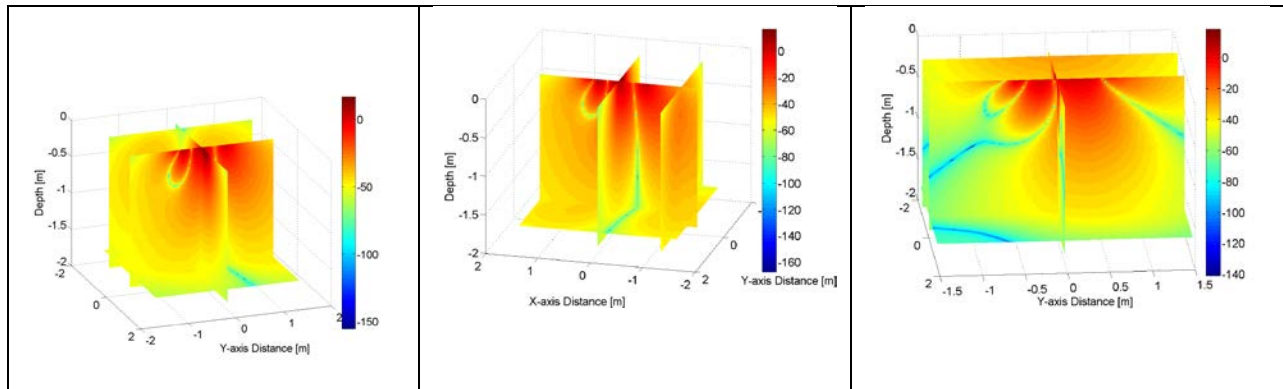


Figure 58.  $H_x$ ,  $H_y$  and  $H_z$  field distributions (in dB) under the  $2 \times 2$  TEMTADS footprint for a large  $1 \text{ m} \times 1 \text{ m}$  coil combined with Tx #2. Currents have opposite directions in the coils, and the small coil carries a current five times stronger.

## 6 APG blind and small-munitions classification studies

To illustrate the classification performance of our advanced EMI models, we conducted discrimination studies at the APG test site. The main objective of the study was to discriminate TOI from non-TOI targets and identify the TOI by type and caliber. We combined the JD, ONVMS, and DE approaches and applied them to data collected with the high-power  $2 \times 2$  TEMTADS at 1) a blind grid containing 400 anomalies and 2) a small-munitions grid containing 300 anomalies.

### APG blind grids

The APG blind-grid TOI, which varied in size from 25 mm up to 105 mm, are depicted on Figure 59.



Figure 59: The APG TOI.

There were two types of data sets: 1) calibration-grid data sets collected over the expected TOI and over some buried clutter items, and 2) blind-grid data sets collected at the 400-anomaly APG test site. According to the preliminary ESTCP data analysis, the EM response of the soil was insignificant at this site; we thus neglected it in all subsequent data inversion and discrimination analyses. Using the original measured  $2 \times 2$  TEMTADS signals, we built a square multi-static response (MSR) data matrix by combining measured signals for different transmitters. Table 3 summarizes the different combinations of transmitters considered in this process.

Table 3. A list of original and combined transmitters for creating a square MRS.

Tx1	Tx1
Tx2	Tx2
Tx3	Tx3
Tx4	Tx4
Tx5	$(Tx1+Tx2)/2$
Tx6	$(Tx2+Tx3)/2$
Tx7	$(Tx3+Tx4)/2$
Tx8	$(Tx4+Tx1)/2$
Tx9	$(Tx1+Tx2+Tx3)/3$
Tx10	$(Tx2+Tx3+Tx4)/3$
Tx11	$(Tx3+Tx4+Tx1)/3$
Tx12	$(Tx4+Tx1+Tx2)/3$

We then applied the JD technique to the MSR matrix from each anomaly and extracted its eigenvalues. The data were de-noised by setting to zero all eigenvalues below a threshold value. The de-noised data sets were processed using the combined ONVMS-DE algorithm, and intrinsic and extrinsic parameters were inverted for all targets. Comparing estimated and actual depths of the munitions correctly identified during the response stage yielded a mean error and standard deviation of 10.4 cm and 6.8 cm. (The depth is measured from the center of the munition to the surface. For the blind grid, only depth errors were calculated because the  $x$  and  $y$  positions are known and correspond to the centers of the grid square.)

We used the extracted total ONVMS and a library-matching technique to classify all blind-grid targets as either UXO or clutter. The extracted total ONVMS for APG blind-grid UXO that were classified as 25-mm, 37-mm, 60-mm, 81-mm, and 105-mm UXO are depicted in Figure 60.

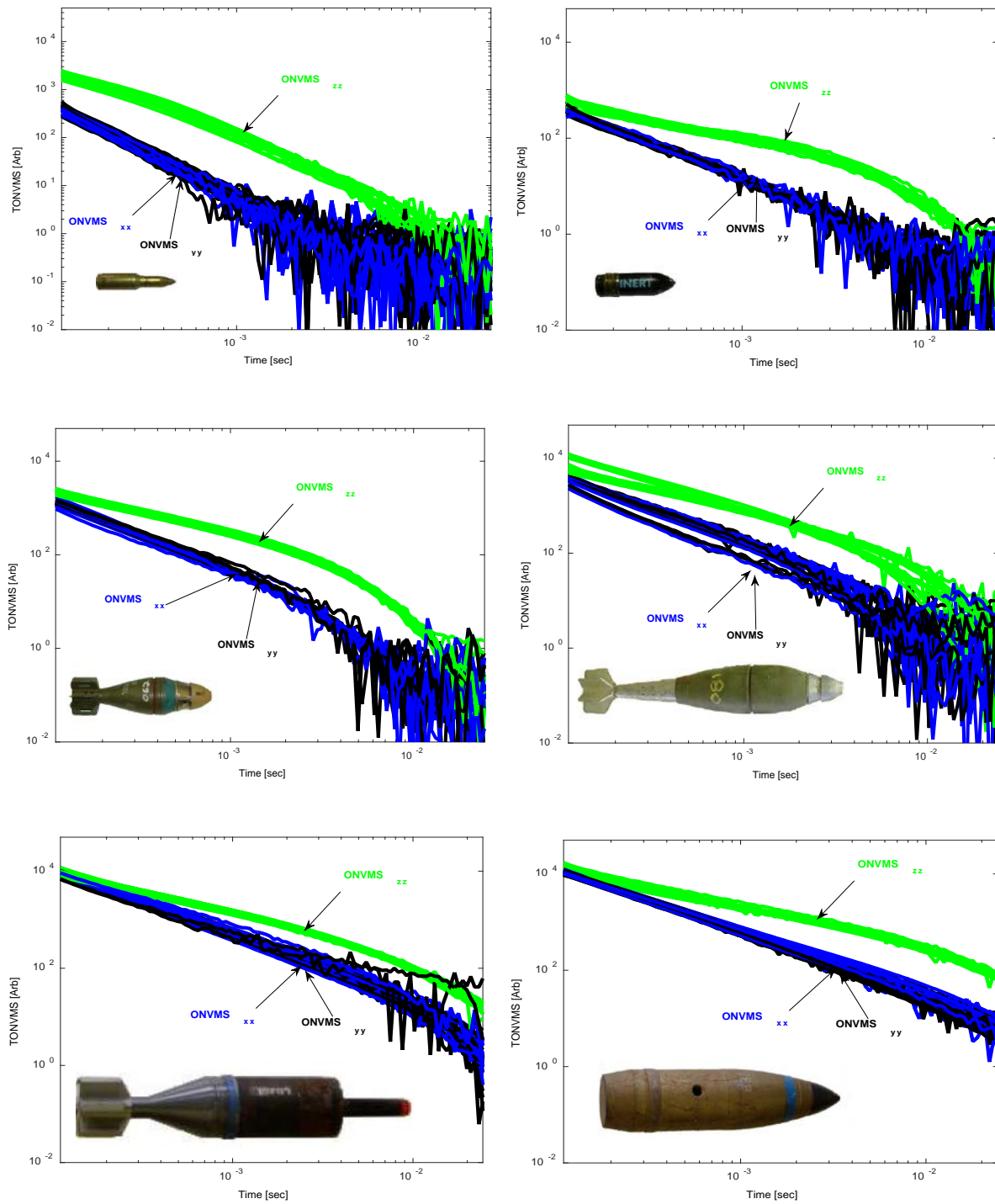


Figure 60: Extracted total ONVMS vs time for APG blind grid UXO targets.

The total ONVMS was used to classify all APG blind-test anomalies as either UXO or clutter and to create a ranked list of UXO by caliber and type. The ranked anomaly list was submitted to APG for independent scoring. The ranked results allowed estimation within each area of the probability of detection for the response stage ( $P_d^{\text{res}}$ ) and the discrimination stage ( $P_d^{\text{disc}}$ ) versus the respective probability of clutter detection or probability of false positive. The results are shown in Figure 61 and Figure 62. Both figures use horizontal lines to illustrate the performance of the demonstrator at two demonstrator-specified points: 1) at the system noise level for the response stage, representing the point below which targets are not considered detectable; and 2) at the demonstrator's recommended threshold level for the discrimination stage, defining the subset of targets the classification approach would rank targets as "dig."

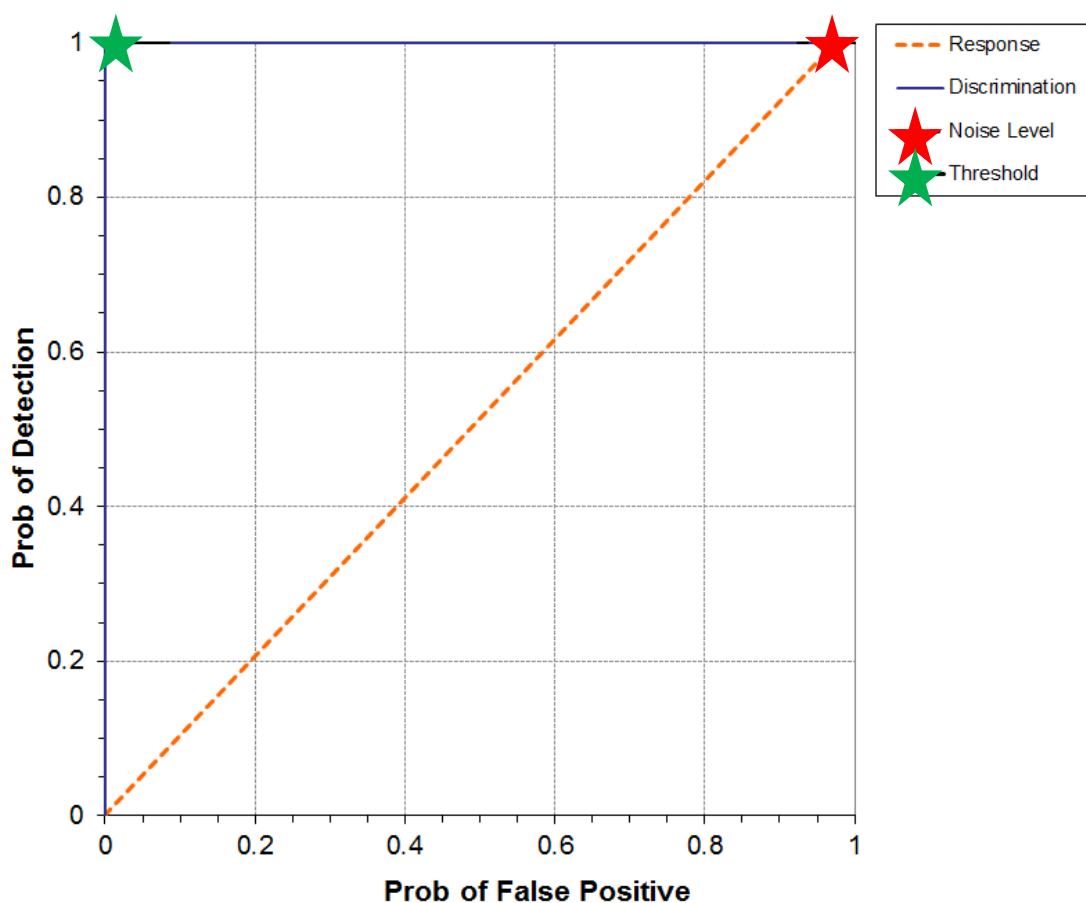


Figure 61. TEMTADS/Pushcart blind grid probability of detection for response and discrimination stages versus their respective false-positive probability.

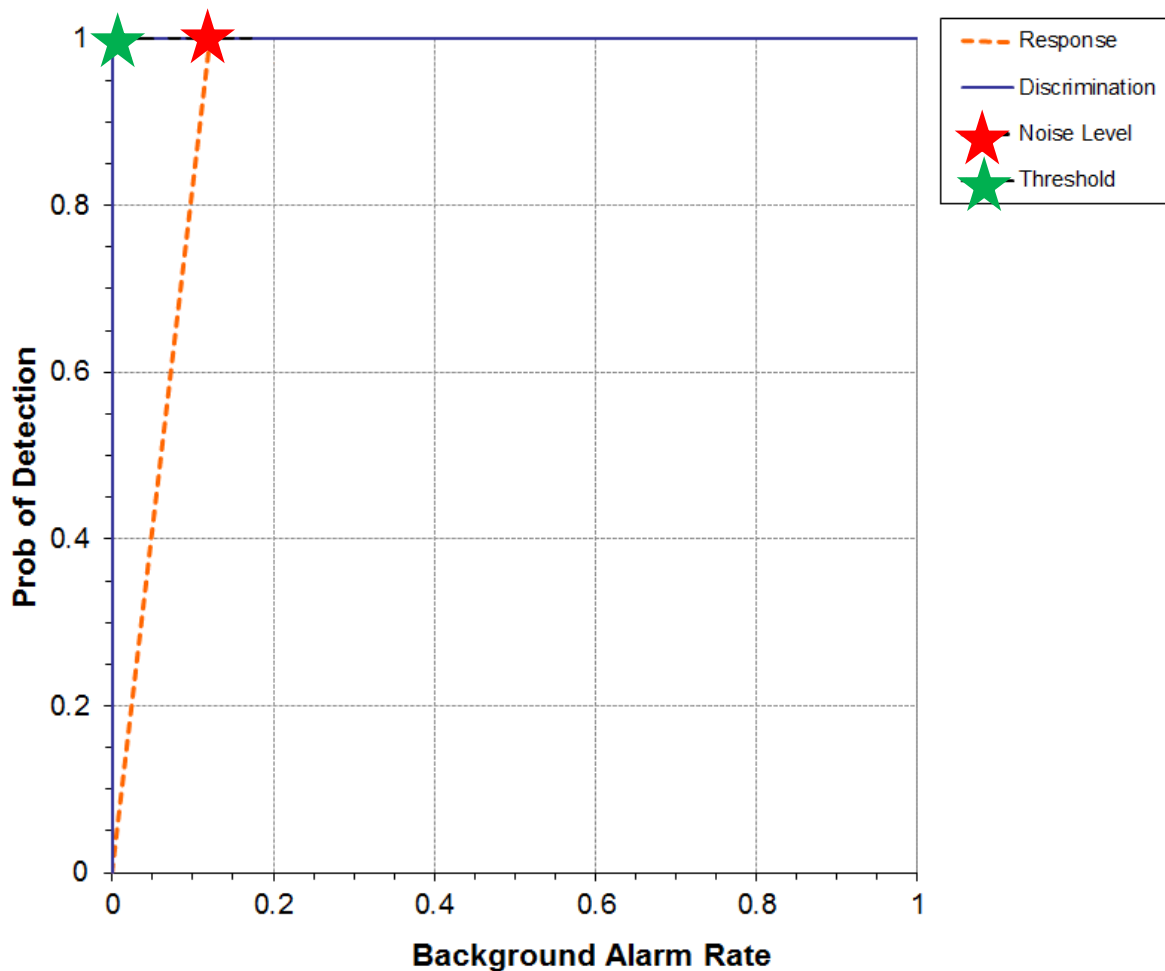


Figure 62. TEMTADS/Pushcart blind grid probability of detection for response and discrimination stages versus their respective probability of background alarm.

The overall detection and classification performance results for the APG blind-grid testing area are presented in Table 4. The response-stage results are derived from an analyst-provided list of anomalies above the data noise level. The results for the discrimination stage are derived from the classification analyst's recommended threshold for optimizing munitions-related cleanup by minimizing false-alarm digs and maximizing munition recovery. The lower and upper 90-percent confidence limits on  $P_d$ ,  $P_{cd}$ , and  $P_{fp}$  are calculated assuming that the number of detections and false positives are binomially distributed random variables.

Table 4. Blind-grid test area results

Response Stage					Discrimination Stage			
Munitions <sup>a</sup> Scores	Pd <sup>res</sup> : by type				Pd <sup>disc</sup> : by type			
	All Types	105-mm	81/60-mm	37/25-mm	All Types	105-mm	81/60-mm	37/25-mm
	1.00	1.00	1.00	1.00	1.00	1.00	1.00	1.00
	1.00	1.00	1.00	1.00	1.00	1.00	1.00	1.00
	0.98	0.93	0.93	0.93	0.98	0.93	0.93	0.93
By Depth <sup>b</sup>								
0 to 4D	1.00	1.00	1.00	1.00	1.00	1.00	1.00	1.00
4D to 8D	1.00	1.00	1.00	1.00	1.00	1.00	1.00	1.00
8D to 12D	1.00	1.00	1.00	1.00	1.00	1.00	1.00	1.00
Clutter Scores	P <sub>cd</sub>				P <sub>fp</sub>			
By Mass								
By Depth <sup>b</sup>	All Mass	0 to 0.25 kg	>0.25 to 1 kg	>1 to 8 kg	All Mass	0 to 0.25 kg	>0.25 to 1 kg	>1 to 8 kg
All Depth	0.99				0.07			
	0.98	0.95	1.00	1.00	0.03	0.00	0.02	0.30
	0.95				0.02			
0 to 0.15 m	0.99	0.98	1.00	1.00	0.02	0.00	0.00	0.33
0.15 to 0.3 m	0.88	0.60	1.00	1.00	0.13	0.00	0.14	0.25
0.3 to 0.6 m	N/A	N/A	N/A	N/A	N/A	N/A	N/A	N/A
Background Alarm Rates								
P <sub>ba</sub> <sup>res</sup> : 0.12					P <sub>ba</sub> <sup>disc</sup> : 0.00			

<sup>a</sup> In cells with offset data entries, the numbers to the left are the result and the two numbers to the right are an upper and lower 90-percent confidence interval for an assumed binomial distribution.

<sup>b</sup> All depths are measured to the center of the object.

In addition, APG personnel calculated efficiency and rejection rates to further quantify the discrimination ability at specific points of interest on the ROC curve: 1) at the point where no decrease in  $P_d$  is suffered (i.e., the efficiency is by definition equal to one), and 2) at the operator-selected threshold. These values for the APG blind grid are presented in Table 5.

Table 5. Blind-grid efficiency and rejection rates

	<b>Efficiency (E)</b>	<b>False Positive Rejection Rate</b>	<b>Background Alarm Rejection Rate</b>
At Operating Point	1.00	0.97	1.00
With No Loss of $P_d$	1.00	1.00	1.00

All the munitions items that were detected and correctly discriminated were further scored on whether they could be identified correctly by type. (We received a list of expected standard-type munitions prior to testing). The results appear in Table 6. Correct-type examples include 25-mm projectiles and 105-mm HEAT rounds. Results show that our approach was able to classify all 25-mm, 37-mm, 60-mm and 81-mm UXO with 100% accuracy. There were a few misclassifications between 105 mm and 105-mm artillery projectiles.

Table 6. Blind correct-type classification of targets correctly discriminated as munitions

Size	Percentage Correct
25-mm	100%
37-mm	100%
60-mm	100%
81-mm	100%
105-mm	87%
105-mm artillery	93%
Overall	97%

### APG small-munition grids

The APG small-munitions test site consists of 300 grids, and the expected TOI are 20-mm, 37-mm, and 40-mm projectiles buried at depths of up to 20 times the munition sizes. The site is highly contaminated with clutter, and in addition there were single (uncapped) and multiple (capped) anomalies. We deployed the high-power  $2 \times 2$  TEMTADS system, collected data at the center of each grid, and processed the data using our advanced EMI models to extract the intrinsic and extrinsic parameters of all targets. We then sorted the anomalies as either UXO or non-UXO and submitted a ranked list to APG personnel for independent scoring. The results were scored using two categories: 1) all munitions (20-mm, 37-mm, and 40-mm) and 2) munitions larger than 20 mm. In addition, each category was broken into capped and uncapped test areas.

The probability of detection for the response stage ( $P_d^{\text{res}}$ ) and the discrimination stage ( $P_d^{\text{disc}}$ ) versus their respective probability of clutter detection or probability of background alarm are shown in Figure 63 for capped test areas and in Figure 64 for uncapped test areas.

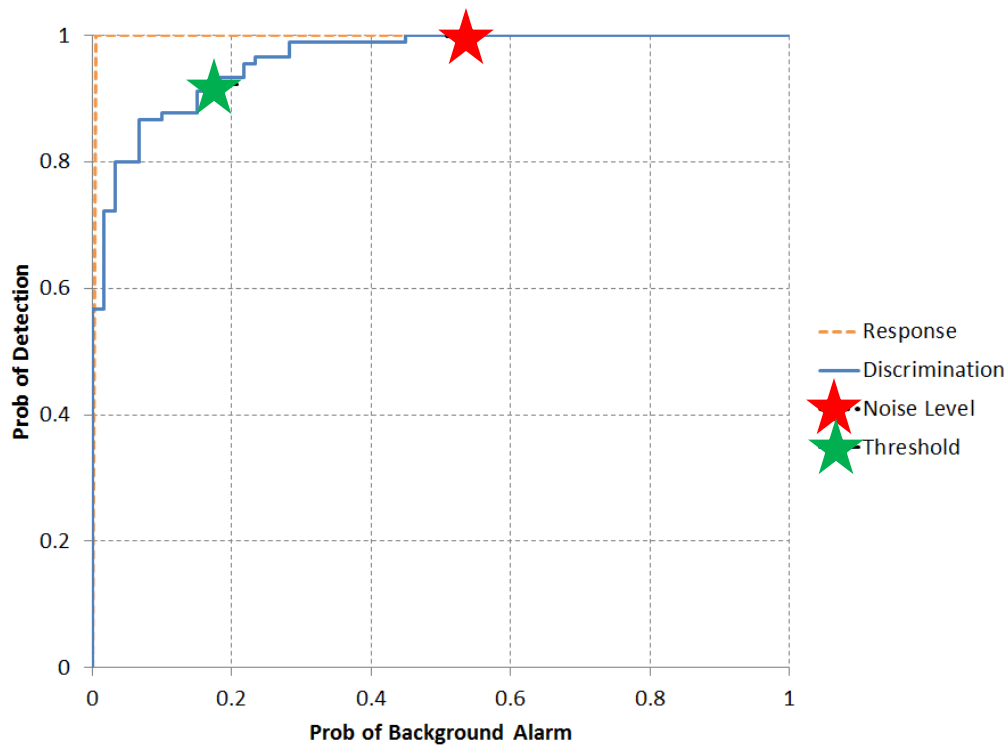


Figure 63. TEMTADS/Pushcart capped test-area probability of detection for response and discrimination stages against their respective probability of background alarm.

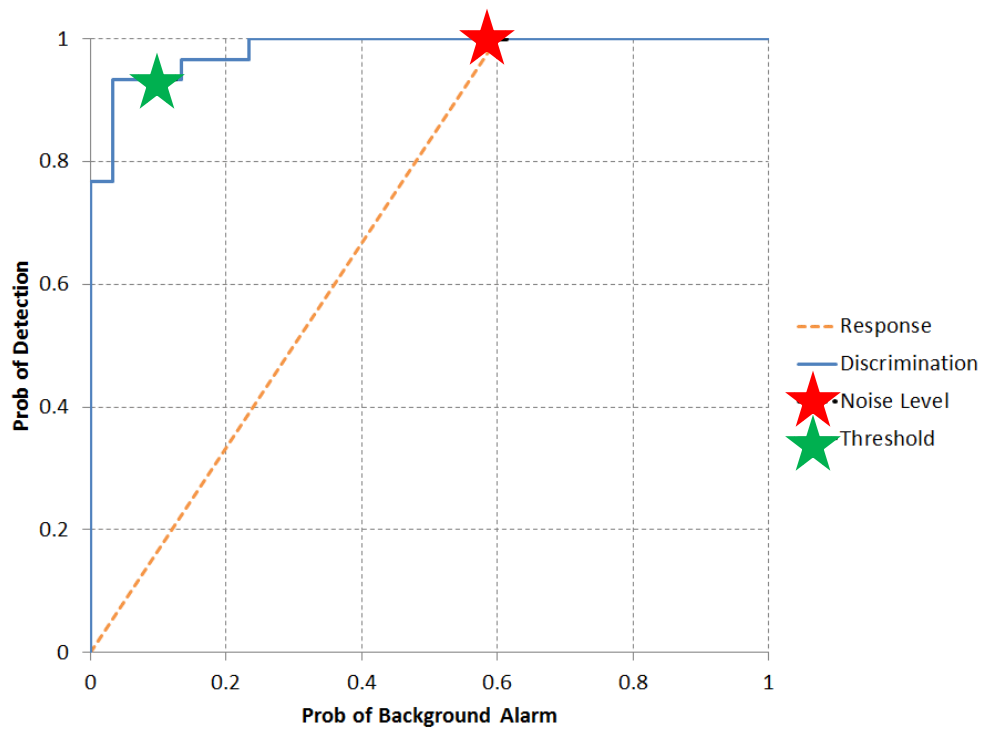


Figure 64. TEMTADS/Pushcart uncapped test-area probability of detection for response and discrimination stages against their respective probability of background alarm.

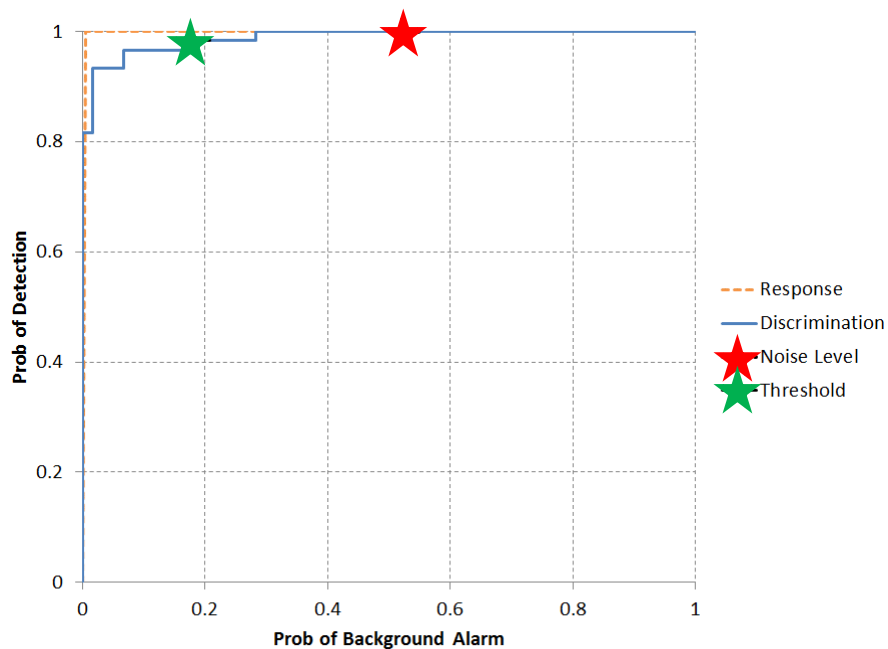


Figure 65. TEMTADS/Pushcart capped test area probability of detection for response and discrimination stages against the respective probability of background alarm for all ordnance larger than 20 mm.

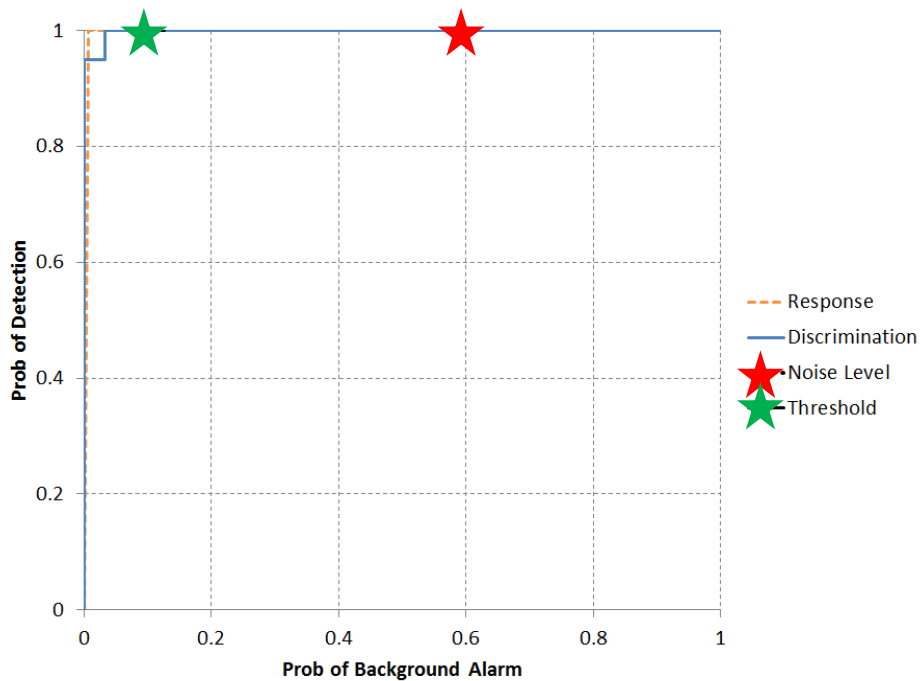


Figure 66. TEMTADS/Pushcart uncapped test area probability of detection for response and discrimination stages against the respective probability of background alarm for all ordnance larger than 20 mm.

Similarly, the probability of detection for the response stage ( $P_d^{\text{res}}$ ) and the discrimination stage ( $P_d^{\text{disc}}$ ) versus the respective probability of background alarm rate when only ordnance larger than 20 mm are considered appear in Figure 65 for capped test areas and in Figure 66 for uncapped test areas. The results show that our approach was able to classify all 37-mm and 40-mm projectiles, except for one capped deeply buried 37-mm target.

## 7 Results and discussion

The main objectives of this project were to combine advanced EMI models and next-generation EMI systems with updated electronics and to demonstrate the combined system's detection and classification capabilities for small and deep targets. There are two ways to increase the maximum depth of detection and classification: 1) increase signal strength by using high-power and/or large transmitter coils and 2) decrease noise strength by extracting B fields from  $dB/dt$  signals or gating signals.

- The JD technique was adapted to next-generation EMI systems. The technique is a fast and robust approach to assess data quality and to provide real-time feedback to the data collection team. Studies conducted using APG blind site and Blossom Point test-stand  $5 \times 5$  TEMTADS datasets shows that the method can be used in the field to collect high-quality data for detection and classification of small and deep targets. The JD technique can also be used to choose the optimal Tx/Rx combination for robust estimation of classification features and for sensor guiding.
- We have employed a combined JD-MUSIC algorithm to locate subsurface UXO targets for  $2 \times 2$  TEMTADS. The critical step in this method is to identify the number of signal-related eigenvalues in JD, as the accuracy of both noise-filtering and the MUSIC algorithm heavily rely on it. Extracting this key information is a challenging under low SNR conditions, when the separation between signal and noise is poor. The majority of the computational workload for the MUSIC algorithm to estimate target locations comes from calculating the Green function for each grid. For a next-generation EMI sensor, this can be done beforehand, and the rest of the calculation can be carried out in near-real-time on a laptop. This provides a new possibility for evaluating data quality immediately after the data are collected, and to take countermeasures if the SNR is unsatisfactory.
- We investigated a large Tx loop's target detection and discrimination capabilities by combining different Tx and using a large Tx loop. We demonstrated that a simple superposition of target responses for different Tx combinations can provide negligible enhancement for classification-feature extraction and that a large Tx loop can improve detection of deep and small targets. However, preserving system resistance means that

increasing Tx loop size requires fewer turns, and thus we concluded that to achieve better spatial Tx/Rx resolution and target multi-viewpoint illuminations it is better to increase current magnitudes in the Tx loop rather than increase the loop size.

- We studied the ability of next-generation EMI sensing technologies and advanced inversion models to detect and classify in cued mode small and deep targets (i.e., with burial depths more than 11 times targets diameter). To that end we considered modifying Tx coil current magnitudes and EMI system electronics. The updated system now allows increasing Tx currents from 6 A to 14 A. Our studies show that small and deep targets such as a 37-mm projectile buried at a depth of 90 cm (or ~24 diameters) can be detected and classified reliably using a 14 A Tx current. In other words, increasing Tx currents enables the primary magnetic field to reach deep targets and induce eddy currents and magnetic dipoles in them. In return, those induced currents and dipoles produce strong secondary magnetic fields that overcome noise levels. Once target signals exceed noise levels, then advanced models such as JD and ONVMS can discriminate targets accurately. These studies were conducted using test-stand data sets. We expect that magnetic and highly conducting soils (plus target offsets from the sensor center) can degrade deep and/or small target detection and classification at ~24 diameters. Therefore, to further demonstrate system robustness for actual UXO sites, we updated  $2 \times 2$  3D TEMTADS electronics, which generate high currents, and will conduct detection and classification of small and deep targets at APG blind test-sites for independent scoring.
- We investigated the robustness of the ONVMS technique for detection and classification of small and deep targets. The method was applied to AN M30 Bomb MetalMapper test-stand data sets, and the resulting inverted parameters were analyzed from a classification viewpoint. The ONVMS method is seen to be applicable for detection and classification of shallow targets, and is now seen to provide very accurate classification features for deep targets.
- We studied four transmitter loops, which, including the standard TEMTADS loop that is 35 cm  $\times$  35 cm, a MetalMapper loop that is 1 m  $\times$  1 m, a *Large* loop that is

1.2 m  $\times$  1.2 m, and a TEMTADS high-power loop that is the same as a TEMTADS loop but with enough more turns to make the length of wire it contains comparable to the MetalMapper loop. Studies showed that increasing the power of a TEMTADS loop by changing the number of turns from 25 to 55 increases the maximum depth of investigation from 70 cm to 80–85 cm. Using a standard MetalMapper loop, or using a 1.2 m  $\times$  1.2 m large loop, increases the maximum depth of investigation from roughly 70 cm to about 95 cm. These increases become larger when weaker signals (for example at the –20 dB level) are used as the minimum detectable signal.

- We investigated the target detection and discrimination capabilities of large Tx loops both by combining different Tx and by adding a large Tx loop to the sensor assembly. We demonstrated that by adjusting the magnitudes and directions of the currents in the Tx coils it is possible to illuminate targets from multiple angles and thus enhance classification.
- We studied both primary and secondary B fields and  $dB/dt$  signals to decrease noise for detecting and classifying small and deep targets. (A “deep” target here is one buried at a depth more than 11 times its diameter.) Small and/or deep target detection and classification performance was compared between B fields and  $dB/dt$  signals. Since the induction receiver loop senses  $dB/dt$ , we expected that differentiation would increase noise and that integrating the signal from the  $dB/dt$  sensor would reduce noise. However, our studies showed that, while integrating the  $dB/dt$  signal does reduce noise, it also reduces the signal, and the net effect does not substantially increase the signal-to-noise ratio. For more details see the Appendix on Minimizing noise.
- We deployed the high-power 2  $\times$  2 TEMTADS system, with 14 A transmitter currents, to the APG site in 2015 and used it to collect data at the blind and small-munition sites. The data were processed using a combined ONVMS-DE approach, and targets’ intrinsic and extrinsic parameters were extracted. Targets were classified as either UXO or non-UXO using the extracted extrinsic parameters. Excellent classification results were obtained at both grids for all anomalies larger than 20 mm.

## 8 Project-related publications

- [1] I. Shamatava, F. Shubitidze, B. E. Barrowes, K. O'Neill, A. Bijamov, R. Jobava, "Application of the ONVMS model to discriminate challenging UXO targets," Direct and Inverse Problems of Electromagnetic and Acoustic Wave Theory DIPED-2012, September 24–27, 2012.
- [2] J. P. Fernández, A. Bijamov, I. Shamatava, B. E. Barrowes, K. A. O'Neill, and F. Shubitidze. "Optimizing EMI transmitter and receiver configurations to enhance detection and identification of small and deep metallic targets," *Proceedings of SPIE* 8357, 8357-02 (2012).
- [3] Dimitris P. Economou, Fridon Shubitidze, Ben Barrowes, Nikolaos K. Uzunoglu, "MUSIC algorithm applied to advanced EMI sensors data for UXO classification," International Conference on Electromagnetics in Advanced Applications - ICEAA, 2011.
- [4] F. Shubitidze, J. P. Fernández, I. Shamatava, A. Luperon, B. E. Barrowes, and K. A. O'Neill, "Inversion-free discrimination of unexploded ordnance in real time," *Proceedings of SPIE* 8357, 8357-04 (2012).
- [5] F. Shubitidze, J. P. Fernández, B. E. Barrowes, K. O'Neill, "A new EMI System for detection and classification of challenging targets," *Proceedings of SPIE*, Baltimore, April 28–May 2, 2013.
- [6] F. Shubitidze, B. Barrowes, I. Shamatava, J. Sigman, Y. Wang, K. O'Neill, "Detecting and classifying small and deep targets using improved EMI hardware and data processing approach," *Proceedings of SPIE*, May 5-9, 2014, Baltimore (2014).
- [7] J. Sigman, B. Barrowes, Y. Wang, K. O'Neill, F. Shubitidze, "Automatic classification of unexploded ordnance applied to live sites for MetalMapper sensor," *Proceedings of SPIE*, May 5-9, 2014, Baltimore (2014).
- [8] Y. Wang, J. Sigman, B. Barrowes, Y. Wang, K. O'Neill, F. Shubitidze, "A combined joint diagonalization-MUSIC algorithm for subsurface target localization," *Proceedings of SPIE*, May 5-9, 2014, Baltimore (2014).
- [9] Y. Wang, J. Sigman, B. Barrowes, Y. Wang, K. O'Neill, F. Shubitidze, "A combined joint diagonalization-MUSIC algorithm applied to  $2 \times 2$  TEMTADS localizations of subsurface targets," *Proceedings of SAGEEP*, Boston, March 16-20, 2014.
- [10] J. Sigman, B. Barrowes, Y. Wang, K. O'Neill, F. Shubitidze, "An expert-free technique for live site UXO target classification," *Proceedings of SAGEEP*, Boston, March 16-20, 2014.
- [11] I. Shamatava, B. Barrowes, J. Sigman, F. Shubitidze, "West Mesa MetalMapper data inversion and classification," *Proceedings of Direct and Inverse Problems of Electromagnetic and Acoustic Wave Theory*, September 22-25, 2014, Tbilisi, Georgia.
- [12] Y. Wang, "Fast Algorithms for Subsurface Target Locating and Mapping in Unexploded Ordnance Detection", Master's Thesis, Thayer School of Engineering, Dartmouth College, Hanover NH, 04, 2015.

## 9 References

- [1] ESTCP, “ESTCP Classification Pilot Program Live Site Demonstrations”, <http://serdp-estcp.org/Featured-Initiatives/Munitions-Response-Initiatives/Classification-Applied-to-Munitions-Response>.
- [2] Mark Prouty, “Detection and Classification with the MetalMapper™ at Former Camp San Luis Obispo,” ESTCP Project No. MM-0603, Geometrics, Inc. July 2009.
- [3] F. Shubitidze et al., “A complex approach to UXO discrimination: Combining advanced EMI forward models and statistical signal processing,” SERDP MR-1572 Final Report, January 2012.
- [4] S. Cazares and M. Tuley, “UXO Classification Study: Scoring Memorandum for the former Camp San Luis Obispo, CA,” Institute for Defense Analyses, 13 March 2009.
- [5] B. Spargo, “ESTCP MR-201165 Demonstration Data Report Former Camp Beale TEMTADS MP 2x2 Cart Survey,” Technical report, August 2011.
- [6] Nicolas Lhomme, “Man-Portable Vector EMI Sensor for Full UXO Characterization,” ESTCP Project MR-201005; Technical Report, March 2012.
- [7] J. P. Fernández, B. E. Barrowes, A. Bijamov, T. M. Grzegorzczak, N. Lhomme, K. O’Neill, I. Shamatava, and F. Shubitidze, “MPV-II: an enhanced vector man-portable EMI sensor for UXO identification,” *Proceedings of SPIE*, 8017, 2011.
- [8] Shubitidze, F., Fernández, J.P., Barrowes, B., Shamatava, I., Bijamov, A., O’Neill, K., and Karkashadze, D., “The orthonormalized volume magnetic source model for discrimination of unexploded ordnance,” *IEEE Transactions on Geoscience and Remote Sensing*, 52, 4658-4670, (Aug 2014).
- [9] F. Shubitidze, J. P. Fernández, I. Shamatava, B. E. Barrowes, and K. A. O’Neill, “Joint diagonalization applied to the detection and discrimination of unexploded ordnance,” *Geophysics*, Jul 2012, Vol. 77, No. 4, pp. WB149-WB160.
- [10] Dimitris P. Economou, Fridon Shubitidze, Ben Barrowes, and Nikolaos K. Uzunoglu, “MUSIC algorithm applied to Advanced EMI sensors data for UXO classification,” *International Conference on Electromagnetics in Advanced Applications – ICEAA*, 2011.
- [11] Y. Wang, “Fast Algorithms for Subsurface Target Locating and Mapping in Unexploded Ordnance Detection”, Master’s Thesis, Thayer School of Engineering, Dartmouth College, Hanover NH, 04, 2015.
- [12] F. Shubitidze, K. O’Neill, B. E. Barrowes, I. Shamatava, J. P. Fernández, K. Sun, and K. D. Paulsen, “Application of the normalized surface magnetic charge model to UXO discrimination in cases with overlapping signals,” *Journal of Applied Geophysics*, vol. 61, pp. 292–303, 2007.
- [13] P. Comon, “Independent Component Analysis, a new concept,” *Signal Processing*, vol. 36, pp. 287–314, 1994.
- [14] A. Belouchrani, K. Abed-Meraim, J. F. Cardoso, and E. Moulines, “A blind source separation technique using second-order statistics,” *IEEE Transactions on Signal Processing*, vol. 45, pp. 434–444, 1997.
- [15] S. Harmeling, A. Ziehe, M. Kawanabe, and K. R. Muller, “Kernel-based nonlinear blind source separation,” *Neural Computation*, vol. 15, pp. 1089–1124, 2003.
- [16] B. N. Flury and W. Gautschi, “An algorithm for simultaneous orthogonal transformation of several positive definite symmetrical matrices to nearly diagonal form,” *SIAM Journal on Scientific and Statistical Computing*, vol. 7, pp. 169–184, 1986.

- [17] J. F. Cardoso and A. Souloumiac, "Jacobi angles for simultaneous diagonalization," *SIAM Journal on Matrix Analysis and Applications*, vol. 17, pp. 161–164, 1996.
- [18] L. Pasion *et al.*, "UXO Discrimination Using Full Coverage and Cued Interrogation Data Sets at Camp Butner, NC," SERDP-ESTCP, Partners 2010.
- [19] Paski *et al.*, "Former Camp Butner Site Description and EM61 Data Collection and Analysis," SERDP-ESTCP, Partners 2010.
- [20] Carin, L., Zhang, Y. and Liao, X., 2004, Detection of Buried UXO via Active Selection of Labeled Data: Presentation at The UXO Forum 2004.
- [21] Billings, S. D., 2004. Discrimination and classification of buried unexploded ordnance using magnetometry: *IEEE Transactions of Geoscience and Remote Sensing*, 42(6), 1241-1251.
- [22] D. Keiswetter *et al.*, "SAIC Data Analysis of Data Acquired at Camp Butner," Partners 2010.
- [23] S. Billings *et al.*, "Processing and Discrimination Strategies for Next-Generation EMI Sensor Data", SERDP-ESTCP, Partners 2010.
- [24] Keiswetter *et al.*, "EM61 and Magnetic Sensors: Application and Performance Summary at Camp SLO", ", SERDP-ESTCP, Partners 2010.
- [25] F. Shubitidze, D. Karkashadze, J. P. Fernández, B. E. Barrowes, K. O'Neill, T. M. Grzegorzczuk, and I. Shamatava, "Applying a Volume Dipole Distribution Model to Next-Generation Sensor Data for Multi-Object Data Inversion and Discrimination," *Proceedings of SPIE*, vol. 7664, 2010.
- [26] S. J. Hart *et al.*, 2001, "Using Physics Based Modeler Outputs to Train Probabilistic Neural Networks for Unexploded Ordnance (UXO) Classification in Magnetometry Surveys," *IEEE Trans. Geosci. Remote Sensing*, 39, 797-804.
- [27] R. O. Schmidt, "Multiple emitter location and signal parameter estimation," *IEEE Transactions on Antennas and Propagation*, AP-34: 276-280, 1986.
- [28] J. J. Ermer, J. C. Mosher, M. Huang, and R. M. Leahy, "Paired MEG Dataset Source Localization Using Recursively Applied and Projected (RAP) MUSIC," *IEEE Trans. Biomedical Engineering* 47(9): 1248-1260, 2000.
- [29] A.J. Devaney, "Super-resolution processing of multi-static data using time reversal and MUSIC," Northeastern University Preprint, 2000.
- [30] H. Ammari, E. Iakovleva, and D. Lesselier, "A MUSIC algorithm for locating small inclusions buried in a half-space from the scattering amplitude at a fixed frequency," *Multiscale Model. Simul.* 3: 597-628, 2005.
- [31] H. Ammari, E. Iakovleva, D. Lesselier, and G. Perrusson, "'MUSIC-type electromagnetic imaging of a collection of small three-dimensional bounded inclusions," *SIAM J. Sci. Comput.* 29(2): 674-709, 2007.
- [32] R. Storn, and K. Price, "Differential evolution: a simple and efficient adaptive scheme for global optimization over continuous spaces," *Journal of Global Optimization*, vol. 11, pp. 341–359, 1997.
- [33] R. Storn, "System design by constant adaptation and differential evolution," *IEEE Trans. Evol. Comput.*, vol. 3, pp. 22–34, 1999.
- [34] A. Bijamov, J. P. Fernández, B. E. Barrowes, I. Shamatava, K. O'Neill, and F. Shubitidze, "Camp Butner Live-Site UXO Classification using Hierarchical Clustering and Gaussian Mixture Modeling," *IEEE Transactions on Geoscience and Remote Sensing*, Digital Object Identifier 10.1109/TGRS.2013.2287510.

- [35] J. Byrnes, Ed., *Unexploded Ordnance Detection and Mitigation*, ser. NATO Science for Peace and Security Series B: Physics and Biophysics. Dordrecht: Springer Netherlands, 2009.
- [36] Zhang, Y., Collins, L., Yu, H., Baum, C. E. and Carin, L., 2003, “Sensing of Unexploded Ordnance with Magnetometer and Induction Data: Theory and Signal Processing,” *IEEE Trans. Geosci. Remote Sensing*, 41, 1005–1015.
- [37] Billings, S. D., 2004. “Discrimination and classification of buried unexploded ordnance using magnetometry,” *IEEE Transactions of Geoscience and Remote Sensing*, 42(6), 1241–1251.
- [38] Carin, L., Zhang, Y. and Liao, X., 2004, “Detection of buried UXO via active selection of labeled data,” Presentation at the UXO Forum, 2004.
- [39] Grimm, R. E., 2003, “Triaxial modeling and target classification of multi-channel, multicomponent EM data for UXO discrimination,” *Journal of Environmental and Engineering Geophysics*, 8, 239-250.
- [40] J. P. Fernández, F. Shubitidze, I. Shamatava, B. Barrowes, and K. O’Neill, “Realistic subsurface anomaly discrimination using electromagnetic induction and an SVM classifier”, *EURASIP Journal of Advances in Signal Processing*, 2010.
- [41] T. Bell, “Classification Study Using a Handheld, Three-element EMI Sensor”, SERDP Project MR-2201, final report, April 2013.
- [42] B. Barrowes, “Portable Electromagnetic Induction Sensor with Integrated Positioning”, final report SERDP-1712, August 2013

## 10 Appendix: Minimizing noise

The objective of this study is to detect deep targets. This correspondingly implies maximizing signal and minimizing noise. Maximizing signal implies making a high-power transmitter and choosing signals that maximize the response produced by the target. Minimizing noise means assuring that the limiting noise level is environmental noise, minimizing effective noise bandwidth, and placing the signal spectrum in regions of the environmental-noise spectrum where it is smallest with respect to the signal. The main text discussed the effects of Tx loop size in maximizing signal. This appendix examines the second part of the problem: minimizing noise. In a time-domain TEM system, both primary and secondary fields are present at the receiver during the on-time and during the initial part of the off-time, as the transmitter field is decaying to zero. This is the reason that making a B-field sensor from a  $dB/dt$  induction coil is difficult. It would be simple if the sensor were exposed only to the secondary B field, in which case we could integrate the secondary  $dB/dt$  signal acquired during the entire off-time, and the result would be a very good estimate of the B field.

During this study, first we have presumed the target produces a step response of the form

$$B_s(t) = \beta \delta^\gamma (t + \delta)^{-\gamma} e^{-\alpha t}, \quad (\text{A1})$$

where in this study  $\alpha = 1000$  (1 ms time constant),  $\gamma = 0.5$ ,  $\delta = 10 \mu\text{s}$ ,  $\beta$  = signal amplitude. To generate the secondary field, we first assume the system response to a step-function turnoff is given by Equation A1. Then the impulse response of the system can be derived as the derivative of  $(1 - B_s(t))$ . We use a) a primary field with a 5ms exponential turnon and b) a primary turnoff transient that is an exponential with a 10  $\mu\text{s}$  time constant. When this signal is convolved with the system impulse response, the result is the secondary signal. The result is shown in Figure 67. The plot shows the primary field in blue and the secondary field in green. For assessing real scenarios, we add noise as shown in Figure 69 (yellow trace<sup>1</sup>). The signal plus noise are passed through a two-cascaded-stage filter where each stage is a single pole lowpass filter with a 3dB

---

<sup>1</sup> The noise is a random number generator with a uniform probability density function from -0.01 nT to +0.01nT. To be more accurate, this noise could be modeled as a Gaussian distribution or even more accurately as a log-normal distribution. But for our purposes, the difference would not change the conclusions.

corner frequency of 50kHz. Finally, we generate logarithmically spaced gates, following standard practice. The gate outputs, shown as red points, are made by averaging the yellow signal over the time of each gate. The gates shown in Figure 67 are 15% gates.

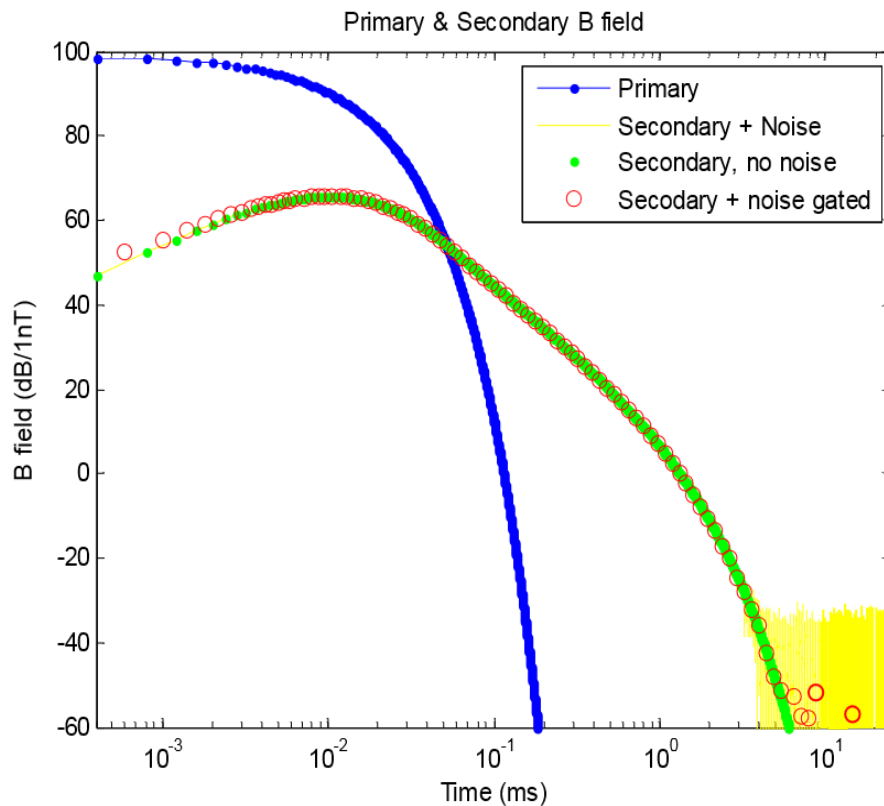


Figure 67. B field signals.

We differentiate the B signals from Figure 67 to produce dB/dt signals in units of nT/s assuming the receiver coil has an effective area of  $1\text{m}^2$  (see Figure 68). The secondary signal changes sign at about  $10\mu\text{s}$ , indicated by the dip in Figure 68. By comparing the B field of Figure 67 to the dB/dt of Figure 68 we notice that:

- The dynamic range of the secondary B field is just over 120 dB for times up to 6 ms while the dynamic range of the dB/dt signal is 160 dB over the same time range.
- The primary and secondary amplitudes cross at about the same times.

- The raw (wideband) noise level for the B field meets the secondary signal at 4 ms for the B field and at 1 ms for the dB/dt signal. This would at first indicate that a B-field sensor would be worthwhile. However, the time-gating function does a better job of reducing noise for the dB/dt signal than for the B-field, and the gated signals are roughly similar, not becoming noise until about 4 ms even though the B-field might be given a slight edge.

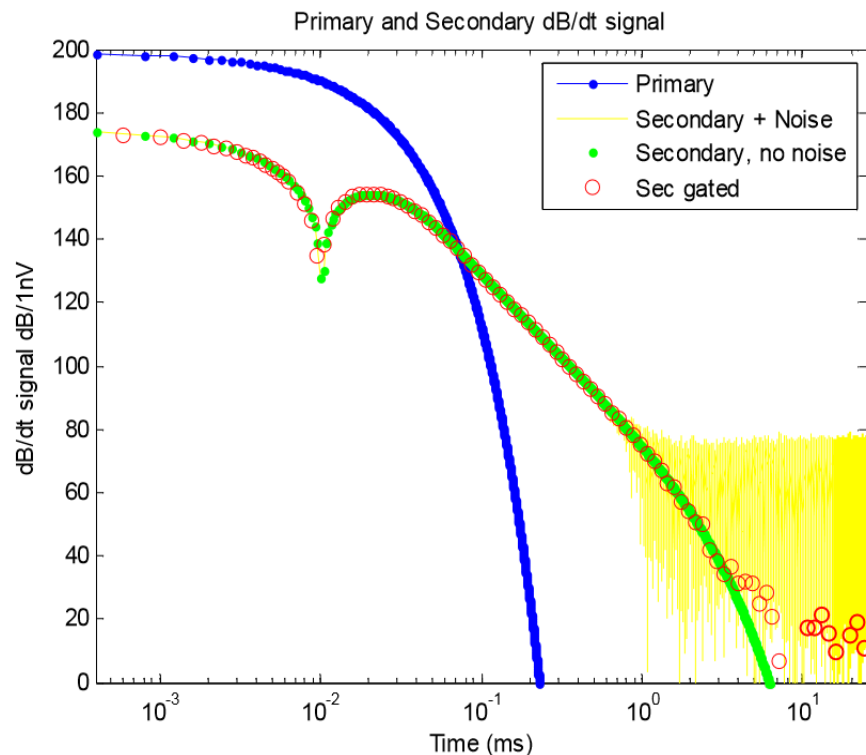


Figure 68. dB/dt signals.

One way to produce a B-field signal from the dB/dt signal is to integrate the secondary dB/dt signal numerically. The result, depicted in Figure 69, shows comparisons between expected signals (see Figure 67) and computed B signals. Although the computed magnetic field agrees well with the expected B field, one must realize that the approach taken here cannot be used in real practice because it is not possible to separate the secondary signal from the primary signal

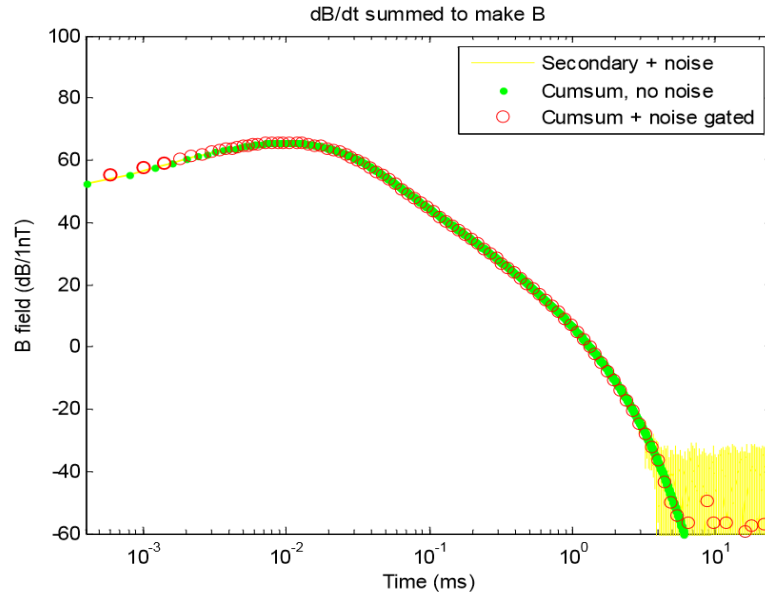


Figure 69. B signals computed from dB/dt signals.

during the time period that the primary is turning off and the secondary is rising. This fact is crucial if the secondary B-field signal is to be produced from the dB/dt signal. The integrator must integrate the early-time part of the secondary dB/dt (which is of opposite in sign to the late-time part) so that the late-time part subtracts from the early-time part, giving zero.

To get a sense of the effects of a B-field sensor using real-life data, here we present a few samples of actual data. In these samples, the ending value for the cumulative sum of the dB/dt signal is arbitrarily taken as the mean of the cumulative sum over the last 25% of the decay curve. Since the data are decimated, this reduces to the mean of the last two gates. The data were taken at Aberdeen using the PEDEMIS system's *deep one* configuration [42]. During the deep one configuration, the  $(3 \times 3)$  Rx array is placed in position #1 (the center of the PEDEMIS Tx array) and data are acquired for transmitters #2, 4, 6, and 8 for deep targets. The data were collected on 11/9/2012 over targets P8, P11, and P3. The data shown are transmitter current-normalized and they are background-subtracted, using as background the average of files DeepOne00113 (test pit), DeepOne00114 (target T13), and DeepOne115 (Target T13 repeat).

Three samples are shown in Figure 70, Figure 71, and Figure 72. Figure 70 is a large, deep target. Figure 71 is an obvious nontarget. Figure 72 is a weak target. The figures show the usual  $z$ ,  $y$ , and  $x$  dB/dt signals on the left and the computed B-field signals on the right.

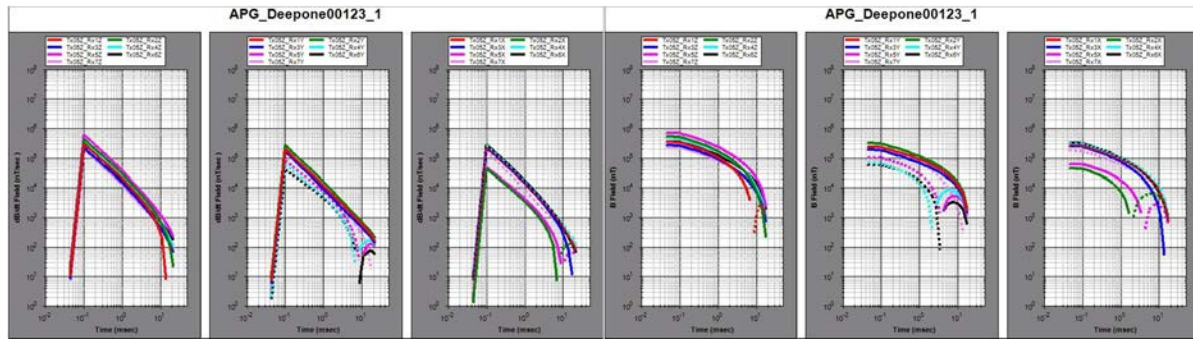


Figure 70. dB/dt and CumSum signals for target at position P8 at Aberdeen.

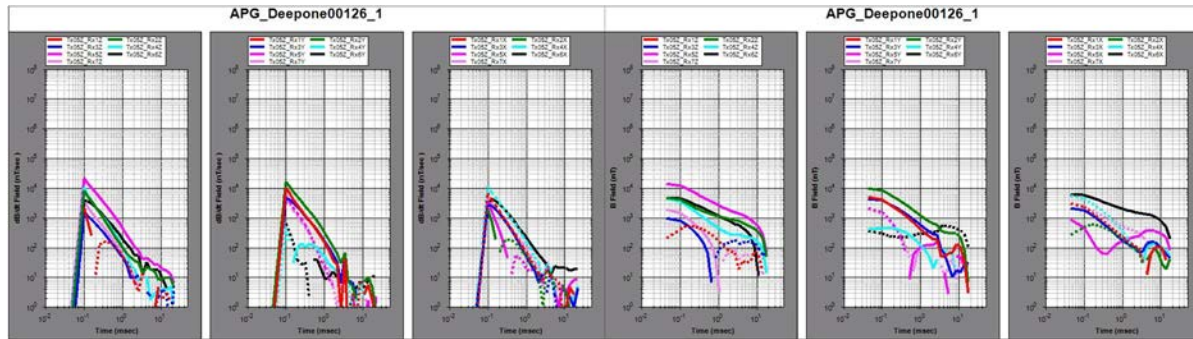


Figure 71. dB/dt and CumSum signals for target at position P11 at Aberdeen.

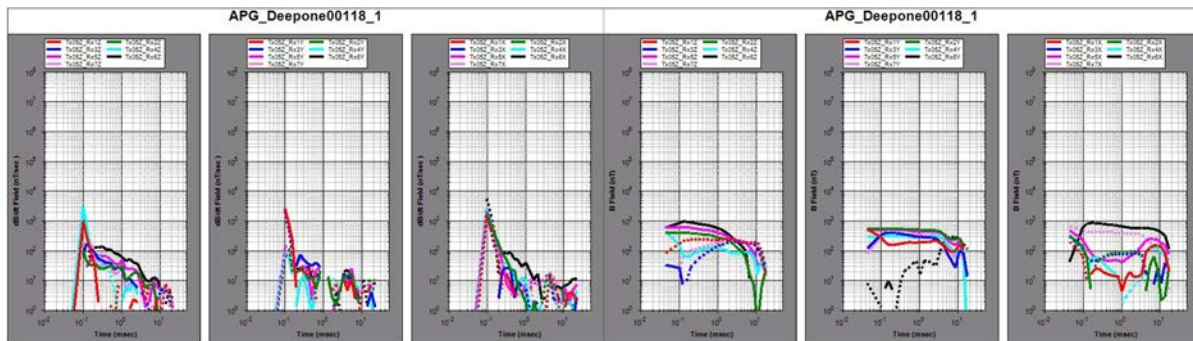


Figure 72. dB/dt and CumSum signals for target at position P3 at Aberdeen.

The figures do not show conclusively that a B-field calculation is desirable, yet they tend certainly to *appear* less noisy than the dB/dt signals. The B-field calculation for the large target is of limited accuracy due to fact that the target's decay has not reached the background level at the end of the decay time.

To assess whether a dB/dt signal of a B-field signal would be better for detection of small and deep targets, here we illustrate some signals that are near the detection limits discussed in Section 5.3.3 on the Minimum detectable signal.

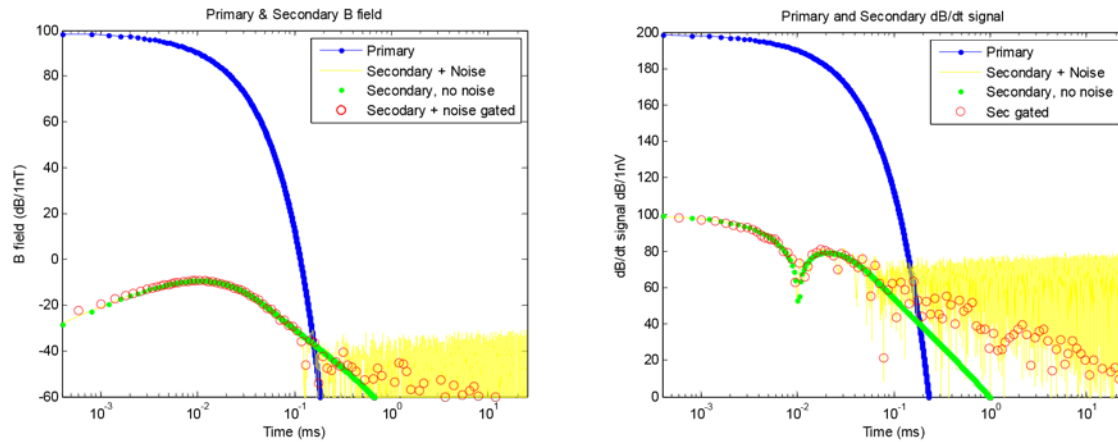


Figure 73. B Fields and dB/dt signals for a deep target.

The results for a target with a signal level of 0 dB/nT are shown in Figure 73. An interesting note in these two results is that the secondary signal in both cases does not become greater than the primary die-away until about 200 $\mu$ s, so background subtraction, particularly subtraction of the primary field at early times, would be important. It also could be argued that, instead of worrying about noise, it might be more productive to worry about speeding up the primary turn-off<sup>2</sup>.

This study does not settle the question whether producing a B-field signal significantly improves detectability, but it does make it clear that producing a B-field signal is desirable in terms of wideband noise.

---

<sup>2</sup> This is contrary to the thought to maximize number of turns and size of the transmitter, two factors which both tend to slow down the speed at which the transmitter can be turned off.